Thesis for the degree of Doctorate of Philosophy

Deformation mechanisms and load distribution in multi-phase engineering materials

NITESH RAJ JALADURGAM

Department of Physics

Chalmers University of Technology

Göteborg, Sweden 2021

Deformation mechanisms and load distribution in multi-phase engineering materials
Nitesh Raj Jaladurgam

ISBN 978-91-7905-544-8

Doktorsavhandlingar vid Chalmers tekniska högskola
Ny serie nr 5011
ISSN 0346-718X

Department of Physics
Chalmers University of Technology
SE-412 96 Göteborg
Sweden
Telephone + 46 (0)31-772 1000

Cover illustration

The top left picture shows the possible load distribution in Haynes 282 between two grains and between γ and γ' phases. Further down, the load distribution between γ and γ' as a function of γ' particle size is shown in (a) and (b). The top right picture corresponds to the phase microstructure of $AlCoCrFeNi_{2.1}$ EHEA and the sketch of orientation relationship between the ordered $L1_2$ and B2 phases. The four plots (a-d) illustrates the load distribution between two ordered phases as a function of temperature.

Printed by Chalmers Reproservice
Göteborg, Sweden 2021

Deformation mechanisms and load distribution in multi-phase engineering materials
Nitesh Raj Jaladurgam
Division of Microstructure Physics
Department of Physics
Chalmers University of Technology

Abstract

While the transition to carbon neutral technologies is still in progress, it is vital to reduce the environmental impact of existing processes. The efficiency of combustion processes for e.g. power generation and aviation can be greatly improved by increasing the operating temperature. This, however, requires development of new and improved materials with increased temperature capability. Similarly, materials which enable e.g. storage of hydrogen or liquid natural gas at cryogenic temperatures can contribute to the above transition. Such high performance engineering materials are usually very complex, with many alloying elements and multiple phases. During deformation the behaviour of the phases, and the grains with different orientations within each phase, is a result of elastic and plastic interactions. Quantifying how the stresses and strains are redistributed within and among the phases is essential for the development of quantitative models capable of accurately predicting the macroscopic mechanical response from the single crystal properties.

This thesis explores the use of in-situ neutron diffraction for investigating load partitioning and deformation mechanisms in two different advanced multi-phase materials, a Ni-based superalloy and a eutectic high entropy alloy, across a wide temperature range (from 20 to 1000 K). For the superalloy, the main findings are: (i) the effect of particle size on the deformation mechanisms and load partitioning was consistent across all temperatures; (ii) plastic deformation of the strengthening phase at high stresses occurred at cryogenic temperatures, which has not been previously reported; and (iii) a strong orientation and phase dependence of the damage evolution during high-temperature deformation was observed. In the eutectic high entropy alloy transitions in the deformation mechanisms of the constituent phases were found to occur with increasing temperature, which lead to a new proposed alloy design strategy for optimising the high temperature properties. Further, the role of the phases is reversed at higher temperatures, i.e. the soft phase at lower temperature becomes the reinforcing phase when the temperature increases. The reported results will have a large impact on the development of accurate multi-scale models for property prediction, as well as development and optimization of complex materials which contribute to a sustainable society.

Keywords: Superalloys, Eutectic high entropy alloys, Deformation mechanisms, Load distribution, In-situ neutron diffraction, Electron microscopy

Preface

The research work presented in this thesis was carried out at the Division of Microstructure Physics at the Department of Physics, Chalmers University of Technology, during the time period August 2017 - August 2021, under the supervision of Associate Professor Magnus Hörnqvist Colliander and Associate Professor Mattias Thuvander.

This research is funded by the Swedish Foundation for Strategic Research (SSF) within the Swedish national graduate school in neutron scattering, SwedNess. The authors acknowledge the allocation of beam times (RB1720280, RB1720281 and RB1810499) at ISIS Neutron and Muon Source, Rutherford Appleton Laboratory, United Kingdom and beamtimes (2018B0117 and 2018B 0220) at Materials and Life Science Experimental Facility, J-PARC, Japan.

List of appended papers

I. *Microstructure-dependent deformation behaviour of a low γ' volume fraction Ni-base superalloy studied by in-situ neutron diffraction*
Nitesh Raj Jaladurgam, Hongjia Li, Joe Kelleher, Christer Persson, Axel Steuwer, Magnus Hörnqvist Colliander
Acta Materialia 183 (2020): 182-195.

II. *Macro- and micro-mechanical behaviour of a γ' strengthened Ni-based superalloy at cryogenic temperatures*
Nitesh Raj Jaladurgam, Saurabh Kabra and Magnus Hörnqvist Colliander
Materials & Design 209 (2021): 109954.

III. *Phase- and orientation-specific mechanical response during high-temperature deformation of a γ' strengthened Ni-based superalloy*
Nitesh Raj Jaladurgam, Stefanus Harjo and Magnus Hörnqvist Colliander
In Manuscript.

IV. *Temperature dependent load partitioning and slip mode transition in a eutectic $AlCoCrFeNi_{2.1}$ high entropy alloy*
Nitesh Raj Jaladurgam, Adrianna Lozinko, Sheng Guo, Tung Lik Lee and Magnus Hörnqvist Colliander
Materialia 17 (2021): 101118.

V. *Load redistribution in eutectic high entropy alloy $AlCoCrFeNi_{2.1}$ during high temperature deformation*
Nitesh Raj Jaladurgam, Adrianna Lozinko, Sheng Guo, Stefanus Harjo and Magnus Hörnqvist Colliander
In Manuscript.

My contributions to the appended papers

I. I performed the in-situ neutron diffraction measurements, analysis of results with the help of my supervisor. Hongjia Li did the modeling efforts involving elasto-plastic self-consistent models to predict the neutron diffraction insights. I performed and reported the detailed electron microscopy studies on the deformed samples. I wrote the paper in co-operation with the co-authors.

II. I performed the in-situ neutron diffraction measurements, analysis of results with the help of my supervisor and wrote the paper in co-operation with the co-authors.

III. I performed the in-situ neutron diffraction measurements, analysis of results with the help of my supervisor and wrote the paper in co-operation with the co-authors.

IV. I performed the in-situ neutron diffraction measurements and electron microscopy studies, analysis of results with the help of my supervisor and wrote the paper in co-operation with the co-authors.

V. I performed the in-situ neutron diffraction measurements, analysis of results with the help of my supervisor and wrote the paper in co-operation with the co-authors.

Acknowledgements

It gives me immense pleasure to express my gratitude to the people who have supported me in my PhD journey. I feel blessed to move to a new country for PhD studies which allowed me to experience different work culture. First and foremost, I am greatly thankful to my supervisor Dr. Magnus Hörnqvist Colliander for his constant support and guiding me with patience throughout the PhD project. It was a great experience to discuss the neutron diffraction experiments (science) in different angles and thank you very much for maintaining our regular work meetings particularly during the ongoing pandemic situation. I thank Dr. Mattias Thuvander for being an additional guidance support for my PhD work. I want to thank Prof. Mats Halvarsson and Prof. Lena Falk for their support in planning my PhD journey with valuable suggestions. I am thankful to Prof. Ru Peng for sharing valuable insights in the neutron diffraction data analysis aspects. I would also like to thank Prof. Christer Persson helping me in the initial days regarding tensile tests at the IMS department. I thank GKN Aerospace AB, and Prof. Sheng Guo, Adrianna for supporting me with the tensile samples of Haynes 282 and Eutectic high entropy alloy for my research work.

I am fortunate to be part of SwedNess graduate school where I participated in the courses with enthusiastic PhD colleagues working on wide variety of projects related to neutron scattering. I would like to thank the study director of SwedNess, Dr. Martin Månsson for planning and implementing the neutrons scattering based courses in a very effective way. I am grateful to the staff of ENGIN-X and TAKUMI beamlines whose support during beamtimes were invaluable. Special thanks to Dr. Axel Steuwer, Adrianna and Dr. Anand K Kanjarla for their help and support during the beamtime experiments. I extend my gratitude to CMAL staff for training and guidance with electron microscopy and sample preparation work. I would also like to thank Ola Löfgren for his timely help with the Macbook related issues. Also, special thanks to Microstructure Physics division members and people from Eva Olsson's group for maintaining such a friendly and positive work atmosphere. I want to thank Siamak Shoja for being a nice and warm-hearted office-mate and I always cherish the discussions we had about life in Sweden and EBSD related topics. I'm grateful to Dr. Anand HS Iyer for his help and guidance in the initial days of work with EBSD and other lab activities. Thanks to Rahul and JK for motivating me to start my fitness journey.

I am indebted to my parents and family for their tremendous support in each step of my life. Lastly, I am grateful to my wife, Sneha for her support, patience and unconditional love throughout this PhD journey.

To my Teachers, Parents and Friends

CONTENTS

CHAPTER 1

INTRODUCTION

1.1 Background and motivation

Whilst there are increasing in efforts to move to renewable energy sources, it is critically important to make the existing technologies as sustainable as possible. The power generation and aviation sectors are therefore always in search of high performance materials to increase their current capability. Higher working temperatures directly translate to more efficient combustion, better fuel efficiency and lower emissions [1]. Gas turbine engines are fundamental parts of land-based power generation and aircraft propulsion systems. In general, gas turbines have three main components: compressor, combustor and turbine. In the compressor, the atmospheric air is compressed and subsequently fed at high pressure into the combustion chamber where it is mixed with fuel and ignited. This operation generates enormous amounts of energy to propel the turbine setup in an aircraft or power generator. Due to the extreme conditions in the turbine, it is crucial to choose eligible materials to build components without any scope for failures. Materials such as Ni-base superalloys are known for high temperature applications and are work horses in gas turbines [2, 3]. Furthermore, as these materials typically have face cubic crystal (fcc) structure to give low diffusion rates at high temperatures, they often also exhibit good cryogenic properties and are used in e.g. fuel tanks and hydrogen/oxygen turbopumps for space applications. However, despite the success of Ni-base superalloys for these extreme applications, there is a continuous search for more efficient and/or economic solutions.

In order to achieve the combination of material properties required for such demanding applications multi-phase materials are typically needed. When the load is applied on multi-phase materials, the load distribution among phases can be in-homogeneous due to differences in the elastic and plastic properties of individual phases, and their respective deformation mechanisms. This load distribution can for example lead to premature failures from cracking of brittle phases or loss of strengthening capabilities in reinforcing phases.

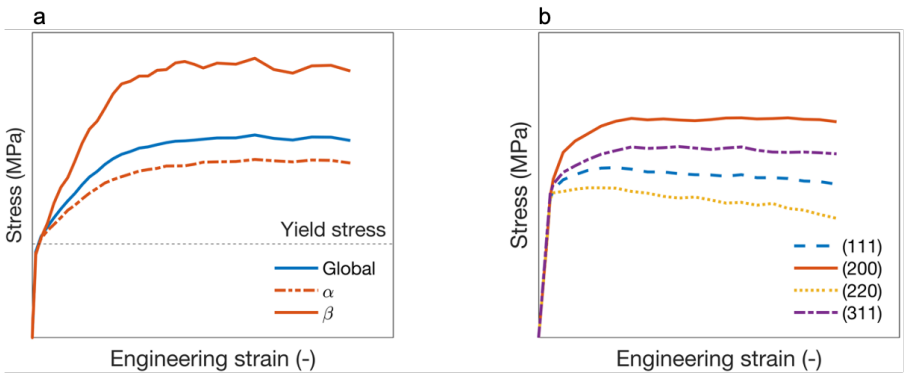

Figure 1.1: The evolution of (a) phase-specific and (b) orientation-specific response of two-phase material during an in-situ tensile test

Consider a two-phase composite material with a soft phase α and hard phase β, which is subjected to uni-axial tensile deformation. Fig. 1.1(a) illustrates the evolution of stress in the two phases with increasing applied strain. Initially, both phases undergo elastic deformation before yielding. However, a distinct load partitioning can be noticed right after the yield stress, where the soft α phase yields earlier and transfers the load to the hard β phase. In general, most of the plastic strain is carried by the soft α phase, while most of the stress is born by the hard β phase due to strain partitioning and load transfer between them. Thus, in order to fully understand the deformation of multi-phase alloys, it is crucial to measure the stress and strain in the phases in-situ during plastic deformation. Please note that the load distribution depends on many factors such as volume fraction and morphology of phases, grain size distribution and deformation temperature. Thus, the load distribution as shown in Fig. 1.1(a) can change with the mentioned factors.

Even in a single phase material the load is redistributed between grains with different orientations, as a result of elastic and plastic anisotropy. This is the case also for the individual phases in composite materials. For instance, assuming α phase has fcc crystal structure, the evolution of load/stress in grains with different orientations aligned with the tensile axis is shown in Fig. 1.1(b). It shows the stress experienced by four different orientations in fcc. Some orien-

tations, such as (220) and (111), yield earlier and carry lower stresses compare to other orientations, like (200) and (311). The yielding of individual orientations is mainly governed by the resolved shear stress (RSS) which depends on the orientation of the slip systems relative to the applied load. The plastic deformation initiates when the RSS reaches the *critical resolved shear stress* (CRSS). The crystal orientations with relatively high RSS will undergo yielding first and continuously transfer the load to other orientations where CRSS has not yet been reached and this phenomena continues until slip has been initiated in all orientations. Thus, there is a continuous load transfer between grains with different orientations, which furthermore will depend on the strain hardening of the different orientations. Depending on the microstructure, this will of course affect the interaction with embedded or adjacent phases, and thereby the load redistribution in multi-phase microstructures.

Thus, understanding of the load distribution is of great importance for alloy development and optimization of microstructures for tailored applications. In addition, knowledge of the load distribution is essential for the development of reliable models to predict the behavior of multi-phase engineering materials.

1.2 Scope of thesis

The aim of this thesis is to increase the knowledge and understanding of the phase and orientation-specific deformation in two distinctly different engineering materials which are expected to exhibit different behaviours with respect to load redistribution. The first material belongs to the traditional class of Ni-base superalloys and the second material is associated with recently developed next generation high entropy alloys called *eutectic high entropy alloy* (EHEA). These two materials have unique microstructures which can directly effect the load distribution and deformation mechanisms at different deformation temperatures.

1.2.1 Ni-base superalloys

Ni-base superalloys are extremely important materials for applications in aviation and power generation sectors due to their high resistance to corrosion and excellent mechanical properties at elevated temperatures [4]. They have complex chemistry and derive strength from the formation of various phases in the microstructure. The fcc matrix phase (γ) is strengthened by the solid solution effect, induced by the lattice distortions caused by the substitutional solute atoms such as Mo, Cr, Co, Fe etc. [5]. Another important mechanisms which enabled superalloys to strengthen at elevated temperature is precipita-

tion hardening [6]. It involves formation of intermetallic precipitates known as γ' or γ'' with ordered structures and maintained lattice coherency with the matrix phase. These precipitates contain Al, Ti and Nb, forming $Ni_3(Al,Ti)$ (γ' - cubic $L1_2$ structure) and Ni_3Nb (γ'' - body centered tetragonal $D0_{22}$ structure), respectively. They are the main strengthening agents which hinder the dislocation motion at high temperatures and enable anomalous increase in strength over 600 °C [7], which is discussed in detail in Chapter 2 (section 2.1.2).

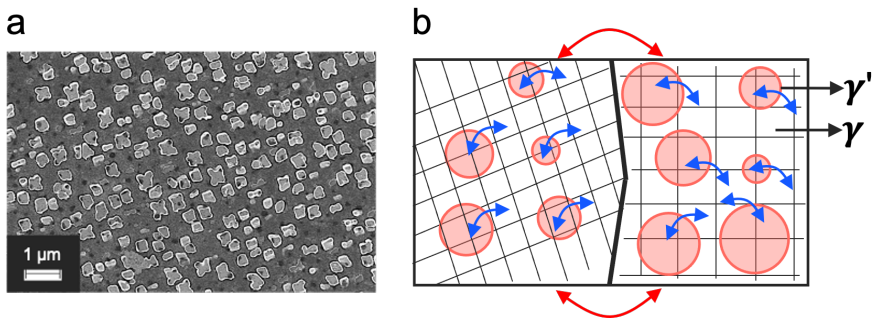

Figure 1.2: (a) The composite microstructure of a Ni-base superalloy (Haynes 282) with cuboidal precipitates in the matrix phase and (b) the model microstructure with γ' particles (red circles) in γ matrix sharing same crystal lattice with random grain boundary between two matrix grains

Most superalloys have relatively low γ' volume fractions, ~10–30%, to have a good balance between mechanical properties and fabricability. The microstructure of these alloys consists of γ matrix with embedded γ' (and/or γ'') strengthening particles as shown in Fig. 1.2(a), and discrete carbides (M_6C and $M_{23}C_6$) and/or intermetallic phases along the grain boundaries.

Fig. 1.2(b) illustrates a model microstructure of the alloy used in this thesis, Haynes 282. Here, both γ' and γ phases share the same orientations and slip planes due to the lattice coherency. When a material with this microstructure is deformed, both matrix and particles deform along same direction which is shown in Fig. 1.3. With increasing load, there will be interactions *between the matrix grains* indicated by red arrows in Fig. 1.2(b), as well as between matrix and particles *within each grain* indicated using blue arrows in the Fig. 1.2(b). Such interactions leads to load transfer between matrix grains and between γ matrix, γ' particles within each grain (Fig. 1.2(b)). As they share common slip planes, the dislocations gliding in the soft matrix can transmit into the γ' particles during deformation under certain circumstances [8]. This can lead to yielding of particles along with the matrix phase and directly affect the deformation response of the material. Ni-base superalloys are known to exhibit

complex load redistribution which depends on the deformation mechanisms [8–10]. These deformation mechanisms mostly depend on volume fraction, size of γ' and deformation temperature [11]. Many studies on load redistribution were reported for high γ' volume fraction ($f > 0.5$) Ni-base superalloys from 293 to 1000 K [8, 11–14]. But limited attention has been directed to low γ' volume fraction alloys, in spite of the fact that these alloys make up a large portion of the alloys used in applications. Further, these are potential materials for cryogenic applications but no load redistribution investigations are reported at sub-zero temperatures. This limited knowledge about the load transfer in low volume fraction alloys motivated the studies in this thesis, where a recently developed alloy, Haynes 282 with a volume fraction of γ' around 0.2, was chosen as a representative material. Haynes 282 has a unique combination of creep strength [15], thermal stability and fabricability [16] and was specifically developed for use in gas turbines and advanced ultra-supercritical boilers applications, where increased combustion temperatures are essential to improve the efficiency and reduce emissions.

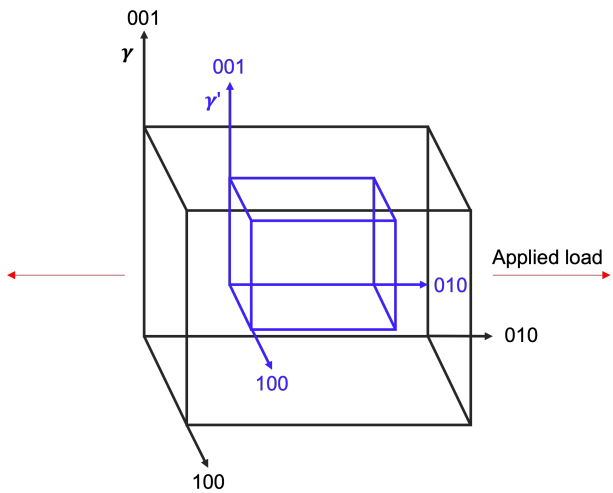

Figure 1.3: The lattice of γ and γ' when loaded under same orientation

1.2.2 Eutectic high entropy alloy

Recently, multicomponent high entropy alloys (HEAs) have gained interest due to their unique microstructures and desirable properties [17]. The concept of HEAs was introduced by Cantor et al. [18] and Yeh et al. [19], and involves combination of at least five principal elements in the at. % range between 5 % and 35 %. Many studies on HEAs have been reported, with single

phase microstructures of fcc providing good ductility at the cost of strength [20, 21], while single phase body centered cubic (bcc) microstructures have high strength but poor ductility [22, 23]. In order to obtain good combinations of both properties, multi-phase HEAs have been developed [24, 25]. However, the castability of these alloys is poor due to large solidification-temperature range leading to segregation and shrinkage cavity defects. This limitation has motivated the development of *eutectic high entropy alloys* (EHEAs), which were formed based on combining principles of eutectic alloys and high entropy alloys [26]. The eutectic reaction is an isothermal process with no solidification-temperature range leading to good castability and avoidance of shrinkage defects. Typically, eutectic alloys are resistant to microstructure change with temperature as high as the eutectic reaction temperature, which gives good control over properties such as creep resistance, high rupture strength with stable defect structures [27]. These properties are attributed to the lamellar or rod-like structures forming an in-situ composite in the as-cast condition.

Lu et al. [28] used this strategic alloy design approach and developed the alloy $AlCoCrFeNi_{2.1}$ with excellent castability at industry scale with minor defects. The microstructure of EHEA $AlCoCrFeNi_{2.1}$ has a distribution of coarse grains as shown in Fig. 1.4. Further, the inset from one grain reveals the lamellar microstructure which has been shown to consist of two ordered intermetallic phases, $L1_2$ and B2, with an orientation relationship called Kurdjumov–Sachs (K-S) relation [29–32].

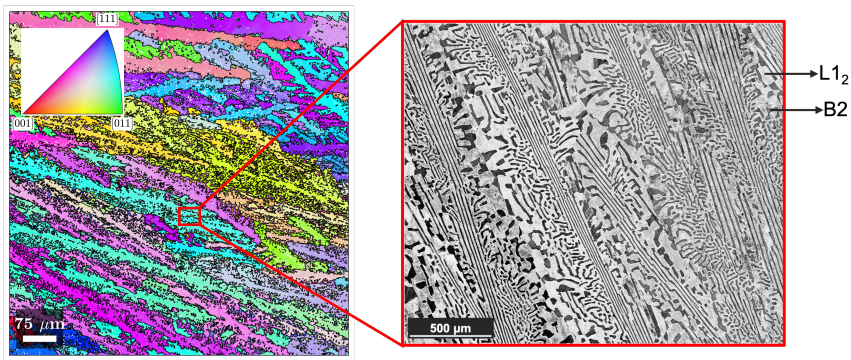

Figure 1.4: The microstructure of EHEA $AlCoCrFeNi_{2.1}$ with coarse grains in the as-cast condition and each color indicates the orientation of the grain. The inset from one grain reveals the lamellar microstructure of $L1_2$ and B2 phases.

The K-S relationship can be written as $(111)_{L1_2} \parallel (110)_{B2}$ and $[110]_{L1_2} \parallel [111]_{B2}$. This is illustrated in Fig. 1.5, where *one* (111) plane in $L1_2$ and *one* (110) plane in B2 are parallel, and *one* [110] direction in $L1_2$ aligns with *one* [111] direction in B2 within these planes. Here, the orientation relationship

is restricted to one plane and one direction, which makes slip transmission between the phases much more difficult, unlike the case of coherent phases in superalloys as discussed in the previous section.

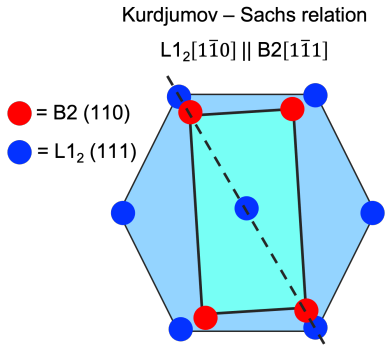

Figure 1.5: Kurdjumov–Sachs orientation relationship between $L1_2$ and B2 lattice. [33]

The elastic and plastic properties of individual phases and single phase boundaries in the $AlCoCrFeNi_{2.1}$ EHEA have been studied by nano-mechanical testing [34] and in-situ TEM [29]. These revealed complex interactions between the two ordered phases, which can effect the load redistribution between them. Thus, knowledge of the load distribution between $L1_2$ and B2 is essential to understand the interactions between the phases during plastic deformation. The reported excellent properties at high [28, 35] and low [36, 37] temperatures further motivates to study the load redistribution over a wide temperature range. Thus, this thesis considered the promising next generation engineering material, eutectic high entropy alloy - $AlCoCrFeNi_{2.1}$, to study the effect of deformation temperature on the load distribution between and within $L1_2$ and B2 phases from 77 K to 973 K.

1.3 Choice of method

The main focus of this thesis is to understand the load redistribution between and within phases of two distinct microstructures and in-situ diffraction is in principle the only way to measure these phenomena. It uses the interplanar spacing of the crystal lattice as internal strain gauge to measure the elastic strain in the diffracting grains. These elastic strains are proportional to the stress, which reveals the load redistribution among diffracting grains within phases. By suitable choice of geometry, strains in particular directions, e.g. parallel and perpendicular to the applied load, are measured. Other methods such as digital image correlation (DIC) is known for mapping of deformation

during micro and macro mechanical testing of materials. However, it measures only plastic strain under most circumstances and is limited to surfaces. Similarly, electron back-scatter diffraction (EBSD) has an ability to measure the orientations of diffracting grains during in-situ mechanical tests but is limited to mainly resolving plastic strain (except high resolution EBSD) from the surface of specimen under investigation. In-situ transmission electron microscopy (TEM) has limitations with the geometrical constraints and lack grain statistics compared to bulk specimens.

As discussed, most techniques, including lab diffraction, are limited to surface studies. Only neutrons and high energy X-rays diffraction (HE-XRD) allow the study of bulk specimens during deformation. Between them, neutrons are favourable for the two materials in the present work, and the motivation to use neutrons is mentioned below for each material case.

- For Haynes 282, the measurement of diffraction peaks from both γ matrix and γ' particles are needed during deformation to evaluate the elastic strains. In particular, the distribution of alloying elements on the specific lattice sites of γ' phase provides very good contrast for neutrons compared to HE-XRD, which makes it possible to measure the weak superlattice peaks more readily during in-situ deformation experiments. Hence, the in-situ deformation studies can be coupled with neutron diffraction in order to measure and understand the load redistribution in Haynes 282.
- In case of EHEA, as-cast $AlCoCrFeNi_{2.1}$ is chosen to understand the load redistribution between two ordered phases. The as-cast eutectic microstructure has a large average grain size, which requires a large gauge volume during in-situ deformation studies. Neutrons are superior in this respect as gauge volumes of several mm^3 are easily achieved. Thus, in-situ neutron diffraction is an ideal tool for the EHEA in this work.

1.4 Research questions

By using in-situ neutron diffraction during tensile testing at temperatures from 20 to 1000 K, the aim of this work has been to answer the following research questions.

- What is the effect of particle size on phase-specific deformation and load partitioning in low γ' volume fraction superalloys (such as Haynes 282)?
- What is the effect of deformation temperature on phase-specific deformation and load partitioning in low γ' volume fraction superalloys (such as Haynes 282)?
- What is the effect of deformation temperature on phase-specific deformation and load partitioning in as-cast EHEA $AlCoCrFeNi_{2.1}$?

CHAPTER 2

DEFORMATION MECHANISMS

Deformation mechanisms refers to the processes by which materials accommodate plastic strain. There are many kinds of deformation mechanisms reported and discussed thoroughly across alloys with different crystal structures by Ashby and Langdon et al. [38, 39]. Under the conditions covered in this thesis, the main deformation mechanism in Haynes 282 and EHEA is expected to be dislocation slip, which is why dislocations and their movement in the relevant microstructures will be discussed below.

2.1 Superalloys

Precipitation-strengthened superalloys are engineered for high temperature, high stress applications and have γ' particles, which act as strengthening agents, embedded in a γ matrix. The size, volume fraction and distribution of ordered intermetallic γ' particles have great impact on the mechanical properties [7]. The two phases (γ and γ') are coherent and undergo plastic deformation on the same slip systems, which allows the possibility of dislocation transmission between the matrix and particles. Hence, the deformation of γ and γ' are important to discuss in order to comprehend the deformation of γ'-strengthened Ni-base superalloys.

2.1.1 Deformation of fcc γ

The γ phase has the fcc crystal structure of the base element Ni with substitutional atoms randomly occupying the face centered and corner positions in the unit cell, as shown in Fig. 2.1. Slip in fcc occurs on the close packed {111} planes along the $\langle 110 \rangle$ directions, which are marked in a fcc unit cell along with Burgers vector as shown in Fig. 2.1.

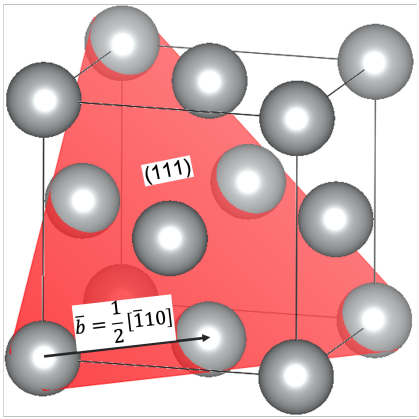

Figure 2.1: Schematic of fcc unit cell with Ni or randomly substituting solute atoms placed at both face centered and corner positions of the unit cell. Slip plane (111) and Burgers vector $\bar{b} = \frac{1}{2}[\bar{1}10]$ are marked in the fcc unit cell

The stress required to move a dislocation is given by Peierls Nabarro stress (τ_P) [40].

$$\tau_P = \frac{2G}{1-\nu} \exp\left(\frac{-2\pi d}{b(1-\nu)}\right) \tag{2.1}$$

Here, G is the shear modulus, ν is the Poisson's ratio, d is the lattice spacing of glide plane and b is the magnitude of Burgers vector. The fault in crystal arrangement leads to an increase in total energy which is proportional to $G \cdot b^2$. In order to reduce the energy, the dislocations in fcc can split into two partial dislocations (Eq. 2.2), provided that the sum of the energy of the partials is smaller than that of the complete dislocation.

$$\frac{a}{2}[110] \implies \frac{a}{6}[211] + \frac{a}{6}[12\bar{1}] \tag{2.2}$$

The partial dislocations are called Shockley partials and are separated by a stacking fault, which is associated with the stacking fault energy, γ_{SFE}. The average stacking fault energy of γ in Ni-base superalloys is in the range of 20-30 mJ/m^2 [41–46]. The equilibrium distance between the Shockley partials, d_{eq}

is determined by the balance between the decrease in energy from dissociation and increase due to γ_{SFE}, according to Eq. 2.3 [47].

$$d_{eq} = \frac{Gb^2}{4\pi\gamma_{\mathrm{SFE}}} g \tag{2.3}$$

Here, g is the geometric factor depends on ν and orientation of the dislocation. In superalloys, d_{eq} is found to be in the range of 15–25 Å. In other fcc materials such as Al, where γ_{SFE} is very high, no dissociation occurs. An important consequence of dislocation splitting is that individual Shockley partials cannot cross slip. Instead, thermally activated constriction to a full (screw) $\frac{a}{2}[110]$ is required in order to allow cross slip.

2.1.2 Deformation of ordered $L1_2$ γ'

The strengthening particle phase γ' in Ni-base superalloys has a simple cubic lattice with a 4 atom basis which is referred to ordered $L1_2$ structure (Pm-3m). In γ', the unit cell of ordered $L1_2$ has Al or Ti atoms at the corner positions and the face centered sites are occupied by Ni (or substitutional atoms) as shown in Fig. 2.2. It has similar potential slip planes as fcc, and {111} is the main active slip plane from ambient to around 700 °C. The Burgers vector has the same direction but twice the length of fcc, i.e. $\bar{b} = a\langle 110\rangle$, due to the ordered structure. Since the distance is larger than the distance between two lattice points, it is called a superdislocation.

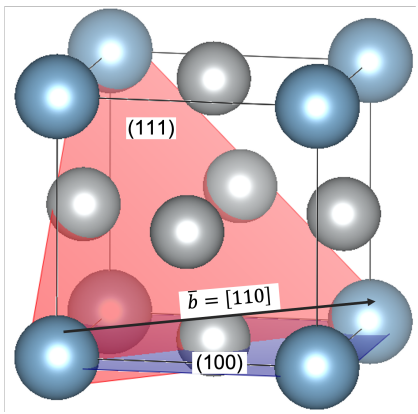

Figure 2.2: $L1_2$ structure with Ni atoms (blue) placed at the face centered positions and Al or Ti atoms (gray) occupying corners of the unit cell. The slip planes (111) in red and (100) in blue with the Burgers vector [110] are marked.

In $L1_2$, the $\langle 110 \rangle$ superdislocation tends to dissociate into two superpartial dislocations b_I and b_{II} (Eq. 2.4) to minimise the defect energy.

$$b = b_I + \text{APB} + b_{II} = a/2\langle 110 \rangle + \text{APB} + a/2\langle 110 \rangle \tag{2.4}$$

These superpartials create an anti-phase boundary between them due to the mismatch of nearest neighbour atoms, which accumulates an energy similar to stacking faults (10–100 mJ m^{-2}) [48]. The possible dislocation dissociations in $L1_2$ are shown in Fig. 2.3. The first superpartial (b_I) from the dissociated unit dislocation results in formation of an APB, which gets annihilated by the trailing superpartial (b_{II}) (see Fig. 2.3(a)). Fig. 2.3(b) shows the two superpartials (b_I and b_{II}) further dissociating into superlattice Shockley partials with Burgers vectors (b_1,b_2 and b_3,b_4), each pair separated by a complex stacking fault (CSF) [49, 50]. The CSF is considered as compound planar defects of superlattice intrinsic stacking fault (SISF) and APB [51]. Another potential

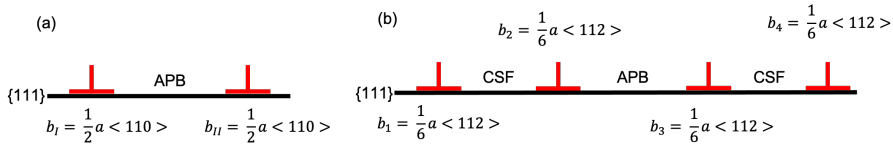

Figure 2.3: Possible dislocation dissociation in $L1_2$ structure, (a) two-fold APB-splitting, (b) four-fold [52, 53]

slip system in $L1_2$ involves the movement of $\langle 110 \rangle$ dislocations on $\{100\}$ planes with the APB formed on $\{100\}$. The dissociation on $\{100\}$ occurs as shown in Eq. 2.5.

$$b(\langle 110 \rangle) = b_I(a/2\langle 110 \rangle) + \text{APB}\{100\} + b_{II}(a/2\langle 110 \rangle) \tag{2.5}$$

The deformation of γ' occurs by moving dislocations with the Burgers vector $\langle 110 \rangle$ on either $\{111\}$ or $\{100\}$ planes depending on the operating temperature. From Fig. 2.4(a), the superdislocation dissociates into superpartials and further forms Shockley partials along with CSF and APB as shown in Fig. 2.3(b). The leading superpartial ($a/2\langle 110 \rangle$) can cross slip if it constricts to a pure screw type which lies in both $\{111\}$ and $\{100\}$. The resulting APB formed on $\{100\}$ has a lower energy than APB on $\{111\}$ leading to cross slip as shown in Fig. 2.4(b). Further dissociation of the leading partial can then occur according to Eq. 2.6.

$$b_I = a/6\langle 112 \rangle + \text{SISF} + a/6\langle 112 \rangle \tag{2.6}$$

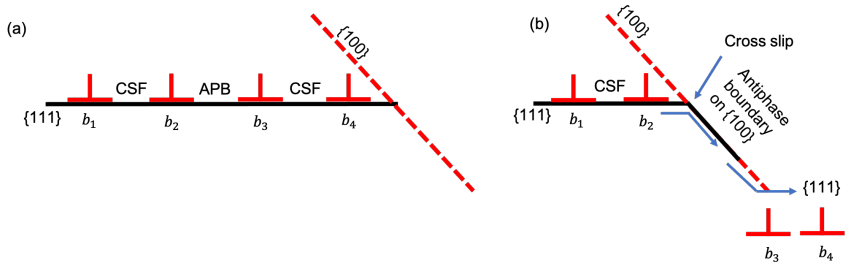

Figure 2.4: (a) Dissociation of superdislocation into superpartials and forming complex stacking fault and APB. (b) Cross slip of partials spread on two adjacent {111} planes and APB on {100} [52].

As the resulting Shockley partials do not lie in the {100} plane, the superpartial cannot move further on {100}. Furthermore, the lower APB energy on {100} prohibits movement of cross-slipping back onto {111}. This situation leads to sessile dislocations where all Shockley partials (b_1,b_2 and b_3,b_4) seize to move and do not allow other dislocations to glide on the plane. This is called a *Kear–Wildsdorf lock* [54] which occurs only in ordered structures. With increase in temperatures, more cross slip can occur leading to many Kear–Wildsdorf locks. The combined effect of cross slip and Kear–Wildsdorf locks is the main contribution to the high yield strength at elevated temperatures, which is often referred as *yield stress anomaly* [55] (i.e. the yield stress increases with increasing temperature), typically observed in ordered structures such as $L1_2$ [56], B2 [57] and $D0_3$ [58]. This phenomena does not obey Schmid's law and exhibits non-Schmid behaviour [59]. Also, this anomaly is usually exploited to design γ'-strengthened Ni-base superalloys to achieve desired mechanical properties up to 1000 °C.

However, after reaching a critical temperature, the superpartial dislocations (b_I and b_{II}) starts to move freely on {100} planes . This *slip mode transition* from {111} "octahedral" planes to {100} "cube" planes leads to a decrease in yield strength with increasing temperature. Hence, a delay in slip mode transition in $L1_2$ structure allows the strength to be retained at higher temperatures. This slip transition is discussed in detail in the case of deformation of $L1_2$ phase in EHEA from cryogenic to high temperature in Chapter 5 (section 5.2).

2.2 Deformation of superalloys (γ and γ')

The movement of dislocations usually occurs through glide, climb and cross slip depending on the deformation temperature and loading conditions. At temperatures when long-range cross slip and climb are not permitted, the deformation occurs only through glide, which is expected in this work. Due to the presence of γ' particles, the plastic deformation occurs mainly in two ways: shearing of particles by passing through a pair of dislocations or forming a dislocation loop around these strengthening agents (so called Orowan looping). The occurrence of these mechanisms depends on the size of the particles and volume fraction in γ matrix.

In order to understand these mechanisms, firstly consider the particle shearing condition. As mentioned earlier, the γ and γ' are coherent phases and share common slip planes during deformation. A single $a/2\langle 110\rangle$ matrix dislocation, (1) in Fig. 2.5(a), shears the γ' particles and disturbs the ordering by forming APB (as the matrix dislocation $a/2\langle 110\rangle$ corresponds to a superpartial in γ', see Eq. 2.4). A second $a/2\langle 110\rangle$ matrix dislocation (2) gliding on the same plane will annihilate the APB, restoring the order. Thus, a pair of matrix dislocations passing through a γ' particle act as a superdislocation and do not leave any remaining APB. As a consequence, matrix dislocations will always move in pairs, coupled by the APBs they create and annihilate. If the particle size is less than the spacing of the dislocation pairs, it leads to weakly coupled dislocations, where only one dislocation is inside the particle at any given time (see Fig. 2.5(a)). On the other hand, an increase in particle size leads to strongly coupled dislocations where both dislocations, i.e. the entire "superdislocation", is inside the particle at a given instance, as shown in Fig. 2.5(b). The motion of these dislocation pairs depend on the applied shear stress, repulsive force between them and the force associated with APB formation [61, 62]. The shear stress to cut through the particles are dependent on the size and volume fraction of the particle for weakly [63] and strongly

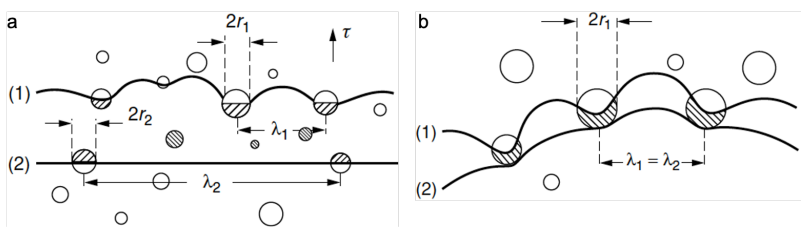

Figure 2.5: Shearing of γ' particles by (a) weakly and (b) strongly pair-coupled dislocations [60]

coupled dislocations [60] as:

$$\tau_{\text{weak}} \propto \gamma_{\text{APB}}^{3/2} \sqrt{\frac{rf}{G}} \tag{2.7}$$

$$\tau_{\text{strong}} \propto \sqrt{\frac{\gamma_{\text{APB}} G f}{r}} \tag{2.8}$$

Here, γ_{APB} is the energy of the anti-phase boundary in γ', r is the radius of the particle, f is the volume fraction and G is shear modulus of the particle. Usually, weakly coupled dislocations occur for under-aged conditions and strongly coupled dislocations are observed in over-aged cases. For both weakly and strongly coupled dislocations, an increase in volume fraction increases the critical shear stress. An increase in particle size increases the critical shear stress for weakly coupled dislocations but decreases it for strongly coupled dislocations. Thus, both volume fraction (f) and particle size (r) can influence the deformation mechanisms.

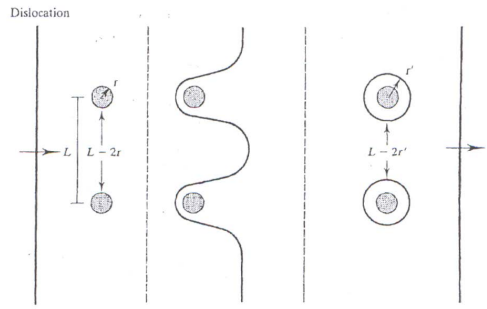

Figure 2.6: A sketch of Orowan process [60]

The other mechanism, Orowan looping, occurs when the particles are not penetrated by the dislocations. As the particles cannot be sheared, the dislocation will bow around them. When the dislocation closes in on itself, it leaves behind a loop around the particles and is then free to move, as shown in Fig. 2.6. This bowing and looping of particles is often observed in the case of large particles. The shear stress (τ_O) for Orowan process is given below.

$$\tau_O = \frac{Gb}{L} \propto \frac{1}{r} \tag{2.9}$$

Here, L is the inter-particle spacing. As no shearing occurs, no APBs are created. Orowan looping thus involves single matrix dislocations rather than coupled pairs. Similar to the case of shearing, increasing the volume fraction increases the critical shear stress for Orowan looping, but an increase in particle size decreases the critical shear stress, similar to strongly coupled dislocations.

Fig. 2.7 shows the critical resolved shear stress (CRSS) normalized by volume fraction, with change in particle diameter. It has a transition particle size (D_{WS}) from weak to strong pair-coupling which typically applies from fine to coarse particle size. Also, D_c indicates the critical particle size for transition from shearing by strongly coupled dislocations to the Orowan process. Values of D_c in the range of 100–200 nm have been reported [64–66], depending on the volume fraction of γ'.

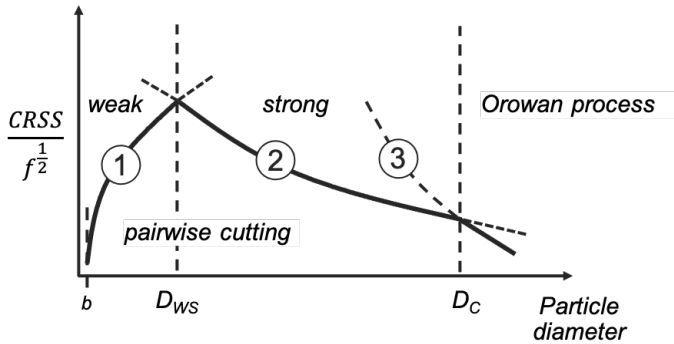

Figure 2.7: Schematic representation of critical resolved shear stress normalized with volume fraction as a function of particle diameter. Three curves corresponding to ① weakly, ② strongly coupled dislocations and ③ Orowan process, respectively [60].

So far the effect of particle size and volume fraction on the deformation mechanisms have been discussed. However, the deformation temperature can also influence the dominant mechanism to be either shearing or Orowan looping or both in superalloys. For Haynes 282 with average particle size around 50 nm, room temperature deformation occurs through shearing of particles by pairs of dislocations, but the dominant mechanism changes to Orowan looping at 760 °C [9]. Zhong et al. [10] has studied the deformation of GH2984 superalloy with similar particle size (but with volume fraction 0.06) and also reported shearing at room temperature while the Orowan process dominated along with particle by passing via climb and cross-slip at high temperatures above 750 °C. Particle bypassing by thermally activated mechanisms such as local climb and/or cross-slip was proposed to occur above the peak strength temperature (around 700 °C) in both low volume fraction (NIMONIC PE16, $f = 0.08$) and high volume fraction (NIMONIC 105, $f = 0.48$) alloys. In general, it is difficult to estimate the dominant deformation mechanisms based on the working temperature, primarily due to the fact that (apart from the effect of particle size and volume fraction) there is a strong dependence on the balance between lattice misfit, anti-phase boundary energy and stacking fault energy, all of which are sensitive to the complex chemistry of the alloys [67].

Apart from slip, other deformation mechanism in superalloys is twinning during deformation, which has been reported under a variety of conditions over a range of temperatures. Creep studies on superalloys with low and high volume fraction γ' under certain conditions confirmed microtwinning as the principal deformation mechanism [49, 68–70]. Thermo-mechanical fatigue studies has found the deformation twinning as dominating in single crystal [71] and polycrystalline superalloys [72, 73]. In TMW-4M3 disc superalloy, the transition from stacking fault shearing to deformation twinning was found to be dominant in the intermediate temperature (650–725 °C) under tension [74].

Furthermore, deformation twinning is preferred over conventional dislocation slip at cryogenic temperatures in many alloys, contributing towards better strength and ductility. U720Li under compression was found to have higher CRSS for slip than for deformation twinning, which enabled deformation twinning as dominant deformation mechanism at cryogenic temperatures [75]. Recent studies involving Alloy 625 and GH3536 alloy has confirmed the deformation twinning contributing towards improved strength and ductility at cryogenic temperatures [76, 77]. Thus, different deformation mechanisms are observed in superalloys depending on the temperature and loading conditions.

2.2.1 Load redistribution

The occurrence of shearing or looping dictates the load redistribution between γ and γ' in γ'-strengthened Ni-base superalloys. The load redistribution between and within the matrix and particle phases has therefore been studied extensively as a function of particle size and deformation temperature. Daymond et al. [12] investigated the load distribution between γ and γ' of Udimet 720Li using in-situ neutron diffraction and found a strong temperature dependence on the deformation behavior. They observed load transfer from γ' to γ up to 500 °C, whereas the opposite scenario was noticed at higher temperatures. This behavior was suggested to be associated with the previously discussed change from octahedral to cube slip in γ'.

Later, Grant et al. [8] studied RR1000 using a similar experimental setup and observed a γ' size dependence of the deformation mechanisms. On the one hand, smaller particles undergo deformation through shearing by pairs of dislocations leading to co-deformation of γ and γ' without load redistribution. On the other hand, the larger particles lead to both shearing and Orowan looping, which is responsible for the initial co-deformation followed by distinct load partitioning. Similar behavior was found to be consistent at higher temperature (750 °C) with no evidence of cube slip [14]. Furthermore, the evolution of lattice strains during tensile and creep at high temperatures were studied in single-crystal [13, 78, 79] and polycrystalline [8, 12, 14, 80–84]

superalloys. These studies are mostly aimed at understanding the difference in the elastic lattice strain between grains (of different orientations) and between matrix and particle phase during different deformation conditions.

These studies were all devoted to superalloys with high γ' volume fraction, mostly above 0.45. A study of Waspaloy with low γ' volume fraction (around 0.25) was an exception, where the load redistribution between γ' and γ was studied for bimodal microstructure (combination of few larger and many smaller γ' particles) at room temperature [80, 85]. However, the effect of microstructure variables, such as size of γ' particles, and deformation temperatures on the load distribution between matrix and particle phase was not investigated. Thus, there is a need to understand the load redistribution in low γ' volume fraction superalloys as a function of particle size and deformation temperature. In this work, we use the recently developed Haynes 282 with a volume fraction $\approx$0.2 as a representative material for low γ' volume fraction superalloys. Particularly, the size of γ' can be tailored for Haynes 282 and obtain wide variety of microstructures [86–88].

2.2.2 Haynes 282

Haynes 282 has a unique combination of creep strength, fabricability and thermal stability with superior resistance to strain age cracking during welding, which is desirable for gas turbine applications [89, 90]. The weldability also makes it a potential candidate for e.g. cryogenic pressure vessels. There have been many studies of Haynes 282 focused on macroscopic mechanical properties including tensile strength [9, 87], creep-rupture [16, 89], fatigue [91–93] and stress relaxation [94] in association with appropriate electron microscopy analysis.

Recently, Shin et al. [95] reported a change in interaction of dislocations with γ' from shearing to Orowan looping depending on the size of γ'-particles in Haynes 282, similar to high γ' volume fraction superalloys [8]. Also, as mentioned above, the temperature is known to effect the dominant deformation mechanism [9]. Such changes in deformation mechanisms are expected to directly influence the load distribution between γ and γ', which has not been explored. This is indeed, as mentioned above, the case for low γ' volume fraction Ni-base superalloys in general, where the load distribution between γ and γ' are not thoroughly examined, but is vital to develop property prediction models to fully achieve the potential of advanced Ni-base superalloys and develop future alloys. This thesis investigates the effect of γ' size on the load distribution between and within matrix and particle phases in Haynes 282 from 20 K to 1000 K using in-situ neutron diffraction.

2.3 Eutectic high entropy alloys

The eutectic high entropy alloy in the present study ($AlCoCrFeNi_{2.1}$) has a lamellar microstructure consisting of ordered $L1_2$ and ordered B2 crystal structures. The general deformation of $L1_2$ has been discussed for γ' in section 2.1.2, which is valid also for $L1_2$ phase in the EHEA. However, the deformation of $L1_2$ is alloy dependent. Particularly the critical temperature for the transition from octahedral to cube slip varies with alloy composition [96–99]. A further complicating factor is the chemical complexity of the material, as the site occupancy in the $L1_2$ phase is not known. Due to the similarities between previously described γ' and $L1_2$ in EHEA, this section will focus on the other phase, B2. The dominating slip systems in B2 depends on the alloy composition. The initial microstructure analysis (Table. 5.1) revealed enrichment of Ni and Al in the B2 phase. The strong tendency to form aluminides suggests that the structure of the B2 phase is based on either NiAl, FeAl or CoAl in $AlCoCrFeNi_{2.1}$. We therefore chose to consider all three possible B2 aluminides for the discussion of B2 behavior.

2.3.1 Deformation of ordered B2

The B2 crystal structure has the primitive cubic lattice with a two atom basis at body centered and corner positions in the unit cell as shown in Fig. 2.8. The deformation in B2 structure occurs via slip mostly on the {110} and/or {112} planes depending on the binary elements and deformation conditions. The potential slip directions include ⟨001⟩, ⟨011⟩ and ⟨111⟩, where ⟨001⟩ is the shortest lattice vector but ⟨111⟩ is the close packed direction. All potential slip directions in the slip plane $(0\bar{1}1)$ are highlighted in Fig. 2.8.

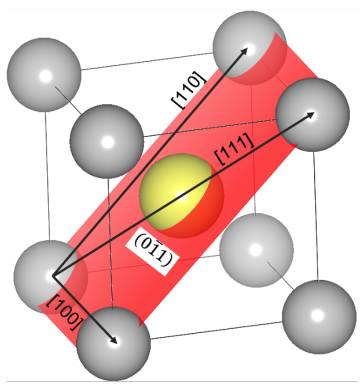

Figure 2.8: Schematic of B2 crystal structure with highlighted $(0\bar{1}1)$ and different slip directions are marked

Numerous studies on NiAl including in-situ neutron diffraction have confirmed the $\{110\}\langle 001\rangle$ as the active operative slip system between 300 and 900 K [100–102]. Non-$\langle 001\rangle$ ($\langle 011\rangle$ and $\langle 111\rangle$) slip have been reported to occur only under very special conditions. For example, $\langle 011\rangle$ was found to be active at very small strains between 850 and 900 K [103], otherwise the samples tested for large strains above and below this temperature range were found to show $\langle 001\rangle$ dislocations. Also, $\langle 011\rangle$ dislocations were noticed in room temperature tests of extruded polycrystalline NiAl with some additions of Ti and Mo. Later, the $\langle 001\rangle$ dislocations were found to be dominant over $\langle 011\rangle$, which were believed to form due to interaction of gliding $\langle 001\rangle$ dislocations during the extrusion process [104, 105]. Another attempt to study the non-$\langle 001\rangle$ dislocations includes deformation of bicrystals at room temperature and 933 K, which didn't provide strong arguments in favour of the existence of non-$\langle 001\rangle$ slip vectors [100]. From the mentioned experimental observations, which agrees with theoretical predictions, the dominant slip system in NiAl is $\{110\}\langle 001\rangle$ over a range of temperatures.

On the other hand, the dominant slip system in FeAl is $\langle 111\rangle\{112\}$ at both room and cryogenic temperatures (77 K), while high temperature deformation occurs through $\langle 111\rangle\{101\}$ slip [106, 107]. Furthermore, Yoo et al. [107] have reported different slip systems for many intermetallics including FeAl and NiAl. Among the three aluminides, CoAl has received the least attention in the literature due to the brittle behavior before the ductile-to-brittle temperature [108]. Yaney et al. [109] reported that the polycrystalline CoAl was extruded at 1505 K and $\langle 001\rangle$ dislocations were observed on both $\{110\}$ and $\{100\}$, while $\langle 111\rangle$ dislocations were found on $\{1\bar{1}0\}$ planes. In addition, Vailhé et al. [110] performed simulations using embedded atom method potentials of Co and Al and discussed all possible defects, planar faults and dislocation core structure in CoAl and suggested the deformation occurs on $\langle 111\rangle\{110\}$ slip system.

Extrapolation of the behavior of binary B2 aluminides to more complex materials is, however, unreliable. Feuerbacher [111] showed that slip in 28Al-20Co-11Cr-15Fe-26N B2 high entropy alloy occurred in $\langle 111\rangle\{112\}$ systems, similar to FeAl, although Ni is the dominating element, followed by Co. Notably, the chemical composition of the B2 phase in $AlCoCrFeNi_{2.1}$ is 21Al-15Co-14Cr-15Fe-35N, which is not too far from the alloy used in [111]. In conclusion, the B2 phase can have different slip systems based on the alloy composition and site occupancy as discussed above. In this work, the dominating slip system in the present B2 phase is unknown.

2.3.2 Deformation of $AlCoCrFeNi_{2.1}$ EHEA

In the $AlCoCrFeNi_{2.1}$ EHEA the two ordered phases, $L1_2$ and B2, essentially form a composite of two intermetallics. It is intriguing to explore the interactions between the ordered phases, which account for the balanced strength and ductility over a wide temperature range. Muskeri et al. [34] performed dedicated deformation studies through compression test of micro-pillars of $L1_2$, B2 and bicrystals containing both phases to understand the phase-specific mechanical behavior. They reported higher CRSS in B2 but a higher elastic stiffness of $L1_2$. The combination of nano and micro-indentation tests revealed that the deformation is largely controlled by hard B2 phase rather than soft $L1_2$. Further, the compression of bi-crystal micro-pillars showed early yielding of $L1_2$ compared to B2 without cracking or separation of the interface, which indicates a strong interphase boundary. This was explained by movement of screw-like partials on fcc {111} interfacial planes, as studied through molecular dynamic simulations of fcc/B2 composite materials with K-S orientation relationship [32]. Moreover, the in-situ tensile tests of $AlCoCrFeNi_{2.1}$ in a transmission electron microscope (TEM) suggested the semi-coherent interfaces contributes to improving the plastic deformation of B2 and avoids cracking for better fracture toughness, as dislocation activity in B2 was promoted by pile-ups at phase boundaries [29]. Such complex interplay between soft and hard ordered phases with strong phase boundaries certainly requires thorough understanding of stress and strain distribution between the phases during plastic deformation.

Load distribution investigations are usually performed on bulk specimens rather than at the micro-scale to preserve the complex elastic interactions between phases and grains with different orientations. Typically in-situ diffraction measurements during loading tests are ideal to gauge the distribution of elastic lattice strains between and within phases of polycrystalline materials. Lu et al. [112] studied the load distribution within the the soft $L1_2$ phase in $AlCoCrFeNi_{2.1}$ using in-situ synchrotron diffraction at room temperature. They observed the large elastic anisotropy among five measured orientations, followed by large lattice strains along (200) and (311), which agrees with traditional behavior of fcc alloys. However, the behavior of B2 phase and load distribution between phases were not investigated. Thus, the load distribution between $L1_2$ and B2 is unknown and must be revealed in order to understand the resulting deformation mechanisms during plastic deformation. Moreover, the deformation of $AlCoCrFeNi_{2.1}$ has been studied at cryogenic temperatures [36, 37] and it was found that slip is the active mechanism, while slip along with twinning were found to be dominating at elevated temperatures [28, 35]. Nevertheless, there has been no studies on load redistribution at elevated or cryogenic temperatures, in spite of the promising properties. This thesis aims to study the effect of deformation temperature on the load distribution be-

tween and within $L1_2$ and B2 phases from 77 K to 973 K in $AlCoCrFeNi_{2.1}$ EHEA using an in-situ neutron diffraction.

CHAPTER 3

NEUTRON SCATTERING

Neutrons were discovered by the British physicist James Chadwick in 1932 who won the Nobel prize for his work in 1935 [113]. Neutron scattering is an excellent research tool to study the structure and dynamics of materials on the atomic scale (nm). In general, neutron scattering is a popular technique in the fields of solid state physics and crystallography. With time it has found its way into various fields such as medicine, biology, earth sciences, planetary science, engineering materials, polymers, cultural heritage and so on.

3.1 Neutron properties

Neutrons are nuclear particles with a mass m_n = 1.675×10^{-27} kg, which is close to that of a proton [114]. Unlike other particles, neutrons has long mean lifetime (880 s) which makes them suitable for scattering experiments, usually lasting a fraction of second [115]. Neutrons are electrically neutral and interact directly with the nuclei of the atoms in the specimen. They have a negative magnetic moment μ = -9.6491 x 10^{-27} (JT^{-1}) which has a tendency to align anti-parallel to an applied magnetic field. This non-zero magnetic moment of neutrons enables them to be used in investigations of microscopic magnetic structures [116] to study the magnetic properties of materials.

Neutrons exhibit particle-wave duality, meaning they possess both particle and wave-like nature as per quantum mechanics [117]. Hence, neutrons are not only associated with moving objects which have momentum and kinetic

energy, but also acquire wavelength and frequency. According to de Broglie relationship [118], the wavelength is defined as

$$\lambda = \frac{h}{m_n v} \tag{3.1}$$

and the kinetic energy (E) in Joules (J) is given as

$$E = \frac{h^2}{2m_n \lambda^2} \tag{3.2}$$

Here, λ is wavelength (m); v is velocity and $h = 6.625 \times 10^{-34}$ J s is Planck's constant.

Varying the wavelength and energy of neutrons enables a wide variety of scattering measurements on different materials. Thus, neutrons are classified based on the range of wavelengths and energy as shown in the Table. 3.1.

Table 3.1: Neutrons are classified and given common names based on energy ranges

Type	λ **(Å)**	**Energy range, meV**	**Origin**
Ultra cold	> 40	< 0.05	Special source < 4 K
Cold	2.4 - 40	0.05 - 14	H_2 moderators at 25 K
Thermal	0.6 - 2.4	14 - 200	H_2O moderators at 300 K
Hot	0.3 - 0.6	200 - 1000	Graphite moderators at 2000 K
Epithermal	< 0.3	10^3 - 10^6	Background from moderators

The number of neutrons generated by the source is measured as neutron flux (Ψ) and it is defined as the neutron rate per unit area and the units are n/cm^{2}s.

$$\Psi = \frac{\text{Number of neutrons hitting on a surface per second}}{\text{surface area perpendicular to the neutron beam direction}} \tag{3.3}$$

During the neutron scattering experiments, the average incoming flux lies in the range 10^5 to 10^9 n/(cm^{2}s).

3.2 Generation of neutrons

There are mainly two methods to generate neutrons for scattering experiments to investigate the materials.

- **Reactor sources:** In nuclear reactors, the neutron-induced fission reactions are used to produce stable neutrons. This process occurs when a

heavy ^{235}U nucleus absorbs a neutron and later splits into two or more stable lighter nuclei along with generation of few free neutrons (≈ 2.4) per fission reaction (Fig. 3.1(a)). One of the free neutrons will further cause fission in another ^{235}U leading to a chain reaction. The remaining neutrons which are not part of fission and absorption will be passed through the moderators to achieve optimum velocities and used for scattering experiments. Typically, the reactor source involves generation of continuous neutron beams with high flux, which are usually pulsed through monochromators to select a specific wavelength for the experiment. In addition, pulsed beams can be generated from continuous flow of neutrons using mechanical choppers.

Some of the well known reactor sources includes Institut Laue-Langevin (ILL), France; IBR-2, Dubna, Russia; NCNR, NIST, USA; HFIR, Oak Ridge, USA; OPAL, ANSTO, Australia; HANARO, South Korea.

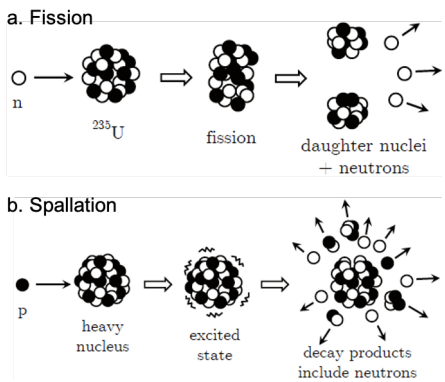

Figure 3.1: Neutrons are generated by two methods; (a) Fission and (b) Spallation [119]

- **Spallation sources:** Nuclear spallation involves bombarding a heavy metal target (W, Hg or Pb) with high energy particles, typically accelerated protons pulses. Upon collision, the proton interacts with the target nucleus and brings it into a highly excited state which rapidly decays with the ejection of stable lighter nuclei, neutrons and other fundamental particles (Fig. 3.1(b)). Spallation sources typically generate pulsed neutron beams, where choppers are used to further define the pulse. All neutrons in a pulse are used for scattering experiments unlike the case of reactor sources. Similar to reactor sources, the high velocity neutrons are passed through the moderators to slow down to thermal or cold neutrons based on the type of moderators used at the source. There are neutron guide systems connected to specific instruments and neutrons are transported through them for scattering experiments.

Some of the important spallation sources across the world includes ISIS, RAL, UK; SINQ, PSI, Switzerland (Continuous spallation source); LANSCE, LANL, USA; SNS, ORNL, USA; MLF, J-PARC, Japan; CSNS, China and European spallation source (ESS), Sweden (Open to users from 2023).

These two types of neutron sources are built as dedicated facilities with variety of instruments meant for specific fields of research. All major sources are user facilities, where external research community can access these instruments and perform experiments.

3.3 Neutron diffraction

Neutron diffraction is an elastic scattering technique which provides information about structural properties of matter on the lattice level (Å/nm). The condition for diffraction is given by Bragg's law.

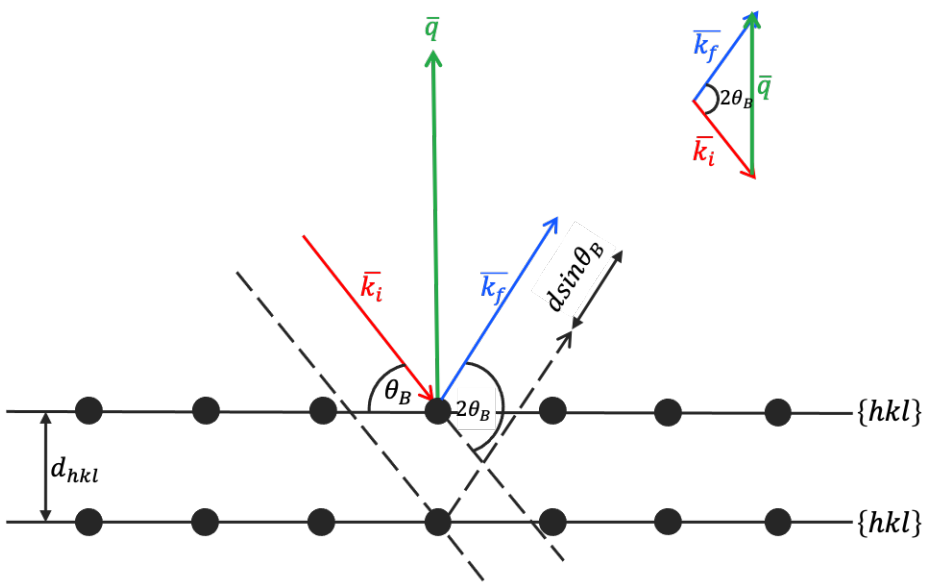

Figure 3.2: Schematic representation of Bragg's law

3.3.1 Bragg's law

Consider a set of crystallographic planes with Miller indices $\{hkl\}$ and the distance between two adjacent planes is d_{hkl} as shown in Fig. 3.2. Here, $\overline{k_i}$ is the wave vector of the incoming beam with magnitude $k_i = \frac{2\pi}{\lambda}$ and $\overline{k_f}$ is the reflected wave vector with the same magnitude as k_i in an elastic scattering event. When the incident neutron waves ($\overline{k_i}$) interact with atoms of the unit cell, only small fraction of them get reflected in a specular way (angle of incidence = angle of reflection). The resultant scattering vector ($\overline{q}$) also called as momentum transfer, is perpendicular to the diffracting plane and calculated using Eq. 3.4.

$$\overline{q} = \overline{k_f} - \overline{k_i} \tag{3.4}$$

The magnitude of $\overline{q}$ is $\frac{4\pi}{\lambda}\sin\theta$ from Eq. 3.4 and Fig. 3.2.

If the coherently reflected waves ($\overline{k_f}$) interfere constructively, this leads to large resultant amplitude. The condition for this is defined by Bragg's law. Bragg's law defines the condition for constructive interference where the path length difference associated with the reflections from the adjacent crystallographic planes is equal to the wavelength of neutrons as given in the Eq. 3.5.

$$n\lambda = 2d_{hkl}\sin\theta_B \tag{3.5}$$

Here, θ_B is the incident and reflection angle or Bragg angle, and n is a positive integer accounting for the fact that the constructive interference occur when the path length difference ($d\sin\theta_B$) of diffracted neutrons equals a multiple of the wavelength. Consequently, for neutrons with a specific wavelength (λ) scattered from planes with distance d, the constructive interference will produce high intensity in the direction $2\theta_B$ relative to the incoming beam according to Eq. 3.5.

According to the Laue condition, the diffraction from a crystal occurs only when the momentum transfer coincides with a reciprocal lattice vector which is expressed as $\overline{G} = h\hat{a} + k\hat{b} + l\hat{c}$, where h, k, l are integers and $\hat{a}, \hat{b}, \hat{c}$ are basis vectors of reciprocal lattice. The Laue condition for diffraction is given by Eq. 3.6.

$$\overline{q} = \overline{G} \tag{3.6}$$

Thus, Laue condition and Bragg's law are equivalent and define *when* diffraction occurs, but the *diffraction intensity* of a given atomic plane $\{hkl\}$ is given by structure factor (F_{hkl}).

3.3.2 Structure factor (F_{hkl})

The structure factor is the sum of the waves scattered by the individual atoms within a unit cell. It is a measure of the amplitude and phase of waves diffracted from the crystal planes defined by Miller indices $\{hkl\}$. The mathematical equation of structure factor for diffraction from plane $\{hkl\}$ is given below.

$$F_{hkl} = \Sigma_i \; b_i e^{2\pi i(hx_i+ky_i+lz_i)} \tag{3.7}$$

Here, the sum of all i atoms in the unit cell with (x_i,y_i,z_i) positional coordinates are considered, and b_i is the scattering length of i^{th} atom. It is important to observe b, whose value changes based on the atom or isotope and source of radiation. For X-rays, b depends on the interaction of outermost electrons of an atom and follows a specific trend with increase in atomic number. However, neutrons interact with nucleus of an atom and b doesn't have any trends unlike X-rays. The intensity (I_{hkl}) of a diffracted beam is directly proportional to the squared amplitude of the structure factor ($I_{hkl} \propto |F_{hkl}|^2$) whose value depends on b, position of atoms (x,y,z) and (hkl) Miller indices.

For instance, the structure factor can be calculated for fcc, which according to Chapter 2 can be described by a simple cubic lattice with four atom basis. Here, the atoms are located at corner (0,0,0) and face centered positions (1/2,1/2,0), (1/2,0,1/2), (0,1/2,1/2). By using Eq. 3.7.

$$F_{hkl} = b(e^{i[2\pi(0)]} + e^{i[2\pi(\frac{h+k}{2})]} + e^{i[2\pi(\frac{k+l}{2})]} + e^{i[2\pi(\frac{l+h}{2})]})$$

$$F_{hkl} = b(1 + e^{i\pi(h+k)} + e^{i\pi(k+l)} + e^{i\pi(l+h)})$$

If the (hkl) is unmixed, meaning all even or all odd gives $F^2_{hkl} = 16b^2$. Thus, the intensity of Bragg peaks (111), (200), (220) and (311) are possible to measure from the γ matrix phase (fcc) of Haynes 282 in this work. Please note that for a solid solution, like γ in Haynes 282, b is the average scattering length of the solute atoms. Otherwise, if the (hkl) are mixed, involving two odd and one even (e.g. 112) or two even and one odd (e.g. 122) then $F^2_{hkl} = 0$, which leads to zero intensity of planes (100), (211), (210) etc., even though Bragg's law is satisfied.

Similarly, the structure factor for $L1_2$ phase (γ'-Ni_3Al) can be calculated using the atomic positions of Ni (1/2,1/2,0), (1/2,0,1/2), (0,1/2,1/2); Al (0,0,0) and respective scattering lengths of Ni (b_{Ni}) and Al (b_{Al}).

$$F_{hkl} = b_{Al}[e^{i[2\pi(0)]}] + b_{Ni}(e^{i[2\pi(\frac{h+k}{2})]} + e^{i[2\pi(\frac{k+l}{2})]} + e^{i[2\pi(\frac{l+h}{2})]})$$

$$F_{hkl} = b_{Al} + b_{Ni}(1 + e^{i\pi(h+k)} + e^{i\pi(k+l)} + e^{i\pi(l+h)})$$

Thus, the structure factor has two solutions; if (hkl) is unmixed then $F^2_{hkl} = (b_{Al}+3b_{Ni})^2$, and in mixed case, the structure factor depends on the difference

between b_{Al} and b_{Ni} i.e., $F_{hkl}^2 = (b_{Al} - b_{Ni})^2$. Hence, one can measure all diffracted peaks as the intensity is non-zero for all scattered reflections. As described in Chapter 1 (section 1.3), the γ' phase in Haynes 282 is not purely Ni_3Al and Ti can substitute for Al in the $L1_2$ lattice. As b_{Ti} is negative, incorporation of Ti on Al sites leads to a large difference between b_{Ni} and b_{Ti} and gives good contrast from superlattice peaks of γ' in Haynes 282. Thus, the superlattice peaks of γ' in Haynes 282 are more readily measured using neutrons compared to X-rays.

Likewise, the structure factor can be calculated for NiAl-B2 crystal structure, which is the hard phase in as-cast $AlCoCrFeNi_{2.1}$. By placing the unit cell origin at the Al site, we get Al atoms at (0,0,0) and Ni atoms at (1/2,1/2,1/2).

$$F_{hkl} = b_{Al}[e^{i[2\pi(0)]}] + b_{Ni}(e^{i[2\pi(\frac{h+k+l}{2})]})$$

$$F_{hkl} = b_{Al} + b_{Ni}(1 + e^{i\pi(h+k+l)})$$

Similar to $L1_2$, we have two solutions for structure factor of B2. If (hkl) are even, then $F_{hkl}^2 = (b_{Al}+b_{Ni})^2$, in odd combination, $F_{hkl}^2 = (b_{Al}-b_{Ni})^2$. Thus, all diffracted Bragg peaks can be measured with non-zero intensity similar to the case of $L1_2$. However, there are other elements (Fe,Co,Cr) in EHEA which can occupy for both $L1_2$ and B2 lattice, then the F_{hkl}^2 changes as the scattering is not only from Al and Ni atoms. Thus, the effective scattering length for all atomic positions ($\overline{b}_{body}$ and $\overline{b}_{corner}$) needs to be considered for the structure factor calculation.

3.3.3 Time-of-flight neutron diffraction

While angle resolved neutron diffraction with monochromatic beams is commonly used at continuous sources, the production of pulsed beams opens up the possibility for energy dispersive techniques using the time-of-flight (TOF) method. The neutron pulses are passed through choppers to select the energy or wavelength range suitable to study the specimen under investigation. TOF method is based on de Broglie wavelength relationship (Eq. 3.1), where neutron wavelength is inversely proportional to its velocity. In other words, the neutrons with short wavelength reach the sample earlier than the longer wavelength neutrons from the source. As the arrival time of each neutron pulse at the detector (t) and the distance travelled by them are known, one can calculate the velocity and hence the wavelength as shown in Eq. 3.8.

$$\lambda = \frac{h}{m_n} \times \frac{t}{L} \tag{3.8}$$

Here, L indicates the distance between source and detector (in meters) and t is the TOF in s, respectively. Instead of measuring the intensity at different

Bragg angles, TOF allows collection of the entire spectrum at a fixed Bragg angle as a function of TOF, as shown in Fig. 3.3. Combining the Eq. 3.5 and Eq. 3.8, d-spacing can be obtained using t and other constants of instrument with fixed Bragg angle (θ_B) as shown in Eq. 3.9.

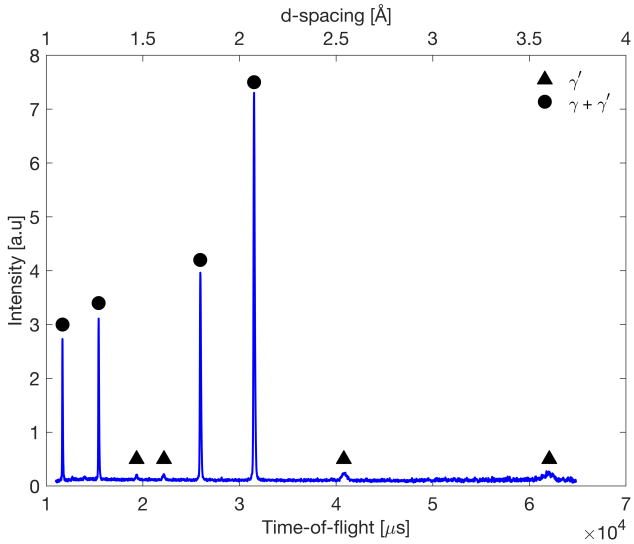

Figure 3.3: Typical diffraction pattern of Ni-base superalloy (Haynes 282) measured at ENGIN-X

$$d = \frac{h}{2 \sin \theta_B m_n L} t \tag{3.9}$$

TOF neutron strain scanners are popularly used for in-situ mechanical testing of materials. Placing detectors with a limited acceptance angle (defined by radial collimators) at $\pm 90^\circ$ creates a cubic gauge volume with defined diffraction vector(s) aligned to the loading (and transverse) directions during an in-situ mechanical testing. The schematic and geometry of an engineering diffractometer for in-situ testing are thoroughly discussed in Chapter 4. In summary, only TOF neutron strain scanners can measure entire spectra at a particular Bragg angle involving intensities of all grains aligned in the tensile and transverse direction, which is useful for studying phase-averaged and orientation-specific behavior during the in-situ tensile testing, as performed in this work.

CHAPTER 4

EXPERIMENTAL METHODS

This chapter is dedicated to the description of the experimental methods in this work. It starts with heat treatments of Haynes 282 to achieve two model microstructures for in-situ tensile tests. Subsequently, neutron strain scanners are discussed in detail along with the two instruments used in this work. Later, the data analysis and measurable quantities from the in-situ neutron diffraction experiments are presented. Further, the final sections are devoted to complimentary techniques.

4.1 Generation of model microstructures of Haynes 282

The chemical composition of Haynes 282 is shown in Table. 4.1. Following the discussion in Chapter 2, small particles are expected to undergo shearing, while particles above a critical size should lead to looping. In order to investigate the effect of the deformation mechanism (controlled through the particle size) on the load partitioning, samples were subjected to two types of heat treatments to achieve fine and coarse γ' particles, respectively. In case of fine γ', the samples were solution treated at 1120 °C and water quenched to dissolve

Table 4.1: Chemical composition of Haynes 282 by wt. %

Cr	Co	Mo	Ti	Al	Fe	B	P	S	Si	Ni
19.52	10.33	8.56	2.13	1.52	0.66	0.005	0.002	0.002	0.6	Bal

carbides and γ' phases from the previous processing. Later, they were heated to 1010 °C for precipitation of carbides at the grain boundaries and air cooled to room temperature. The final step was focused on ageing, involving precipitation of γ' particles at 788 °C for 8 hours followed by air cooling. The large undercooling below the γ' solvus ($\approx$ 1000 °C) provides a large driving force for nucleation and slow growth leading to many small γ' particles. The size of γ' in the final microstructure was $\approx$ 20 nm with a volume fraction of around 0.2 as shown in Fig. 4.1(a). For coarse γ', the heat treatment was continuous without intermittent water quenching. It starts with solution treatment at 1120 °C for half an hour followed by controlled cooling at 10 °C/min to 950 °C, where the temperature was held for half an hour. This step involves both nucleation of carbides and sparse γ'. Due to very small undercooling, only few γ' nuclei are formed, which grow rapidly at 950 °C. Then, the samples were cooled slowly at 0.1 °C/min until 500 °C followed by water quench. The very slow cooling in this step increases the volume fraction of γ' (which is very low at 950 °C) by growing existing particles under quasi-equilibrium conditions without further nucleation. The final microstructure is shown in Fig. 4.1(b), which has a γ' size of $\approx$ 200 nm and similar volume fraction as the fine γ' condition in the matrix. The overview of the microstructure is shown in Fig. 4.1(c) having coarse grains with annealing twins.

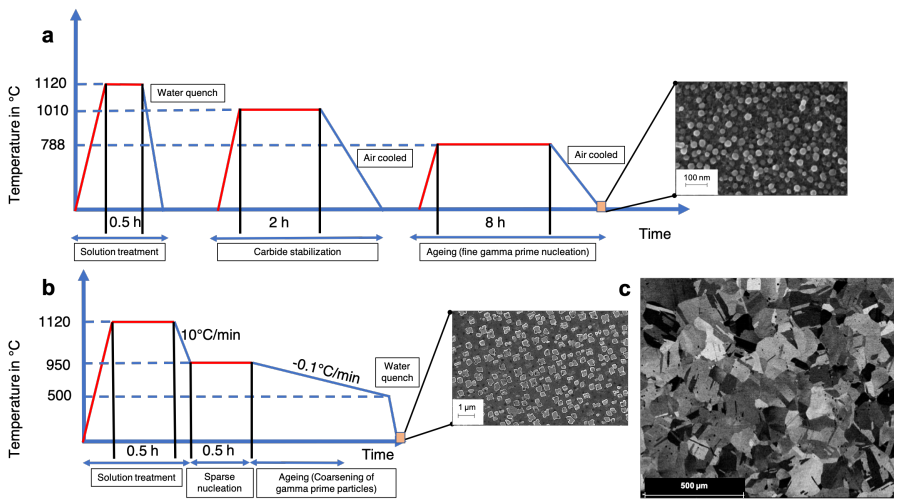

Figure 4.1: Heat treatments on Haynes 282 to obtain (a) fine γ', (b) coarse γ' and (c) overview of coarse grains with annealing twins.

4.2 Neutron strain scanner (NSS)

NSS has been one of the most popular techniques to measure the elastic strains (and thus stress) in engineering materials based on the internal crystal lattice as strain gauge. The strain measurements were proposed and developed in the early 1980s at the Harwell Laboratory, UK [120] to investigate the residual stresses in polycrystalline engineering specimens [121, 122]. Later, NSS were extended to measure stresses during in-situ mechanical testing of materials with the help of different sample environments built around the neutron strain scanners at large scale facilities. These measurements are performed at instruments at both reactor sources and spallation sources, but the latter has the advantage to measure multiple Bragg peaks at a fixed $2\theta_B$ by simultaneously utilising the entire wavelength spectrum in the neutron pulses, which is suitable for this work. As only TOF based NSS of spallation sources were used in this work, the description is limited to such instruments.

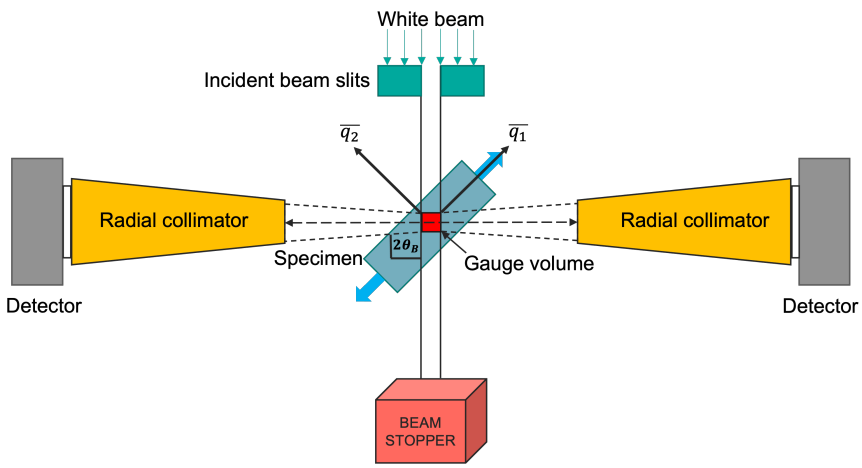

Figure 4.2: Schematic of TOF neutron strain scanner with two detectors placed at $2\theta_B = \pm\ 90^\circ$ to the incident neutron beam and the sample is aligned at 45° [123]

The size of the incoming beam is controlled by slits. Diffraction will occur all along the path of the incoming beam through the specimen, but the radial collimators define the volume from which neutrons are allowed to reach the detectors, which are placed at ±90° as shown in Fig. 4.2. This volume is called the neutron gauge volume (GV), and the size and shape is defined by the slits and radial collimators. In general, the size of the GV is in the order of mm^3, and with the described set-up it has a nearly cuboidal shape. By moving the sample so that the region of interest coincides with the GV, it is possible to measure diffraction signals only from a selected volume in the specimen.

The two detectors are used to determine two orthogonal momentum transfer vectors, $\overline{q_1}$ and $\overline{q_2}$, which can directly measure the d-spacings (i.e. strain) in two orthogonal directions. The use of cuboidal GV allows measurement of signals in different direction from exactly the same GV by rotating the sample 90°. This permits determination of strains in all three principal directions by only one rotation. Further, the transmitted beam in the path are absorbed by the beam stopper for safety and avoid further scattering and radiation in the experimental hall.

In this work, samples were subjected to in-situ tensile testing and both $\overline{q_1}$ and $\overline{q_2}$, which correspond to the loading and transverse axes respectively, were measured simultaneously, as shown in Fig. 4.2. There was no rotation of the sample during the in-situ loading experiments and thus only axial and one transverse direction were measured, assuming symmetry around the tensile axis. During in-situ tests, diffraction patterns were collected at different load/strain levels throughout the deformation. The measured diffraction spectra from the GV are subsequently analysed (as will be described in section 4.4) to allow tracking for the lattice strains, intensity and peak width, as a function of load/strain. In the present work, the in-situ neutron diffraction experiments were performed at ENGIN-X and TAKUMI engineering diffractometers, which are known for complex in-situ mechanical testing of engineering materials.

4.3 Neutron engineering diffractometers

4.3.1 ENGIN-X at ISIS

ENGIN-X is a TOF based neutron strain scanner located at Target Station 1 of ISIS Neutron and Muon source, Rutherford Appleton Laboratory, UK [124, 125]. This instrument is built around 50 m away from the target. As described in section 3.2, moderators are used to slow down the speed of the generated fast neutrons to optimum levels for any given instrument. ISIS uses methane moderators to achieve a wide wavelength range, which is suitable for most engineering materials. The decelerated neutrons are passed through neutron guides to transport the pulsed neutron beam from the moderator to the sample at ENGIN-X. Note that the choppers define the wavelength range of the neutron pulse, and thus the accessible d-spacing range. Optimum chopper settings are selected based on the material and peaks of interest. The top view of the ENGIN-X instrument is very similar to the schematic of TOF based NSS shown in Fig. 4.2. The radial collimators are placed just before the two detectors at ±90° to the incident beam, and have adjustable gauge width options from 0.5–4 mm. The coverage angle for each detector is about ± 16° in the horizontal plane and ± 21° in the vertical plane [124]. Furthermore,

ENGIN-X uses integration of neutron counts during pre-determined interval(s) for histogramming the diffraction spectra measured from the sample GV. The histogramming is correlated with the stress-rig data, where the calculated average stress-strain data is associated with each diffraction spectra measured during the tests.

Each test was initially performed in load control mode, since the change in displacements are relatively small and hard to pre-define in the elastic regime. After the yield point, the relative change in the loads are comparably small which is why displacement control was chosen for the rest of the test. The strain in the sample during the tensile tests was measured using an extensometer and a thermocouples was attached to the sample to monitor the temperature. Tests at cryogenic temperatures were conducted using a dedicated evacuated chamber as shown in Fig. 4.3(b), where samples can be loaded up to 100 kN in the temperature range 6 K to 300 K [126–130]. For high temperature tests, a different chamber was used, where the sample was heated by radiant air furnace on the stress rig [131] as shown in Fig. 4.3(a).

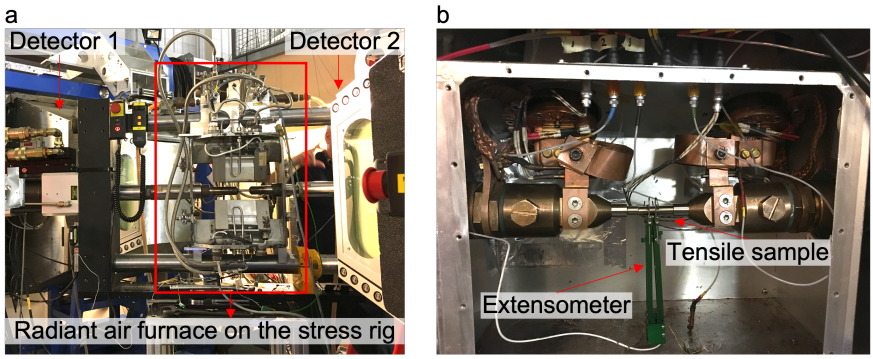

Figure 4.3: (a) Front view picture of ENGIN-X diffractometer with stress rig placed in the middle of two detectors. (b) sample environment chamber for in-situ tensile tests at cryogenic temperatures (6 K to 300 K)

Using these sample environments, we performed in-situ tensile tests of Haynes 282 at 20 K, 100 K and room temperature (300 K) with a counting time of $\approx$ 1 hour per loading point in order to obtain adequate signal to noise ratio, particularly from the γ' superlattice peaks. The obtained diffraction patterns with a d-spacing range of 1 to 3.7 Å cover the Bragg peaks from (311) to (100). EHEA samples were tested at 77 K, 300 K and 673 K with a counting time of $\approx$ 20–30 minutes per loading point. Both $L1_2$ and B2 peaks within d-spacing range of 0.4 to 2.2 Å were measured along loading and transverse axes simultaneously. At each load/displacement level, the initial period (5-10 minutes), depending on the temperature, was excluded from the analysis to

allow for initial stress relaxation which can affect the lattice strain calculations. More details can be found in the supplementary material of **Paper IV**. For all tests, the slits and radial collimators were selected to measure a GV of $4 \times 4 \times 4$ mm^3 from the tensile samples.

4.3.2 TAKUMI at J-PARC

TAKUMI is an engineering materials diffractometer located at the Materials and Life Science Experimental Facility (MLF) of the Japan Proton Accelerator Research Complex (J-PARC), Japan [132, 133]. MLF has a spallation source and generates pulsed neutron beams which are passed through poisoned decoupled hydrogen moderators to slow down the neutrons. TAKUMI is 40 m away from the spallation source and the setup (see Fig. 4.4(a)) is almost identical to the ENGIN-X instrument with two detector placed at $\pm 90^\circ$ and the stress-rig mounted between them at 45° to the incoming beam. This setup measures a near cuboidal GV from the sample with a coverage of $\pm 15^\circ$ horizontally and $\pm 16^\circ$ vertically for each detector. TAKUMI has an advantage over ENGIN-X with respect to the data recording, as an *event-based* data acquisition method has been implemented. Each detected neutron is individually time-stamped and associated with an incoming pulse. This allows the histogramming to be performed after the test at arbitrary intervals. This is referred to as time-slicing, since time intervals for histogramming are selected during the data analysis after the experiments. The average strain and stress in each time interval is calculated from the stress-rig data and associated with corresponding diffractograms. Due to the high flux of neutrons at TAKUMI, typical time intervals for slicing are in the range of 5–15 minutes compare to $\sim$1 hour per point at ENGIN-X in the case of Haynes 282. TAKUMI utilises a software application kit called EMAKi [134, 135], which is used for data acquisition, reduction and visualization.

Unlike ENGIN-X, step-wise loading is not necessary at TAKUMI, due to high flux and event based data acquisition method. This permits the study of transient behaviors in materials. For example, the elasto-plastic transition during tensile tests at higher temperatures would involve stress relaxation when step-wise loading or holding the cross-head at regular intervals is used. Such tests need to be performed almost without any holding steps to avoid significant stress relaxation (except for creep studies) at high temperatures. Thus, TAKUMI has an advantage over ENGIN-X particularly for high temperature in-situ mechanical studies.

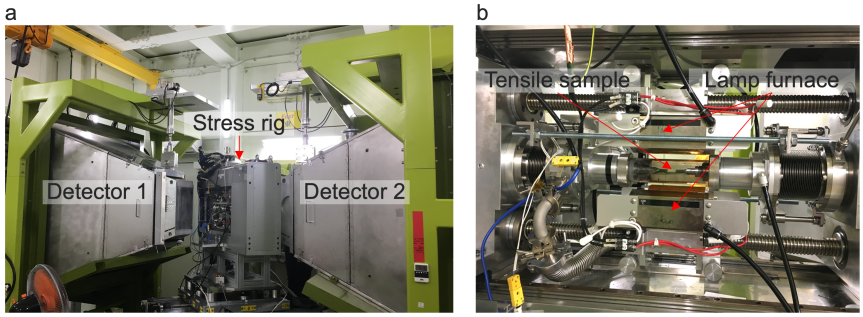

Figure 4.4: (a) Picture of TAKUMI engineering materials diffractometer with stress rig placed at 45° to the incoming beam between the two detectors located at ±90°. (b) sample environment chamber for in-situ tensile tests at high temperatures.

In this thesis, TAKUMI was chosen for in-situ tensile test of Haynes 282 and EHEA at the highest temperatures. As mentioned earlier, two uni-modal microstructures, namely fine γ' and coarse γ' were considered for the in-situ tensile tests of Haynes 282. The main focus of these experiments was to understand the effect of particle size and deformation temperature during tensile testing of Haynes 282 at high temperatures. Tensile samples with dimensions 6 mm diameter and 35 mm gauge length were used to perform tests at 650 and 730 °C, while measuring the diffraction during deformation from the $5 \times 5 \times 5$ mm^3 GV. The chopper settings were adjusted to measure d-spacing range of 1–4 Å, which recorded the fundamental and superlattice peaks. The change in displacements were directly measured through the cross-head displacement of the stress-rig. In all tests, the samples were heated to the test temperature using a lamp furnace [136] (see Fig. 4.4(b)) and held for 30 minutes for homogenization. This is followed by constant load steps, where the sample was held at pre-defined loads for 5 minutes at each point in the elastic regime and continuous deformation corresponding to a nominal strain rate 10^{-6} s^{-1} was then applied until the end of the test. During the constant load steps, no significant stress relaxation was noticed and all diffracted neutrons were counted during the entire holding time.

For EHEA, the in-situ tensile test was performed at 700 °C with the sample dimensions of 6 mm diameter and 40 mm gauge length in as-cast condition. Test procedure for EHEA was the same as Haynes 282 except for chopper settings, which were used to select a d-spacing range of 0.3 to 3 Å to measure Bragg peaks of $L1_2$ and B2. Unlike Haynes 282, the EHEA sample was loaded continuously at a strain rate 10^{-6} s^{-1} throughout the test without any holding steps in the elastic regime.

4.4 Data analysis

The diffraction spectra measured during the tensile tests were reduced using OpenGenie [137] and Mantid [138] applications in case of ENGIN-X and EMAKi software for TAKUMI data. The diffraction pattern is generally analysed with TOF on the X-axis and intensity on the Y-axis (see Fig. 3.3). In this work, the goal was to study the load redistribution through the relative movement of each peak during deformation. Thus, we used single peak fitting to analyse the diffraction patterns measured at different test conditions. GSAS-II software [139] was used to perform single peak fitting for selected peaks using psuedo-Voigt (PV) peak shape function convoluted with two back-to-back exponential functions. The PV peak shape function is a linear combination of Gaussian and Lorentzian peak functions, which is numerically more efficient than the Voigt function. Further, the back-to-back exponential functions are considered to accommodate the peak shape effects from the moderating process. Thus, the total peak shape function involves the convolution of PV peak shape function with back-to-back exponential function, which is implemented in the GSAS-II software as the standard peak shape function for analysis of neutron TOF data.

For Haynes 282, due to coherency between γ and γ', the fundamental fcc γ peaks overlap with the corresponding γ' peaks. The deconvolution of γ and γ' contributions to the composite fundamental peak is not directly possible due to small lattice mismatch, measured to be $\approx$ -0.04% in **Paper II**. However, the (200) and (220) doublets can be deconvoluted using the *d*-spacings obtained from the fits of the corresponding (100) and (110) superlattice peaks through constraining as shown below.

$$d^{\gamma'}_{2h2k2l} = \frac{d^{\gamma'}_{hkl}}{2} \tag{4.1}$$

There are also additional constraints such as γ/γ' intensity ratio and peak width, which are commonly applied during deconvolution of the fundamental peaks in the superalloys. However, these constraints are known to have a large impact on the deconvolution and their accuracy is difficult to assess [13]. Therefore, no such constraints were employed here. The other doublet peaks (111) and (311) were fitted as single peaks, as they do not have equivalent superlattice peaks to apply constraints using Eq. 4.1. For Haynes 282, however, this gave negligible errors, as shown in **Paper I**.

The progressive change in d_{hkl} during deformation can be used to determine the elastic lattice strains (and stress). During continuous deformation of the sample, the diffraction peaks move away from the initial peak positions due to accumulation of lattice strains. These lattice strains are purely elastic, irrespective of the macroscopic plasticity in the specimen and depend on the

stress experienced by the diffracting grains. Thus, NSS allows to measure the anisotropic elastic lattice strains, typically expressed in $\mu\epsilon = 10^{-6}$, within the GV of the sample. For a fixed Bragg angle ($2\theta_B$), the elastic lattice strain (ϵ_{hkl}) from diffracting planes $\{hkl\}$ is determined from the change in interplanar distances d_{hkl} (or equivalent t_{hkl}) as compared with the d^0_{hkl} (or equivalent t^0_{hkl}) measured from the stress-free or reference condition as shown below (Eq. 4.2).

$$\epsilon_{hkl} = \frac{d_{hkl} - d^0_{hkl}}{d^0_{hkl}} = \frac{t_{hkl} - t^0_{hkl}}{t^0_{hkl}} \tag{4.2}$$

In this work, we measured d^0_{hkl} at zero load as reference and any initial internal stresses at zero load are neglected. The movement of individual Bragg peak positions enables the measurements of elastic and plastic anisotropy. Often Pawley or Rietveld refinements are performed on the diffraction spectra to obtain the lattice parameters of the respective phases, which can give a good estimate of average strain in the phase [140, 141]. In this work, there was no proper powder averaging due to the large grain sizes, which limits the analysis to Pawley refinements. However, the Pawley refinements has free intensity parameter and can therefore not reliably fit the two closely overlapping peaks from γ and γ' in the doublets, particularly when the effects of elastic and plastic anisotropy of grains increase during deformation. Thus, the deconvolution of γ and γ' was not successful through whole-pattern refinements in Haynes 282. Instead, we used single peak fitting method for all selected peaks to extract the d-spacing values in order to evaluate the elastic lattice strains in this study. The phase-averaged lattice strains ($\bar{\epsilon}$) were determined as the multiplicity weighted average of the individual peaks [141] in Eq. 4.3.

$$\bar{\epsilon} = \frac{1}{\sum_i w_i} \sum_i w_i \epsilon_i \tag{4.3}$$

Here, w_i is the multiplicity of individual grain families of the respective phase. Moving on, the in-situ neutron diffraction measurements of EHEA were also analysed using single peak fitting method, where distinct $L1_2$ and B2 Bragg peaks were individually fitted to obtain the respective d_{hkl} values. Here, only fundamental peaks were used, as superlattice peaks were too weak to fit with good accuracy. Again, multiplicity-weighted average was used to calculate the phase-averaged strains.

As mentioned earlier, the measured lattice strains are elastic in nature, hence the average stress (σ_p^{hkl}) associated with diffracting $\{hkl\}$ planes can be approximately calculated through Hooke's law as shown below

$$\sigma_p^{hkl} = E_p^{hkl} \times \epsilon_p^{hkl} \tag{4.4}$$

where E_p^{hkl} is the effective stiffness of the $\{hkl\}$ plane and ϵ_p^{hkl} is the elastic lattice strain of $\{hkl\}$ plane in a specific phase. Please note the elastic stiffness

was obtained from the diffraction measurements in the elastic region and it is assumed to be constant throughout the tests. Similarly, the phase-specific elastic lattice strain can be used to calculate the phase-specific stress (σ_p) as shown below

$$\sigma_p = \frac{E_p}{(1+\nu)(1-2\nu)}[(1-\nu)\epsilon_p^a + 2\nu\epsilon_p^{tr}] \tag{4.5}$$

where ϵ_p^a and ϵ_p^{tr} are phase-specific elastic lattice strain in the axial and transverse directions, respectively, ν_p is the Poisson's ratio and E_p is the effective stiffness of the phase. Eq. 4.5 can be simplified to Eq. 4.6, if $\epsilon^{tr} = -\nu\epsilon^{ax}$, i.e. assuming there are only Poisson contractions and no interaction stresses between the phases.

$$\sigma_p = E^p\epsilon^p \tag{4.6}$$

We calculated the σ_p from the EHEA diffraction measurements using both Eq. 4.5 and 4.6, and the values were in good agreement as discussed in **Paper IV**.

In addition to peak positions, peak intensity (I_{hkl}) and full width half maximum (FWHM) of the peak can be obtained. When the instrument broadening is corrected for, FWHM mainly depends on size (for very small diffracting domains) and presence of defects (dislocations). In Haynes 282, the diffractograms of fine and coarse γ' has shown noticeable difference in peak broadening due to the γ' size effect as shown in **Paper I**. In this work, the size broadening is assumed to be constant and the accumulation of dislocations can then be inferred from FWHM. Further, the intensity of individual peaks is proportional to the number of diffracting grains and their multiplicity. An increase in I_{hkl} corresponds to an increase in the number of grains with $\{hkl\}$ aligned with $\overline{q}$ and vice versa, which gives a qualitative measure of texture evolution.

4.5 Complementary techniques

Apart from in-situ neutron diffraction, electron microscopy techniques were used in this work to study the initial and deformed microstructures. The samples were prepared and analysed using scanning electron microscopy (SEM) and transmission electron microscopy (TEM).

4.5.1 Electron channelling contrast imaging (ECCI)

ECCI is a mode of imaging in SEM involving the channelling effect of electrons through a crystal lattice and images with crystallographic orientation contrast is obtained. The electrons travelling parallel to atomic planes without intense interaction leads to electron channelling with minimum back scattering signal.

For orientations when channeling is not possible, electrons produce more back scattering signal, which gives a contrast related to the orientation of the grains.

If the crystals are imperfect, with defects such as dislocations and stacking faults, then the electron beam interacts with inclined planes and a strong back scattered signal is emitted. Local changes in contrast due to defect density allows visualization of the distribution of plastic strain (dislocation density) in the microstructure. In order to get the optimum electron channelling contrast [142], the beam must be parallel and collimated by choosing appropriate aperture size with high beam current. ECCI requires a large beam diameter to receive sufficient signal for imaging, which reduces spatial resolution.

4.5.2 Electron backscatter diffraction (EBSD)

EBSD is an ideal technique to measure crystallographic orientations at the surface of crystalline materials. The set-up includes tilting stage to 70° with respect to the incident beam and back scattered electrons are generated during interaction with the inclined sample. Some back scattered electrons undergo Bragg diffraction and are detected as Kikuchi lines representing the diffracting crystal planes on a phosphor screen (detector) [143]. The recorded Kikuchi patterns are used to determine the orientation of the diffracting crystal.

In general, the presence of texture is visualised using inverse polefigures (IPF) maps. The IPF maps follow a specific color scheme to represent different orientations measured in the microstructure. Alternatively, local misorientation maps are appropriate to look at defect structures. Kernal average misorientation (KAM), grain reference orientation deviation (GROD) and grain orientation spread (GOS) are different ways to represent the misorientations in the deformed microstructure [144]. KAM is based on the misorientation between the point of interest (POI) and a definite set of points around it and therefore related to the local density of geometrically necessary dislocations. GROD measures the misorientation between a point and mean orientation of the grain, which allows characterization of the distribution of plastic strains. GOS is the average measure of misorientation between all points and the mean orientation of each grain and as such it represents the average "degree of deformation" of the grain.

In this study, GROD in combination with KAM are used to interpret the critical features of deformed microstructure of Haynes 282. EBSD was also used to identify the phases and K-S orientation relationship between $L1_2$ and B2 in the EHEA.

4.5.3 Transmission electron microscopy (TEM): Imaging of dislocations

TEM is a unique tool to observe features of microstructures at micro to Å scale with good resolution. TEM is used to study dislocations in this work. In order to observe dislocations, one need to follow the $\overline{G} \cdot \overline{b}$ rule. Here, $\overline{G}$ corresponds to the diffraction vector (indeed a set of planes) and $\overline{b}$ represents the Burgers vector of the dislocation. The sample is tilted with respect to the incident electron beam to alter $\overline{b}$ with respect to $\overline{G}$ and obtain perfect diffraction conditions to observe dislocations. If $\overline{G} \cdot \overline{b} = 0$, diffraction contrast will be minimum and one cannot resolve the line defects. On the other hand if $\overline{G} \cdot \overline{b} \neq 0$, then these defects can be observed in TEM. To do this analysis, the possible combination of the Burgers vectors, $\overline{b}$, and diffraction vector, $\overline{G}$, which satisfies $\overline{G} \cdot \overline{b} \neq 0$ needs to be determined. Table. 4.2 helps in choosing relevant diffraction plane for imaging dislocations [145].

The dot product of $\overline{G}$ and $\overline{b}$ were evaluated at each combination and the result is tabulated. According to $\overline{G} \cdot \overline{b}$ rule, the highlighted yellow colored rows satisfy the $\overline{G} \cdot \overline{b}$ rule to observe dislocations. Hence, either $(\overline{1}\overline{1}1)$ or (200) or both can be chosen to observe and study dislocations. These diffraction vectors exists in specific zone axis, (200) and $(\overline{1}\overline{1}1)$ can be observed in [011]. Hence, one should obtain [011] zone axis using double tilt holder. Selected area diffraction aperture is used to select the two-beam condition at (200) or $(\overline{1}\overline{1}1)$ and the corresponding bright field image was captured.

Table 4.2: The Burgers vectors and diffraction planes of fcc are tabulated as per $\overline{G} \cdot \overline{b}$ rule. Yellow coloured row gives the selected $\overline{G}$ and $\overline{b}$ combinations to resolve dislocations [145].

$\overline{G} \backslash \overline{b}$	$\frac{1}{6}[11\overline{2}]$	$\frac{1}{6}[1\overline{2}1]$	$\frac{1}{6}[\overline{2}11]$	$\frac{1}{3}[111]$
$(1\overline{1}1)$	$\pm \frac{1}{3}$	$\pm \frac{2}{3}$	$\pm \frac{1}{3}$	$\pm \frac{1}{3}$
$(\overline{1}\overline{1}1)$	$\pm \frac{2}{3}$	$\pm \frac{1}{3}$	$\pm \frac{1}{3}$	$\pm \frac{1}{3}$
$(0\overline{2}2)$	± 1	± 1	0	0
(200)	$\pm \frac{1}{3}$	$\pm \frac{1}{3}$	$\pm \frac{2}{3}$	$\pm \frac{2}{3}$
$(3\overline{1}\overline{1})$	0	± 1	± 1	± 1
$(\overline{3}\overline{1}1)$	± 1	0	± 1	± 1

4.5.4 Sample preparation

The deformed samples of Haynes 282 and EHEA were cut parallel to the loading axis using a slow speed saw. The cut samples were mounted and ground using emery sheets followed by polishing using diamond and colloidal

silica to obtain a mirror finish and strain free surface. These samples were observed in scanning electron microscope to examine defect microstructures using ECCI and EBSD techniques.

Later, a 0.5 mm thick slice was sectioned from the deformed sample and further reduced the thickness to 100 μm using series of emery sheets. Subsequently, the slice was punched into discs of 3 mm diameter. These disc samples were subjected to electropolishing using a Struers™ Tenupol-5 twin-jet polishing machine. Ethanol and perchloric acid in 9:1 volume fraction was used as electrolyte. The equipment was operated at 25 V in -30 °C.

CHAPTER 5

RESULTS AND OUTLOOK

This chapter mainly summarizes the important results obtained from the in-situ neutron diffraction measurements of Haynes 282 and $AlCoCrFeNi_{2.1}$ EHEA. In total, there are five papers; the first three consider to Haynes 282 and the next two are associated with $AlCoCrFeNi_{2.1}$ EHEA. More details are given in the respective appended papers. Further, the outlook mentions the future work suggestions.

5.1 Haynes 282

The fine γ' (20 nm) and coarse γ' (200 nm) microstructures were already presented in Chapter 4 (section 4.1) and the overall chemical composition of Haynes 282 is shown in Table. 4.1. These two microstructures were used to study the load distribution between matrix and particle phase as a function of γ' size and deformation temperature using in-situ neutron diffraction. The deformation of samples with fine and coarse γ' microstructures were studied from 20 K–1000 K, and the results are discussed and documented in three manuscripts. In **Paper I**, the load distribution between matrix and particle phases during room temperature deformation is discussed and the dominating deformation mechanisms in the two microstructures are identified. Similar experiments were performed at 20 K and 100 K and the results are presented in **Paper II** in comparison with room temperature deformation (**Paper I**). Finally, the investigation on load distribution at 650 and 730 °C were thoroughly discussed in **Paper III**.

5.1.1 Deformation mechanisms and load distribution at room temperature

The flow curves measured during in-situ neutron diffraction experiments are shown in Fig. 5.1(a), where fine γ' microstructure has higher yield stress since weakly paired coupling is operating, as the size of fine γ' is close to the optimum size (28 nm) [87]. The coarse structure falls in the regime of Orowan looping and/or strong pair coupling resulting in lower levels of strength. The strain hardening behavior is found to be similar for fine and coarse structures (Fig. 5.1(a)), with slightly higher work hardening at higher strains contrary to high γ' volume fraction superalloys [8, 11, 14]. Both microstructures failed at true strains of around 0.2 with no signs of necking before fracture. In addition, elasto-plastic self-consistent (EPSC) crystal plasticity simulations are implemented to predict the deformation behavior of fine and coarse microstructures as shown in Fig. 5.1(a), where the macroscopic stress-strain response were matched with the simulation results.

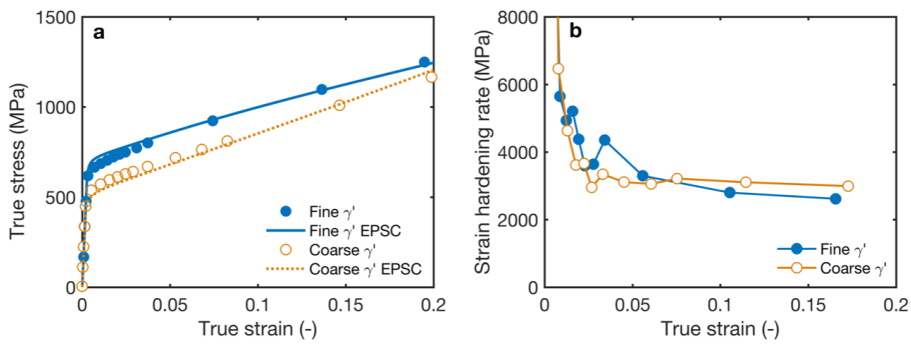

Figure 5.1: (a) Global stress-strain curves for fine and coarse γ' structures with the corresponding predictions from EPSC simulations. (b) Strain hardening curves for both microstructures

Further, the orientation-specific and phase-averaged lattice strains were determined using Eq. 4.2 and Eq. 4.3, respectively. Fig. 5.2 shows the evolution of phase-averaged lattice strain against the macroscopic stress for fine and coarse structures. Initial deformation shows similar elastic stiffness, but upon yielding the lattice strain distribution differs between the two microstructures. In the case of fine γ' (Fig. 5.2(a)), there exists a co-deformation of matrix and particle phase with no redistribution between them after the yield stress at around 640 MPa. This behavior is consistent with previous studies on high γ' volume fraction superalloys [8, 11, 14], where co-deformation occurs due to shearing of small coherent particles in the matrix. On the other hand, the coarse γ' microstructure (Fig. 5.2(b)) shows a significant load redistribution

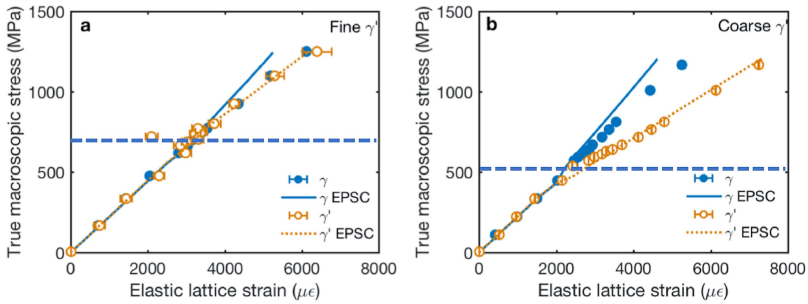

Figure 5.2: Phase-averaged lattice strains in case of (a) fine γ' and (b) coarse γ' microstructures. Markers show experimental data and lines indicate fitted EPSC model. The blue dashed line across the plots indicates the yield stress for reference. Note that when error bars are not visible, they are smaller than the marker size.

between the phases after yielding at ∼510 MPa. Here, the γ matrix undergoes preferential yielding, resulting in stress transfer to the elastically deforming γ' particles. This behavior also agrees with the observation from the high γ' volume fraction superalloys [8, 11, 14], where the coarse γ' structure tends to deform through Orowan looping mechanism. Unlike shearing, it involves single dislocations which circumvents the γ' particles by bowing around them, leaving residual dislocation loops enclosing the particles. Thus, the plastic flow is accommodated in the matrix through dislocations pile up around the γ' particles. A study of high γ' volume fraction superalloys with coarse particle size (130 nm and 230 nm) reported co-deformation of γ and γ' after yielding at room temperature different particle size at room temperature [8]. This sustained over a significant stress range before the significant load transfer to γ' particles occurred. In contrast, no such region of co-deformation was observed for the coarse microstructure of Haynes 282, where only load redistribution occurs directly upon yielding.

Fig. 5.3 shows the distribution of lattice strains of different orientations measured in γ and γ' from fine and coarse microstructures. Both phases exhibit similar elastic anisotropy and pronounced plastic anisotropy upon yielding. During deformation, the load is transferred to the (200)/(100) oriented grains, while (220)/(110) undergoes preferential yielding and (311) remains close to linear in both microstructures. The EPSC simulations are consistent in predicting the evolution of lattice strains for both microstructures.

Furthermore, the deconvoluted (100)/(200) and (110)/(220) behavior of both microstructures is shown in Fig. 5.4. The preferred yielding of (110)/(220) compared to (100)/(200) in the fine microstructure is due to lower elastic stiffness in the (100)/(200) direction which keeps the resolved shear stresses lower. This allows larger elastic strains to be sustained in the (100)/(200)

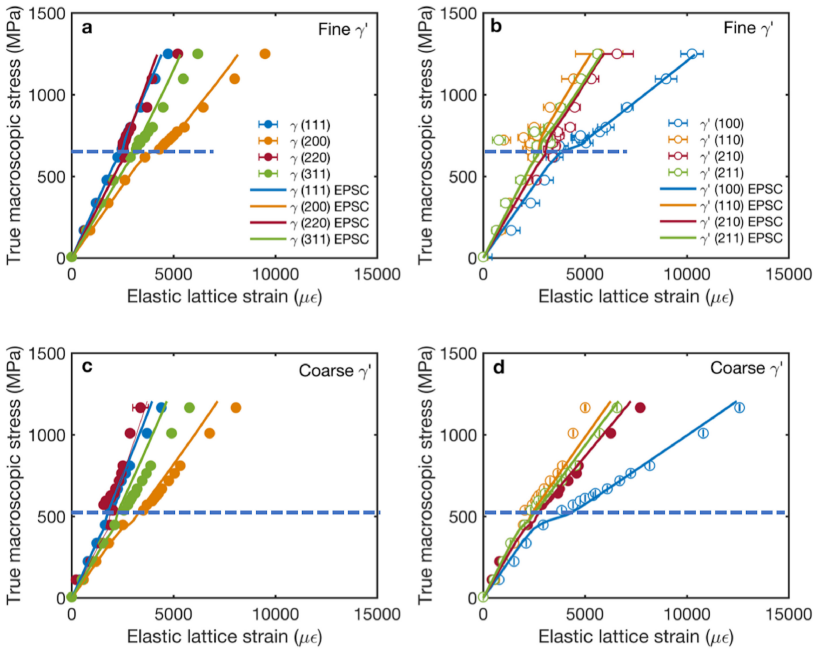

Figure 5.3: Elastic lattice strains against macroscopic (applied) stress for (a) the fundamental fcc peaks, and (b) γ' superlattice peaks for the fine γ' microstructure. Markers show experimental data and lines indicate fitted EPSC model. (c) and (d) show the corresponding figures for the coarse γ' microstructure. The legends are the same as in (a) and (b). Note that when error bars are not visible, they are smaller than the marker size.

direction before yielding. Thus, the load is transferred to (100)/(200) oriented grains which prefers to yield later. This is reproduced by the EPSC simulations as a kink in the elasto-plastic transition region. Similar behavior is observed in the coarse microstructure (Fig. 5.4), where the direct partitioning between γ and γ' after yielding is clearly seen for both (110)/(220) and (100)/(200) orientations.

Apart from the elastic lattice strains from the peak positions, the peak shape evolution can give information on microstructure evolution during deformation. Fig. 5.5(a,b) shows the evolution of intensity (normalized by the intensity in the unloaded state) of deconvoluted peaks in fine and coarse microstructures. The intensity of (200) increases, while (220) intensity decreases with deformation as shown in Fig. 5.5(a). The evolution of intensity of the γ' (100) and (110) peaks follows the same trends as the γ (200) and (220) peaks (Fig. 5.5(b)) and further conclusions were difficult to draw due to higher noise levels in the superlattice peaks.

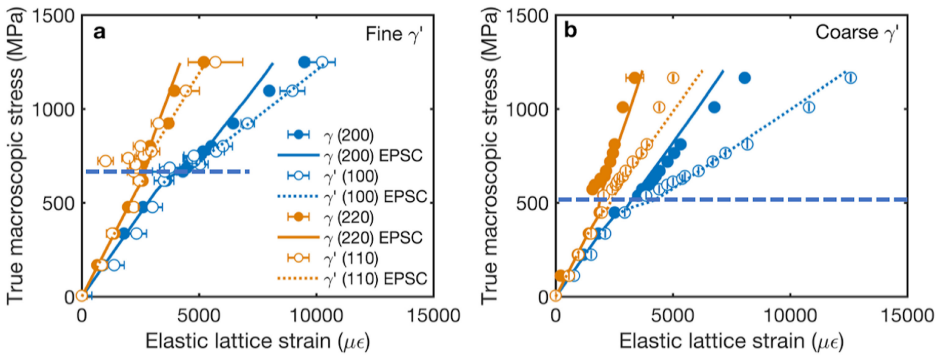

Figure 5.4: Load transfer between γ' (100)/ γ (200) and γ' (110)/ γ (220) in (a) fine and (b) coarse γ' microstructures. Markers show experimental data and lines indicate fitted EPSC model. Note that when error bars are not visible, they are smaller than the marker size.

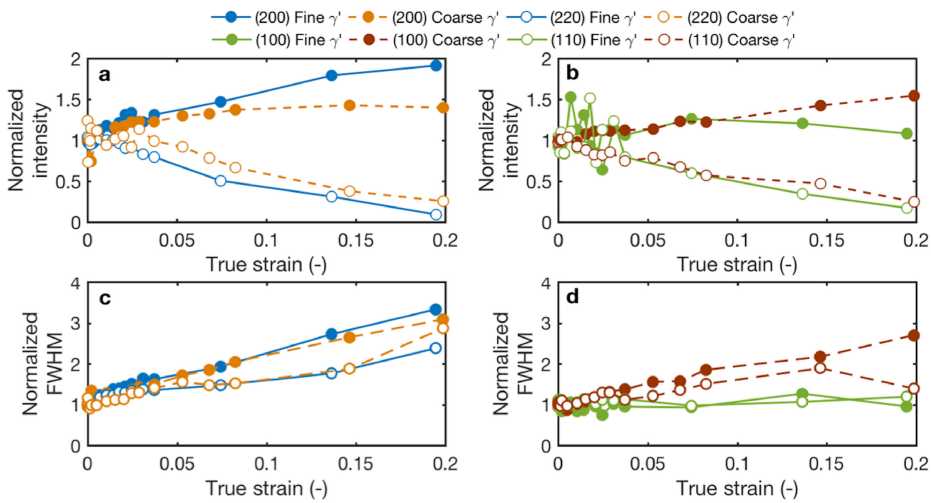

Figure 5.5: Evolution of (a) normalized peak intensity for the (200) and (220) γ peaks; (b) normalized peak intensity for the (100) and (110) γ' peaks; (c) normalized FWHM for the (200) and (220) γ peaks; and (d) normalized peak intensity for the (100) and (110) γ' peaks with deformation in the fine and coarse microstructures.

Moreover, the peak broadening which is measured as full width at half maximum (FWHM) typically indicates the quantities in the microstructure such as size of sub-μm size crystals or presence of dislocations, provided that the instrumental broadening is corrected for. In this study, no significant changes in the γ' particle size is expected to occur. Thus, any change in the peak broadening during deformation corresponds to result of an increased disloca-

tion density. Here, the FWHM of the decomposed (200) and (220) γ peaks and the (100) and (110) γ' peaks are considered and normalized in the same way as for the intensity. The evolution of FWHM with strain is shown in Fig. 5.5(c,d) for both microstructures. For the γ matrix, the normalized FWHM of both (200) and (220) increases with strain (Fig. 5.5(c)), more so in (200) compared to (220). No increase in FWHM was observed for γ' in the fine microstructure, which is probably due to prevention of significant dislocation storage within the fine γ' particles. On the other hand, the FWHM of coarse structure increases almost comparable to the matrix, despite the lower degree of plasticity suggested by the lattice strain evolution. This could due to accumulation and pile-up of dislocations around the impenetrable particles leading to inhomogeneous stress fields and spatial strain variations within and between coarse particles.

As will be shown later (section 5.1.2) there is also a possibility that the coarse γ' particles yield at higher stresses, which would also contribute to an increase in the FWHM. Similar observations were reported in high γ' volume fraction superalloys, but the γ in the coarse particle structure has larger increase in FWHM compared to fine particle size microstructure [14]. From the peak intensity evolution, both deformed microstructures showed typical fcc behavior with increasing in intensity of (200) and (111) and decreasing (220) with strain.

In addition to in-situ neutron diffraction, ex-situ microscopy investigations were performed on both deformed microstructures using ECCI and EBSD techniques in SEM, and the interaction of dislocations with fine and coarse γ' were recorded using the two-beam condition in TEM. The detailed discussion on the observations on the average deformed microstructure and texture in fine and coarse microstructures are presented in **Paper I**, but the important observations from TEM analyses are shown in Fig. 5.6(a-c) and (d-f) for fine and coarse microstructures, respectively. On the one hand, fine γ' has slip lines clearly visible in the low magnification micrograph (Fig. 5.6(a)) and at higher magnification shearing of the fine γ' particles can be seen (Fig. 5.6(b)). Also, the presence of paired dislocations are shown in Fig. 5.6(c) as described in Chapter 2 (section 2.1.2). On the other hand, the coarse microstructure shows a distinct accumulation of single dislocations around the γ' particles as a result of Orowan looping as shown in Fig. 5.6(d,e). Also, in spite of the very slow cooling (from 950 °C to 500 °C) there exists regions with fine secondary γ' particles with paired dislocations (Fig. 5.6(f)). As the small fraction of such particles is insignificant, it doesn't influence the deformation mechanism of coarse γ' microstructure.

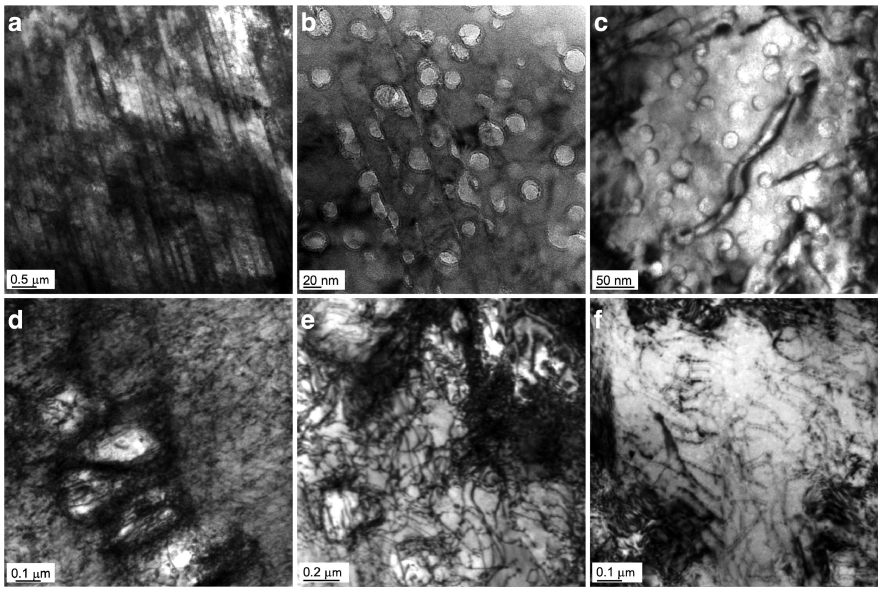

Figure 5.6: Bright field TEM micrographs of deformed microstructures with (a)–(c) fine γ', and (d)–(f) coarse γ'. (a) Slip lines; (b) Distinct shearing of precipitates; (c) Paired dislocations indicating shearing of precipitates is the predominant deformation mechanism. (d) Accumulation of dislocations in the matrix around the precipitates; (e) Single matrix dislocations and dislocation debris around γ' precipitates, indicating that precipitate shearing is not the dominating deformation mechanism; (f) Paired dislocations in regions with secondary small γ' precipitates, where particle shearing becomes active. All bright field micrographs were recorded in zone axis [110]

Thus, the description of important results from the load distribution between and within γ and γ' at room temperature have been presented. The most important conclusion is that the two microstructures do lead to different deformation mechanisms, which in turn lead to distinctly different load partitioning behavior. This allows the next step in the investigation, where the response of the two microstructures at non-ambient temperatures are explored. The next section focuses on the load distribution at cryogenic temperatures, 20 K and 100 K, in comparison with room temperature (300 K).

5.1.2 Load distribution at cryogenic temperatures

The representative fine and coarse microstructures are shown in Fig. 5.7(a,b) along with the macroscopic stress-strain curves measured at 20 K, 100 K and 300 K for two microstructures in Fig. 5.7(c,d). The change in yield stress is found to decrease linearly with temperature (Fig. 5.7(e)) for both microstructures. The difference in yield strength between samples was ∼100 MPa at all temperatures. The yield stress of fine γ' is higher than the coarse due to the strengthening associated with particle sharing. Otherwise, the ductility is consistently higher for coarse γ', and is only slightly lower at 100 K compared to 300 K, but decreases drastically at 20 K (Fig. 5.7(e)). The work hardening rates for the two microstructures are independent of temperature as shown in Fig. 5.7(f) and (g). Fine γ' shows an extended period of gradually decreasing work hardening followed by a slower decrease at higher strains, while the coarse structure shows a more abrupt change from the elasto-plastic transition region to linear region, defined as stage II work hardening and this behavior agrees well with previous observations [87].

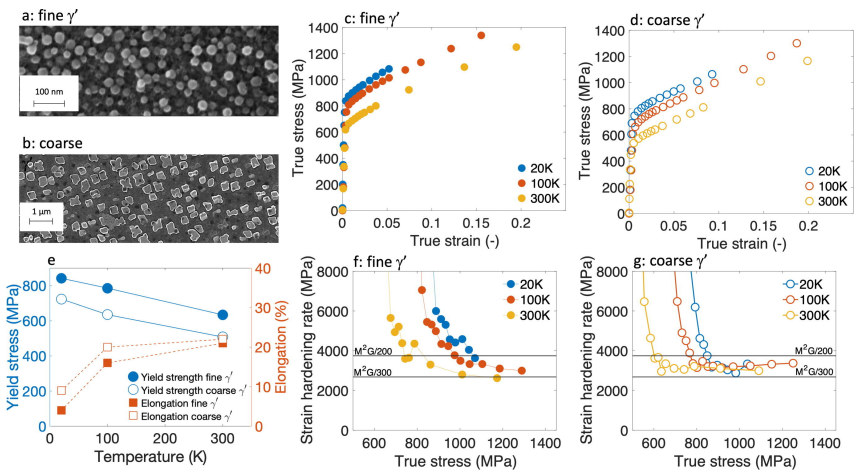

Figure 5.7: Illustration of two-unimodal microstructures of Haynes 282, (a) fine γ' and (b) coarse γ'. Global stress–strain curves measured at 20 K, 100 K and 300 K with (c) fine γ', (d) coarse γ' followed by the (e) variation of yield stress and ductility with temperatures for both microstructures. Strain hardening behavior of (f) fine γ' and (g) coarse γ' microstructures at respective temperatures.

The evolution of phase-averaged elastic lattice strains of fine and coarse γ' microstructures are shown in Fig. 5.8(a-c) and (d-f), respectively. In fine γ', co-deformation of matrix and particle phases is observed at all temperatures and the evolution is almost linear with applied stress without load distribution between the phases (Fig. 5.8(a-c)). This is consistent with the observa-

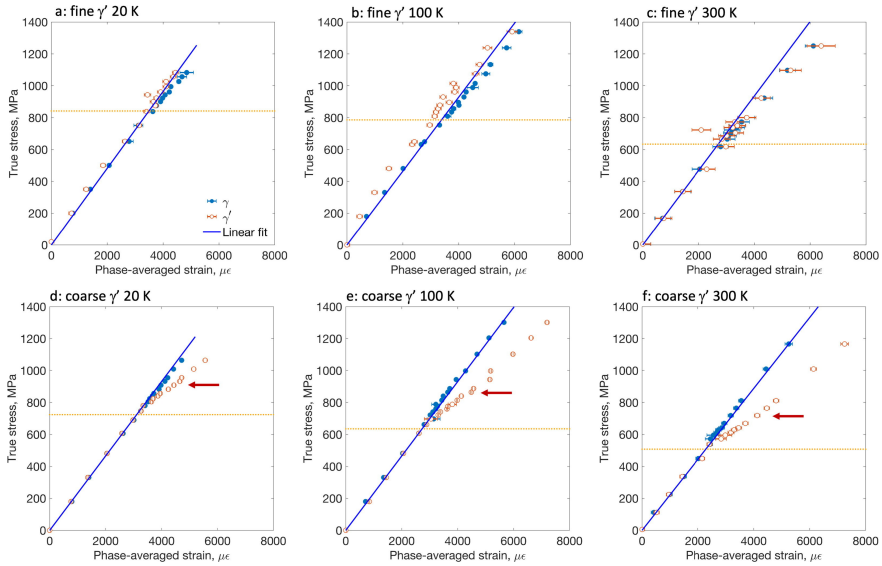

Figure 5.8: Phase-averaged lattice strains in case of (a-c) fine and (d-f) coarse γ' microstructures at (a,d) 20 K, (b,e) 100 K and (c,f) 300 K, respectively. The yellow dashed lines indicate the yield stress and the blue solid lines shows the slope of the c lattice strain evolution in the elastic region. Red arrows in (d-f) indicate approximate stress levels where a change in slope of the elastic lattice strain development can be seen

tions from **Paper I**, where the deformation of fine and coarse microstructures were conducted at room temperature. Furthermore, the coarse microstructure shows distinct load partition between γ and γ' after the yield stress at all temperatures. Similar to fine γ', the γ lattice strain increases linearly, while the γ' shows two stages of evolution with change in slope at stress levels around 200 MPa above the yield stress (marked with red arrows in Fig. 5.8(d-f)).

Further, the load partitioning between γ and γ' in coarse γ' is determined using the difference between the respective lattice strains ($\Delta\epsilon = \epsilon^{\gamma'} - \epsilon^{\gamma}$) as shown in Fig. 5.9. It is observed that the initial stage of partitioning is similar at all temperatures, but the rate decreases at higher strains. This is more pronounced at 100 K compared to 300 K. The sample at 20 K has failed too early to reliably determine the evolution of strain partitioning between the phases.

The orientation-specific lattice strains are analysed at all temperatures as shown in Fig. 5.10. During deformation, the $\langle 111 \rangle$ and $\langle 311 \rangle$ oriented grains in the γ matrix show very limited changes in slope after yielding, which is common to both microstructures. The $\langle 220 \rangle$ grains undergo early yielding (change

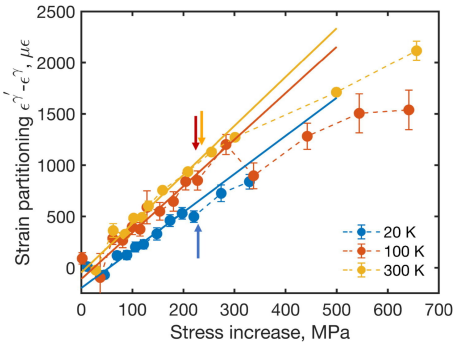

Figure 5.9: Elastic lattice strain (equivalent to load) partitioning between γ and γ' as a function of stress increase above the yield stress in the coarse microstructure. Arrows indicate the approximate positions identified in Fig. 5.8(d)-(f).

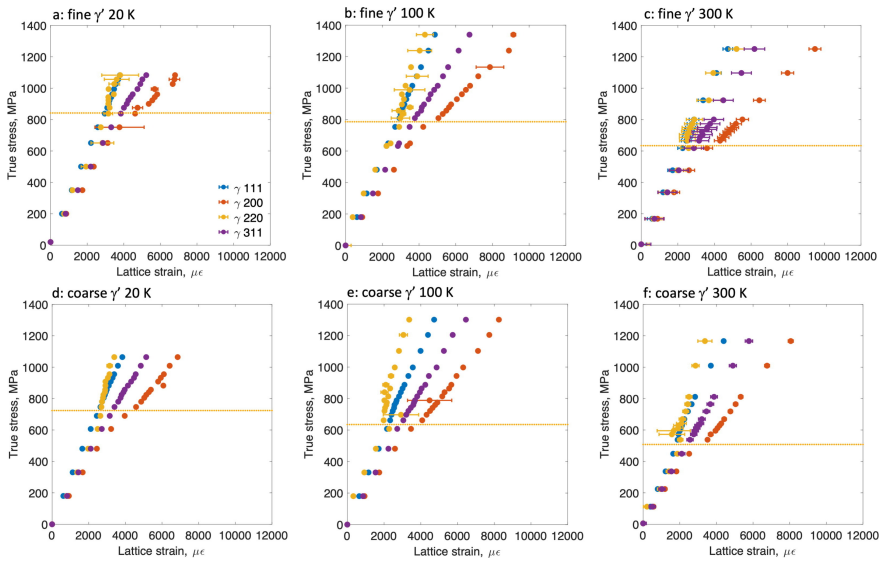

Figure 5.10: The elastic lattice strains against applied stress of the fundamental FCC peaks of (a-c) fine and (d-f) coarse γ' at (a,d) 20 K, (b,e) 100 K and (c,f) 300 K, respectively. The yellow dashed lines indicate the yield stress

in slope in Fig. 5.10), which leads to intergranular load transfer to the $\langle 200 \rangle$ orientation in the matrix. In the fine γ', the load transfer in the matrix is directly reflected in the strengthening phase, where the increased accumulation of elastic lattice strains in the $\langle 100 \rangle$ orientation is observed as shown in Fig. 5.11(a-c). Apart from yielding of the $\langle 110 \rangle$ due to lattice coherency and particle shearing, also the $\langle 210 \rangle$ and $\langle 211 \rangle$ orientations in γ' show an increase in slope after the yield stress. This suggests that the matrix grains with simi-

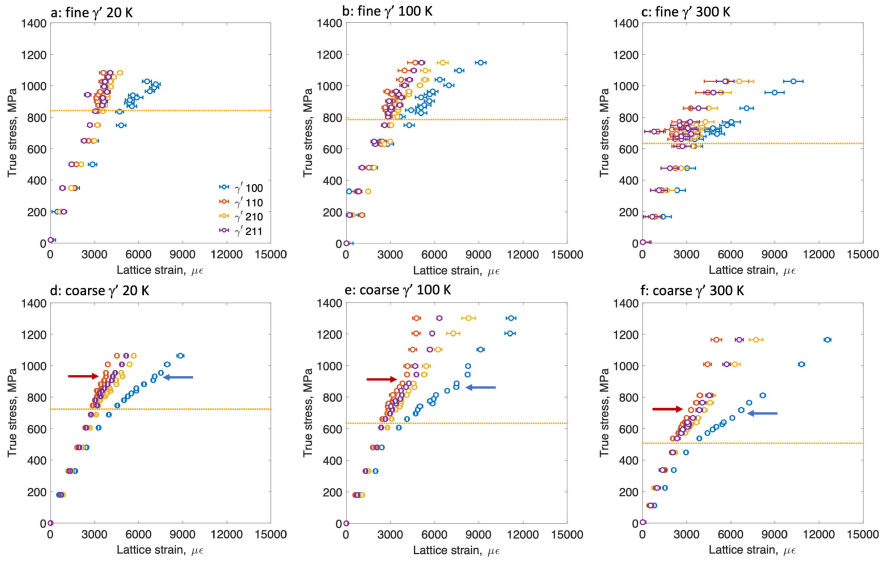

Figure 5.11: The elastic lattice strains against applied stress of the superlattice γ' peaks of (a-c) fine and (d-f) coarse γ' at (a,d) 20 K, (b,e) 100 K and (c,f) 300 K, respectively. The yellow dashed lines indicate the yield stress. Blue and red arrows in (d-f) indicate yielding of the $\langle 100 \rangle$ and $\langle 110 \rangle$ orientations, respectively.

lar orientation of γ' can also yield, however the respective γ peaks are not in the range of the measured diffractograms. In coarse γ', the $\langle 110 \rangle$ orientation shows no signs of yielding at the early stage of deformation. But the distinct change in slope observed at higher stress (red arrows) after the yield point, indicate yielding at later stage of deformation as shown in Fig. 5.11(d-f).The $\langle 100 \rangle$ orientation with higher elastic lattice strain shows the signs of yielding at higher stresses (blue arrows).

The yielding of γ and γ' orientations can be compared using the respective deconvoluted peaks $\langle 100 \rangle$, $\langle 110 \rangle$ and $\langle 200 \rangle$, $\langle 220 \rangle$ as shown in Fig. 5.12 for two microstructures. In fine γ', there is clear overlap of $\langle 100 \rangle$ and $\langle 200 \rangle$ indicating the co-deformation of matrix and particle phases. The $\langle 110 \rangle$ and $\langle 220 \rangle$ orientations also show overlap behavior and exhibit almost ideal plastic behavior after yielding followed by a linear development with smaller slope (except at 20 K due to the early fracture). In coarse γ', the load partitioning between the decomposed peaks of γ and γ' are very distinct at all temperatures. There is an intragranular load partitioning within the $\langle 200 \rangle$ and $\langle 220 \rangle$ orientations, from matrix to γ' particles. Further, the changes in the slope for the $\langle 100 \rangle$ (blue arrows) and $\langle 110 \rangle$ (red arrows) orientations, which suggests the yielding of γ' at higher stresses at all three measured temperatures. Fig. 5.13 shows the strain partitioning between $\langle 100 \rangle$–$\langle 200 \rangle$ and $\langle 110 \rangle$–$\langle 220 \rangle$, which is determined

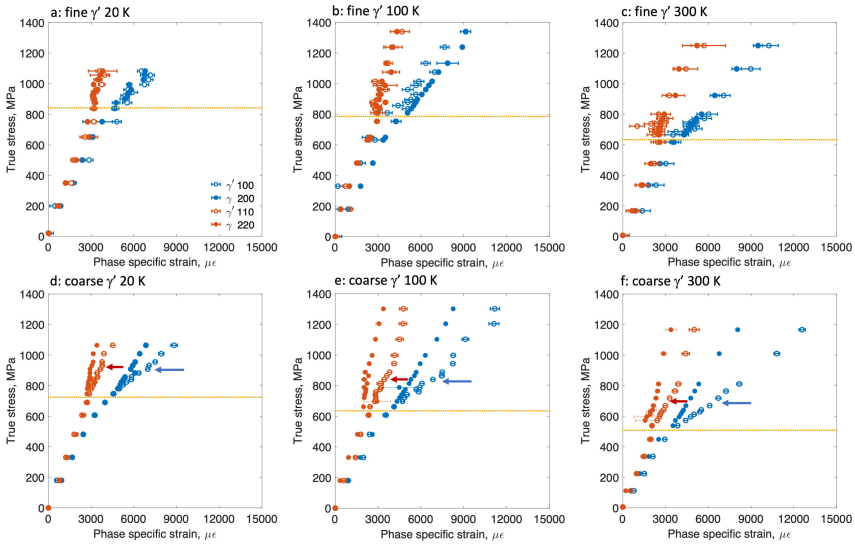

Figure 5.12: Load distribution between γ' $\langle 100 \rangle$/ γ $\langle 200 \rangle$ and γ' $\langle 110 \rangle$/ γ $\langle 220 \rangle$ in (a-c) fine and (d-f) coarse γ' microstructures at (a,d) 20 K, (b,e) 100 K and (c,f) 300 K, respectively. The yellow dashed lines indicate the yield stress. Blue and red arrows in (d-f) indicate yielding of the $\langle 100 \rangle$ and $\langle 110 \rangle$ orientations, respectively.

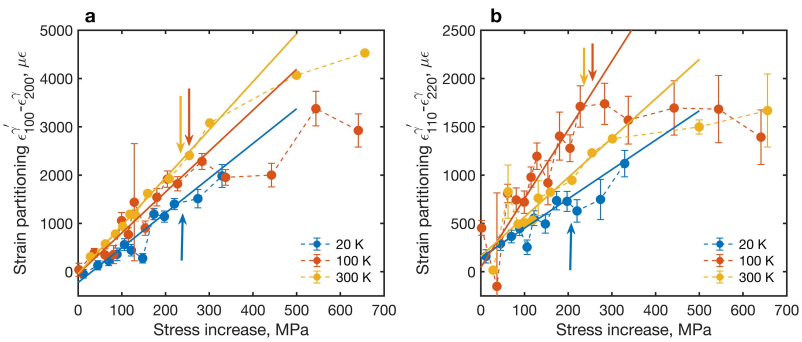

Figure 5.13: Elastic lattice strain (equivalent to load) partitioning between γ and γ' for grains with (a) $\langle 100 \rangle$/$\langle 200 \rangle$ orientation and (b) $\langle 220 \rangle$/$\langle 110 \rangle$ orientation parallel to the tensile direction, as a function of stress increase above the yield stress. Arrows mark approximate points identified in Figure 5.11(d)-(f) and Figure 5.12(d)-(f).

as $\Delta\epsilon_{hkl} = \epsilon^{\gamma'}_{hkl} - \epsilon^{\gamma}_{hkl}$. It is observed that the strain partitioning at higher stresses is dependent on the deformation temperature. The $\langle 100 \rangle$ orientation shows a more pronounced decrease in partitioning rate at 100 K compared to 300 K (Fig. 5.13(a)). The effect is even more pronounced in the $\langle 110 \rangle$ orientation, where the partitioning rate becomes almost independent of applied stress at higher stresses (Fig. 5.13(b)).

Thus, the load distribution between matrix and particle phases at cryogenic temperatures in comparison with room temperature have been studied and thoroughly discussed. The main outcome is the indications of yielding of coarse γ' at higher stresses, which become more pronounced as the stress levels increase at cryogenic temperatures. The next section deals with the load distribution during deformation in fine and coarse γ' microstructures at 650 and 730 °C, respectively.

5.1.3 Load distribution at high temperatures

The fine and coarse γ' microstructures are subjected to the in-situ tensile testing each at 650 and 730 °C, respectively. The average mechanical response in terms of load and compliance-corrected displacement is shown in Fig. 5.14(a) and (b). Both fine and coarse microstructures show decreasing stress levels with increasing temperature. All samples except fine γ' deformed at 650 °C has a peak stress followed by continuously decreasing stress levels. The apparent softening is mainly due to the occurrence of necking, which occurs in all tested samples, except in the case of fine γ' deformed at 650 °C. The dashed lines in Fig. 5.14(a) and (b) indicate the onset of necking, corresponding to the maximum in the engineering stress. In this study, there are mainly two issues in order to further consider stress values from the stress-rig; (1) No extensometer was used during the tensile tests so there is no reliable measure of the strain in the gauge volume. Also, the compliance corrected displacements are not accurate enough for the true stress calculation as the effective gauge length will change during the test due to the continuous elongation from gauge section to the shoulders. (2) Almost all samples have shown decrease in stress levels due to necking. Both necking region and the neutron gauge volume are approximately centered on the gauge length. But the stress is calculated based on the assumption of uniform deformation, which is disconnected from the elastic strain measured from the necking region. Backzmański et al. [146] suggested an approach to bypass both issues. They proposed the average true stress in the neutron gauge volume $\bar{\sigma}$, is proportional to the average elastic lattice strain measured from diffraction, $\bar{\epsilon}$:

$$\bar{\sigma} = \kappa\bar{\epsilon} \tag{5.1}$$

Here, the proportionality constant κ is determined from the elastic region and Eq. 5.1 holds both in the elastic and plastic regimes. Thus, the $\bar{\sigma}$ is considered as true stress throughout the deformation, as it is determined from the diffraction strain measurements. However, this assumption is only valid if κ does not change significantly during the tests. This hypothesis is usually far from the reality, as κ depends on the elastic stiffness and texture which changes during deformation. Backzmański et al. [146] performed EPSC and finite element (FE) simulations considering the lattice rotation, texture evolution

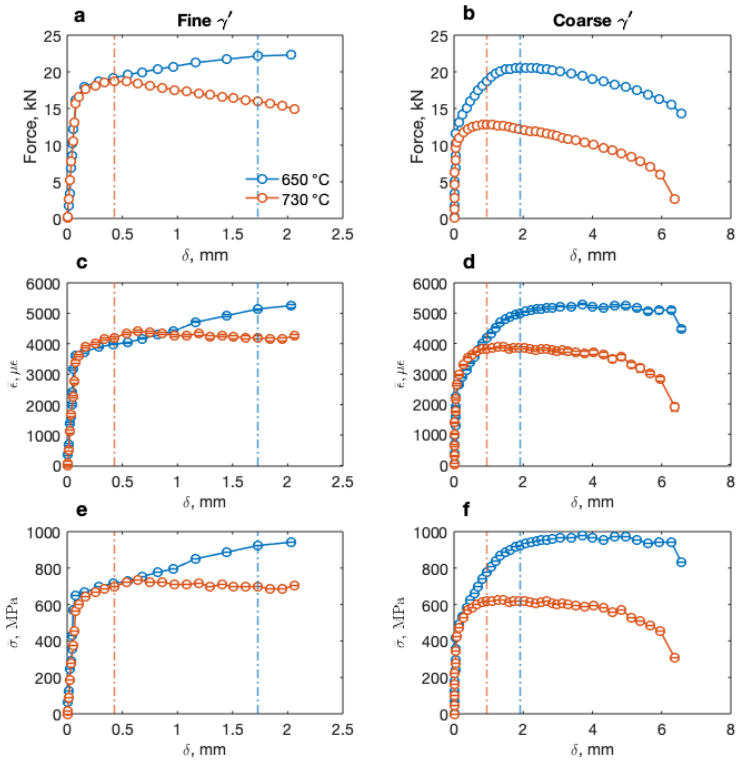

Figure 5.14: The in-situ tensile test response of fine and coarse γ' at 650 and 730 °C are presented in terms of Force vs. displacement in (a,b) and the change in phase-averaged lattice strain ($\bar{\epsilon}$) and lattice stress ($\bar{\sigma}$) with displacement are illustrated in (c,d) and (e,f) respectively. The blue and red dash lines indicates the maximum load during the tensile tests.

and verified the linear relationship holds up to large strains (>0.5) including the early stages of necking. Thus, the Eq. 5.1 is implemented in this work to calculate the true stress for all conditions. Further, the average of the phase-averaged lattice strains were determined considering the volume fraction of the γ and γ' (Eq. 5.2), similar to the approach followed by Backzmański et al. [146–148] on duplex stainless steel.

$$\bar{\epsilon} = (1 - f)\epsilon^{\gamma} + f\epsilon^{\gamma'} \tag{5.2}$$

Fig. 5.14(c,d) and (e,f) represents the evolution of $\bar{\epsilon}$ and $\bar{\sigma}$, respectively. In fine γ', both $\bar{\epsilon}$ and $\bar{\sigma}$ increases continuously at 650 °C, but reaches a maximum and decreases slightly at 730 °C. In coarse γ', both $\bar{\epsilon}$ and $\bar{\sigma}$ saturate at 650

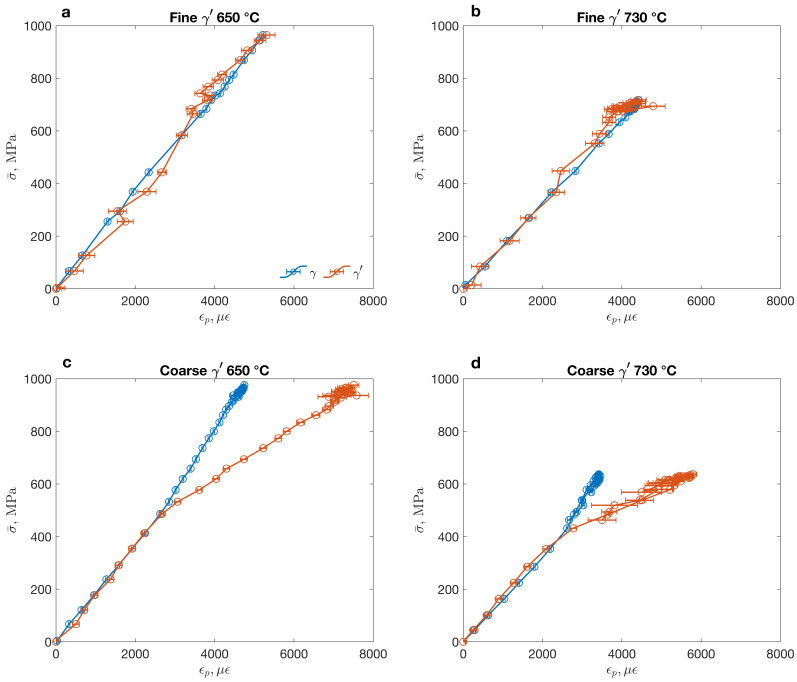

Figure 5.15: The evolution of phase-specific lattice strains at 650 and 730 °C for (a,b) fine γ' and (c,d) coarse γ' at 650 and 730 °C, respectively.

°C, but decrease in the stress after necking at 730 °C is more pronounced than fine γ'.

Further, the distribution of lattice strains between phases during deformation is shown in Fig. 5.15, where the phase-averaged lattice strains are plotted against $\bar{\sigma}$. Fine γ' shows co-deformation of γ and γ' at 650 and 730 °C, which indicates that shearing of γ' particles by paired dislocations, similar to the observations from **Paper I and II**, prevails also at higher temperatures. However, the previous studies on Haynes 282 has shown the transition in deformation mechanism from shearing to looping at 760 °C with the particle size of 50 nm [9]. But with particle size of 20 nm, the shearing seems to be dominant also at higher temperatures. Coarse γ' shows significant load transfer from γ to γ' suggesting Orowan looping of γ' particles by single dislocations, as observed at the room and cryogenic temperatures. Due to the necking, all conditions (except fine γ' at 650 °C) show a decrease in stress along the same slope as in the hardening regime.

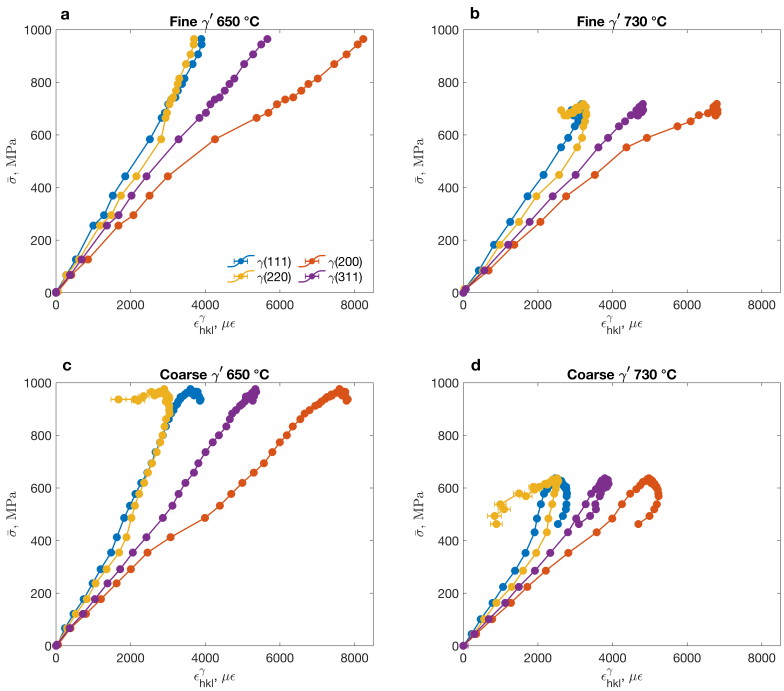

Figure 5.16: The evolution of γ orientation-specific lattice strains at 650 and 730 °C for (a,b) fine γ' and (c,d) coarse γ', respectively.

The distribution of orientation-specific lattice strains in the matrix γ phase is shown in Fig. 5.16 for both microstructures at 650 and 730 °C. The load distribution is similar to previous observations at lower temperatures until necking regime. Once necking sets in, there is an accelerated redistribution of strains from (220) orientations to other orientations. Also, the spring-back of the strain does not follow the slope of the load curve in the coarse γ' at 730 °C. The γ' orientation-specific lattice strains are shown in Fig. 5.17, where the distribution of strains are similar to the low temperature observations (**Paper I and II**) and further observations are difficult to evaluate due to larger scatter of γ' peaks in the diffractogram. Nevertheless, the load is transferred to (100) from other orientations, which is clear in the coarse microstructure (Fig. 5.17(c,d)). The yielding of (110) and further reduction in the lattice strains after necking in coarse γ' reflects the partitioning from (220) to (200) orientations in the γ matrix. At 730 °C, the detailed response of (110) is difficult to analyse due to the scatter.

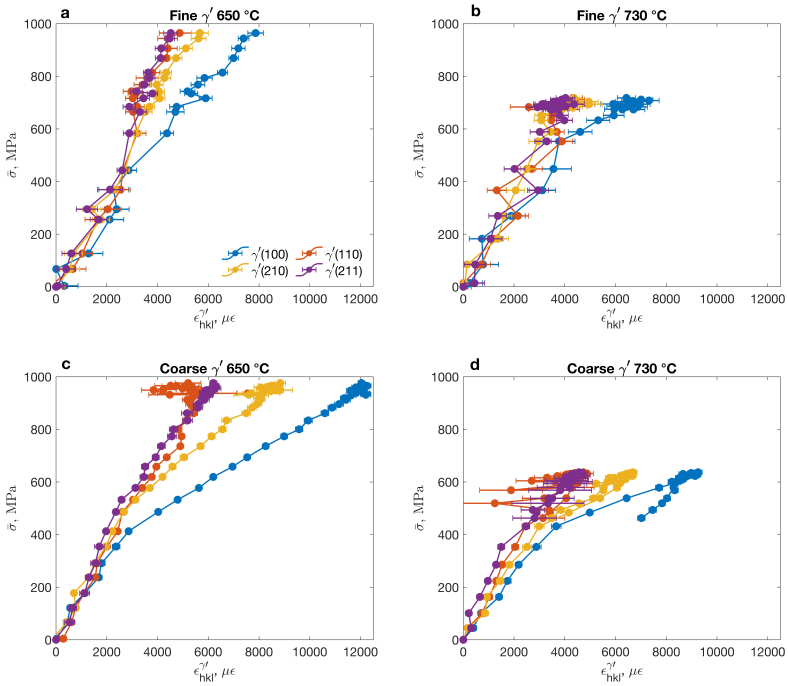

Figure 5.17: The evolution of γ' orientation-specific lattice strains at 650 and 730 °C for (a,b) fine γ' and (c,d) coarse γ', respectively.

Further, the phase-averaged (σ^p) and orientation-specific (σ^p_{hkl}) stresses in each phase are determined and plotted against the displacement to observe the load distribution between and within γ and γ' at 650 and 730 °C. In fine γ', the phase-averaged stresses of γ and γ' are identical and follow the average stress behavior as shown in Fig. 5.18(a,b). The orientation-specific stresses in the γ phase show continuous strain hardening in fine γ' at 650 °C, with highest stress in the (200) orientation and the lowest for (220) oriented grains (Fig. 5.18(c)). At 730 °C, both (200) and (311) orientations saturate at the point of necking, while (111) and (220) decrease at larger deformations (Fig. 5.18(d)). The γ' orientation-specific stress distribution shows continuous hardening at 650 °C with the highest stress in the (100) orientation (Fig. 5.18(e)), while all orientations saturate at the point of necking at 730 °C (Fig. 5.18(f)). The stress in deconvoluted (100)/(200) and (110)/(220) are found to be same, hence, the stresses are same in both phases.

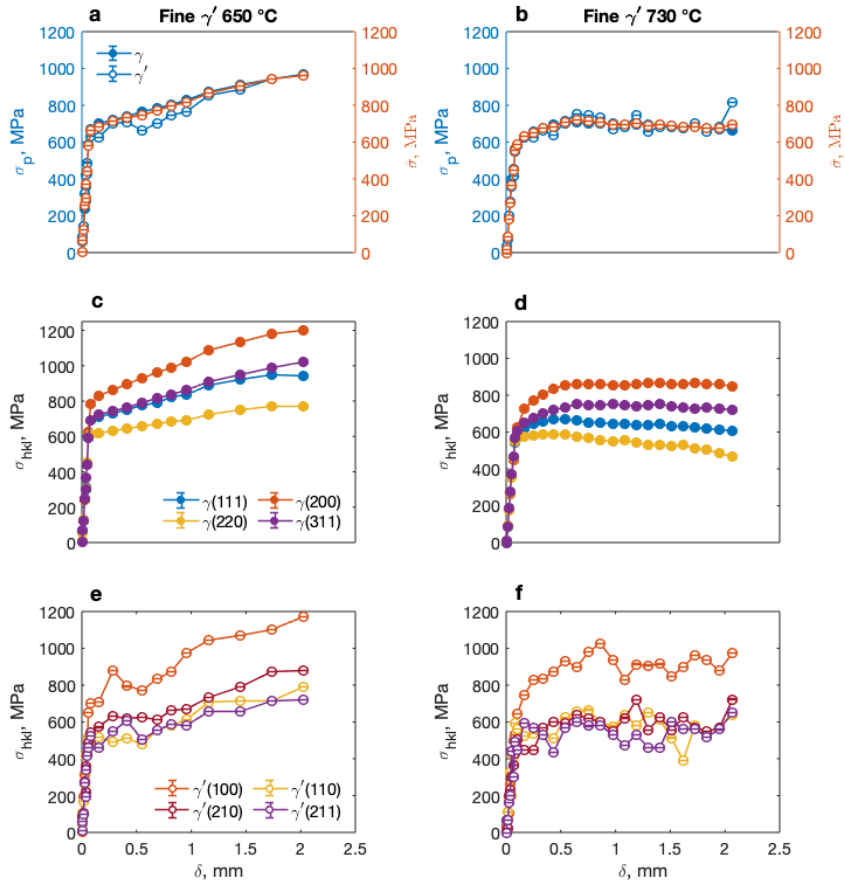

Figure 5.18: The evolution of phase-averaged and orientation specific stresses in fine γ'. (a) and (b) shows the phase-averaged stresses at 650 and (b) 730 °C, respectively. Orientation-specific stresses for the γ phase are shown in (c) and (d) for 650 and 730 °C, respectively, and the corresponding stresses in γ' are shown in (e) and (f).

The phase-averaged stresses in the coarse γ' microstructure at 650 °C and 730 °C clearly shows the load transfer from γ to γ' as shown in Fig. 5.19(a,b) with relatively more softening after necking at 730 °C compare to 650 °C. The distribution of γ orientation-specific stress at 650 °C shows the work hardening of (200) and (111) orientations, whereas (311) saturates and (220) shows decreasing stresses at large deformations (Fig. 5.19(c)). This behavior is similar but even more pronounced at 730 °C (Fig. 5.19(d)). At 650 °C, all orientations in the γ' phase appear to saturate with an exception of (110) as shown

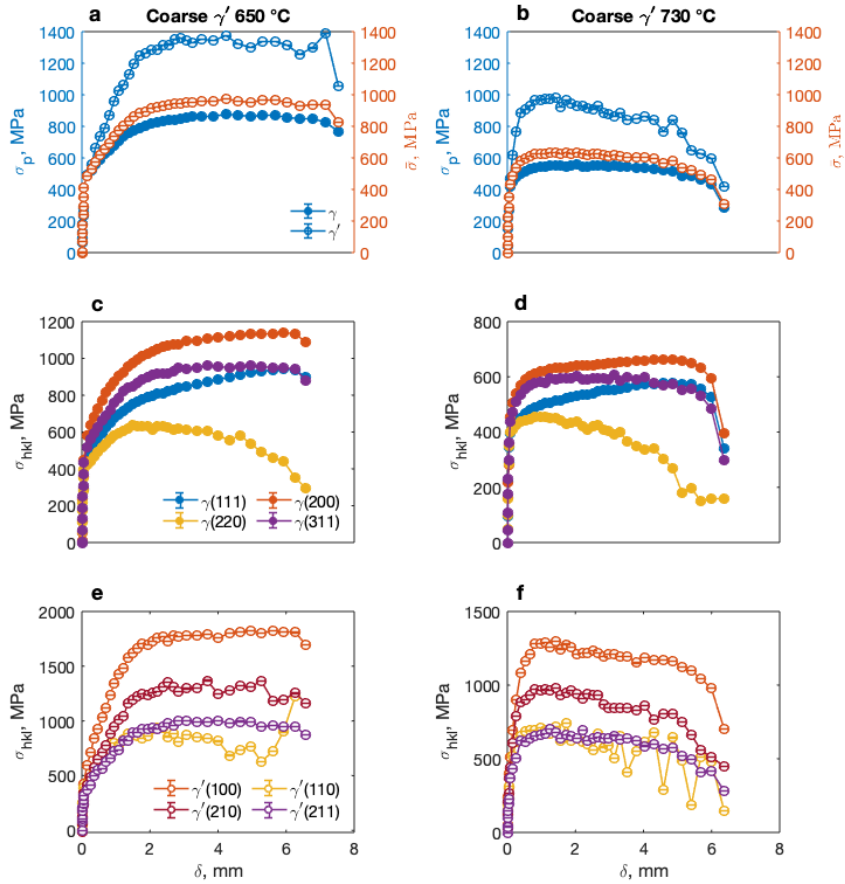

Figure 5.19: The evolution of phase-averaged and orientation specific stresses in coarse γ'. (a) and (b) shows the phase-averaged stresses at 650 and (b) 730 °C, respectively. Orientation-specific stresses for the γ phase are shown in (c) and (d) for 650 and 730 °C, respectively, and the corresponding stresses in γ' are shown in (e) and (f).

in Fig. 5.19(e). At 730 °C, all orientations soften after necking. At both temperatures, there is a stress redistribution between the (210), (110) and (211) orientations, which is not observed in fine γ'. This further indicates the effects of load transfer between matrix and particles but it is difficult to analyse since the corresponding (420) and (422) γ peaks are not available.

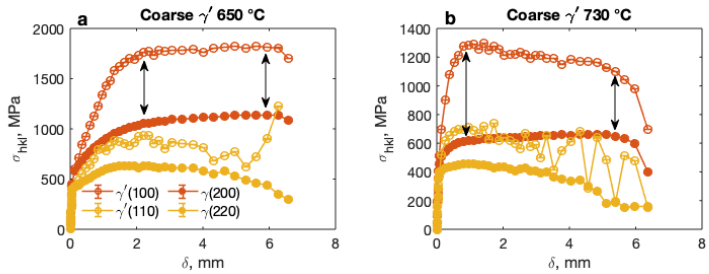

Figure 5.20: The load transfer between $\gamma'(100)/\gamma$ (200) and $\gamma'(110)/\gamma$ (220) in coarse γ' at (a) 650 and (b) 730 °C.

The comparison of the (100)/(200) and (110)/(220) shows the stress partitioning between the two phases in the coarse γ' microstructure in Fig. 5.20. At 650 °C, the stress partitioning between (100) and (200) is almost constant, while it decreases with softening of (100) at 730 °C. More observations from (110)/(220) response are difficult to draw due to the large scatter at large deformations. In summary, the observation of decreasing phase-averaged and orientation-specific stresses suggests that damage is accumulating in the material during necking. At 650 °C, fine γ' in Fig. 5.18(c) shows continuous hardening of γ matrix with lowest stress in the (220) orientation. But the saturated stresses are observed at 730 °C with softening only in the (220) orientation. Similar to γ matrix, deformation of fine γ' orientations shows hardening at 650 °C and saturation with probable softening in the (110) orientation (i.e. particles present in the (220) matrix grains). This behavior suggests that the damage accumulation is anisotropic (softening of (220) and (110) orientations). Further, coarse γ' shows distinct softening in the (220) orientation, while other orientations undergo hardening and saturate with strain at 650 °C. The softening in the (220) orientation is even more pronounced at 730 °C in the γ matrix. Also, (311) orientation seems to show decreasing in stress levels while (200), (111) tend to harden followed by collective softening at large strains. Whilst γ' shows the saturated behavior at 650 °C and very dominant softening in all orientations is clearly visible at 730 °C. This clearly suggests that the softening or damage initiation occurs in γ' particles rather than in γ as they mostly show saturated stresses (except in (220) orientation). Thus, while the actual damage mechanism is unknown at this stage, it is clearly phase-dependent and anisotropic based on the observations in this work. Identification of the exact mechanisms is critical for future efforts to improve the resistance to damage accumulation at high temperatures.

Further, the normalized intensity evolution is observed in the coarse γ' microstructure at 650 and 730 °C. It is noticed that the evolution at 650 °C depicts the typical fcc fiber texture with increase in intensity of (111) and

(100), and decreasing (110) orientations. Similar observations are noticed at 730 °C, but there is a maximum followed by decrease in strength of all fibers at larger strains probably due to development of triaxiality which could alter the local strain path in the neutron gauge volume. Such effects can be studied by EPSC simulations, which is unfortunately out of scope of this work.

5.2 Eutectic high entropy alloy - $AlCoCrFeNi_{2.1}$

$AlCoCrFeNi_{2.1}$ EHEA was prepared through vacuum induction melting of all 5 elements in high purity Ar atmosphere, and tensile samples were machined from the as-cast material. The as-cast microstructure of $AlCoCrFeNi_{2.1}$ is shown in Fig. 5.21, consisting of a lamellar structure with ordered $L1_2$ (bright contrast ∼65 vol.%) and ordered B2 phase (dark contrast ∼35 vol.%). The average chemical composition of the alloy is determined using SEM-EDS (Fig. 5.21(b,c)) and the detailed chemistry is shown in Table. 5.1, where Ni and Al are enriched in the B2 phase and Fe, Co, Cr partition to the $L1_2$ phase. In addition, the K-S orientation relationship between $L1_2$ and B2 phases is confirmed and the phase map with K-S boundaries is shown in Fig. 5.21(d,e) including the deviation histogram.

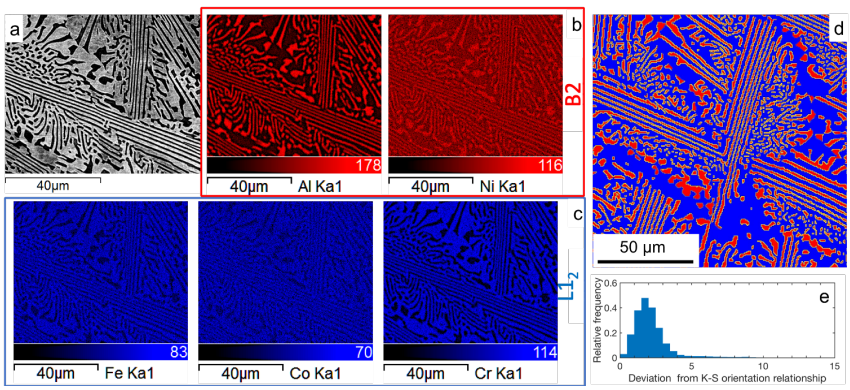

Figure 5.21: (a) Eutectic structure along with EDS maps showing the rich contrast of (b) Ni and Al to B2, and (c) Fe, Co, Cr to $L1_2$. (d) The phase map shows $L1_2$ in red and B2 in blue. The yellow lines mark phase boundaries with less than 10° deviation from the Kurdjumov-Sachs (K-S) orientation relationship, and the actual distribution of deviations from K-S is shown in (e), respectively.

The as-cast samples were measured using in-situ neutron diffraction during tensile loading from 77–973 K. These experiments were aimed to understand the load distribution between and within ordered $L1_2$ and ordered B2 phases as a function of deformation temperature. The obtained results from these

Table 5.1: Average chemical composition of EHEA and the respective phases.

Elements	Al	Co	Cr	Fe	Ni
Average, (at. %)	17.88	16.24	16.16	16.08	33.64
$L1_2$ (at. %)	10.58	18.43	20.72	19.43	30.83
B2 (at. %)	21.30	15.35	13.67	14.56	35.12

experiments were thoroughly discussed and presented in **Papers IV and V**.

5.2.1 Load distribution at 77–673 K

The macroscopic stress-strain curves measured at 77 K, 293 K and 673 K are presented in Fig. 5.22. The flow curves show distinct increase in the elastic moduli and stress levels with decreasing temperature from 673 K to 77 K.

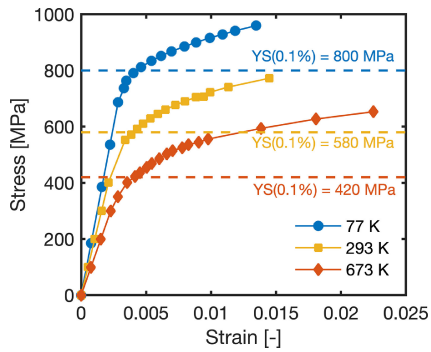

Figure 5.22: Macroscopic stress–strain curves measured at 77 K, 293 K and 673 K. Dashed lines indicate the 0.1% offset yield strengths.

The phase-averaged lattice strains against the applied stress are shown in Fig. 5.23(a-c). Please note the the phase-averaged lattice strain in the transverse direction for the B2 phase at 293 K is not calculated due to the absence of the (200) peak in the diffractograms. At 77–673 K, $L1_2$ tends to yield well before the yield stress (dashed lines) and transfer the load to B2 phase which carries larger lattice strain as shown in Fig. 5.23(a-c). Moreover, the phase-averaged stress of $L1_2$ and B2 are determined and plotted against the macroscopic strain along with the stress-strain curve in Fig. 5.23(d-f). At all three temperatures, very high stresses in the B2 phase are clearly observed, whereas $L1_2$ behaves almost perfectly plastic. Also, the average stress is calculated according to the rule-of-mixture (ROM) $\bar{\sigma} = f\sigma_{B2} + (1-f)\sigma_{L1_2}$, where volume fraction (f) is 0.35, obtained from the EBSD measurement. The macroscopic stress-

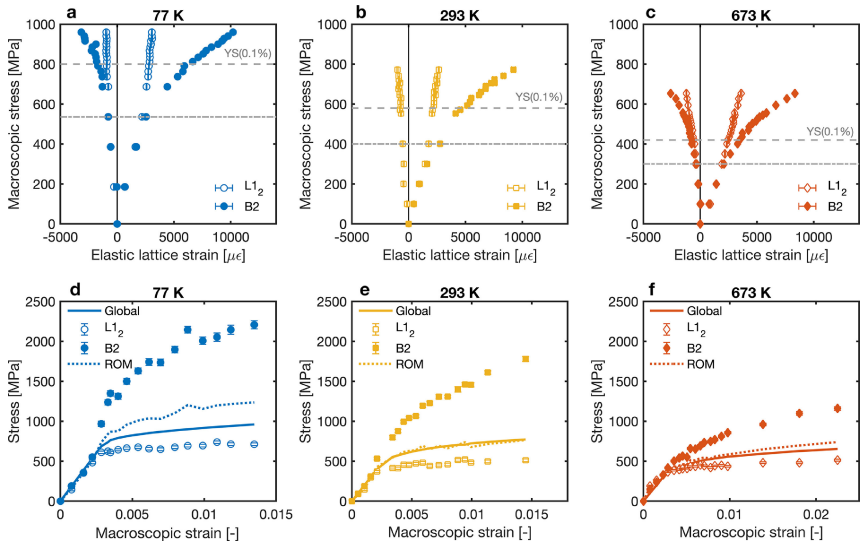

Figure 5.23: Phase-averaged lattice strain (a-c) and stress (d-f) response measured at (a,d) 77 K, (b,e) 293 K and (c,f) 673 K. Dashed lines in (a)-(c) indicate YS(0.1%), whereas dash-dotted lines indicate the data point where distinct load transfer is first observed. Dotted lines in (d)-(f) indicate average stresses calculated from the rule-of-mixtures (ROM).

strain curves agree reasonably well with the ROM stress, but it is closer to the $L1_2$ phase response at 77 K, which could be due to the continuous phase in the microstructure. But it contradicts the suggested B2 dominance from the indentation measurements as the bulk response [149]. Also, B2 phase shows decreasing stress levels with increasing temperature, whereas $L1_2$ phase stress decreases between 77 K and 293 K and remains at similar levels at 673 K.

The orientation-specific lattice strains in $L1_2$ and B2 phases are plotted against the macroscopic stress as shown in Fig. 5.24 at all temperatures. In the $L1_2$ phase, the differences in slope in the elastic regime confirms the elastic anisotropy at all temperatures. From Fig. 5.24(a,b), the (220) orientation tends to yield earlier followed by (111) while (311) is linear and (200) continuous to accumulates higher elastic lattice strains at 77 K and 293 K. At 673 K, the (111) orientation yields earlier than (200), and furthermore, the (200) and (311) orientations are deviating more towards the larger lattice strains (Fig. 5.24(c)) compared to at lower temperatures. The distribution of lattice strains of $L1_2$ phase at 77 K and 293 K are consistent with $\langle 110 \rangle \{111\}$ octahedral slip, but the early yielding of the (111) orientation at 673 K could be due to occurrence of slip on the $\{001\}$ cube slip planes. The cube slip $\langle 110 \rangle \{111\}$ is well known to operate in $L1_2$ single crystals above a critical temperature, in particular when loaded along the $\langle 111 \rangle$ direction [96–99]. Fur-

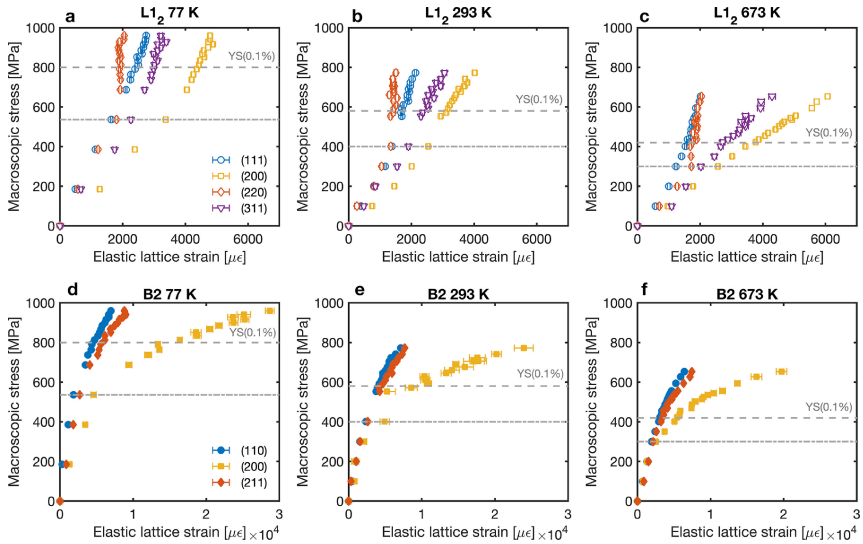

Figure 5.24: Elastic lattice strains from fundamental peaks for $L1_2$ (a-c) and B2 (d-f) at 77 K (a,d), 293 K (b,e) and 673 K (c,f), respectively. Dashed lines indicate YS(0.1%), whereas dash-dotted lines indicate the data point where distinct load transfer is first observed.

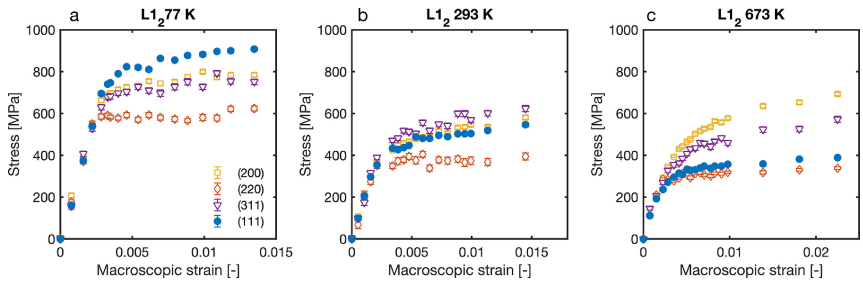

Figure 5.25: Orientation-specific stress in different $L1_2$ grain families as a function of macroscopic strain.

ther, the orientation-specific axial stress evolution is determined in $L1_2$ phase at all temperatures as shown in Fig. 5.25.

In addition, Schmid factors along four tensile directions on the octahedral and cube planes are determined as shown in the Table. 5.2. From Fig. 5.25(a) at 77 K, the (111) orientation stress is highest (due to the high stiffness and low Schmid factor for octahedral slip from Table. 5.2) and (220) orientations has the lowest due to the plastic behavior, while (200) and (311) show intermediate stress levels. At room temperature, the stress levels of (111) are almost similar to the (200) and (311), which indicates the activation of cube slip already at

Table 5.2: Maximum Schmid factors on $\langle 110 \rangle \{001\}$ cube ($m_{\max}^{\text{cube}}$) and $\langle 110 \rangle \{111\}$ octahedral ($m_{\max}^{\text{oct}}$) slip systems in grain families with different tensile axes. $N_{\max}^{\text{cube}}$ and $N_{\max}^{\text{oct}}$ are the number of independent system experiencing the maximum Schmid factor for cube and octahedral slip, respectively.

Tensile axis	$m_{\max}^{\text{cube}}$	$N_{\max}^{\text{cube}}$	$m_{\max}^{\text{oct}}$	$N_{\max}^{\text{oct}}$	$m_{\max}^{\text{cube}}/m_{\max}^{\text{oct}}$
(111)	0.4714	3	0.2722	6	1.73
(200)	0	–	0.4082	8	0
(220)	0.3536	4	0.4082	4	0.86
(311)	0.3857	1	0.4454	2	0.86

the room temperature. The critical temperature for cube slip to occur depends on the alloy chemistry and many systems have been reported to undergo cube slip at room temperature [99, 150] or even below [150], when deformed in the $\langle 111 \rangle$ direction. At 673 K, the extensive activation of cube slip leads to low stresses in the (111) grains. Lower stresses are observed in the (311) grains as well, which suggests cube slip in these grains. The (200) orientation seems to be unaffected as the Schmid factor for cube slip is zero (Table. 5.2). This slip transition from octahedral to cube slip potentially reverses the anomalous temperature dependence of the strength of the $L1_2$. This observation of cube slip in the EHEA could point towards an alloy design strategy for delaying this transition in order to further increasing the strength at elevated temperatures.

In contrast to $L1_2$, B2 phase elastic lattice strains shows approximately isotropic behavior in the elastic regime (Fig. 5.24(d-f)). Moreover, the load redistribution in B2 phase is similar at all temperatures. The lattice strain evolution of (110) and (211) orientations follow each other closely, with only small deviations towards the larger strains, whereas (200) orientation accommodates the large elastic lattice strains and carries majority of the load compare to the other two orientations in B2 phase.

Thus, the change in load distribution in the EHEA from 77–673 K has been thoroughly discussed. The most important finding is the temperature dependent slip mode transition in $L1_2$, which can be expected to have a significant impact on the behavior at higher temperature. This is discussed in the next section, which deals with the load distribution in the EHEA at 973 K.

5.2.2 Load distribution at 973 K

Fig. 5.26(a) shows the engineering stress-strain curve from the stress-rig measured during the deformation at 973 K. The yield stress is measured to be 216 MPa, which is much lower than reported values (550 MPa) at the same temperature [35]. This low yield stress is probably due to very low strain rate

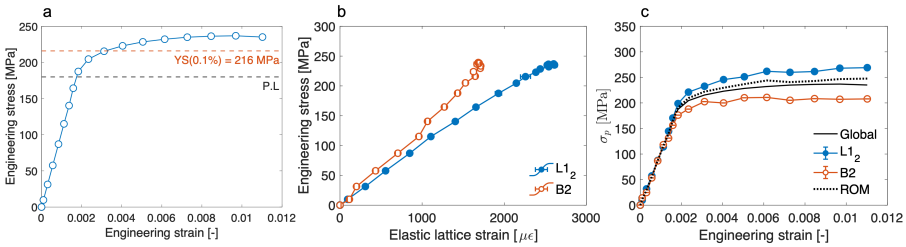

Figure 5.26: (a) The engineering stress-strain curve at 973 K with yield stress of 216 MPa and the evolution of (b) phase-averaged lattice strain and (c) phase-averaged stress, including global and ROM stress.

deformation (10^{-6} s^{-1}) which could enable creep-like deformation at lower stresses. However, the previous stress-rig measurement at 77–673 K were consistent with literature values and we believe the yield stress in this work is correct in the present deformation conditions. Further, the phase-average elastic lattice strains shows the load transfer from B2 to $L1_2$ in Fig. 5.26(b), which is contrary to the previous observations in the temperature range 77–673 K. This is further confirmed by the phase-averaged stress with higher $L1_2$ stress than B2 in Fig. 5.26(c). Thus, under the low strain rate deformation conditions, the load transfer is reversed at higher temperature making $L1_2$ the stronger phase instead of B2. Also, $L1_2$ shows work hardening at larger strains, although at a low rate, while B2 has almost ideal plastic deformation.

The distribution of orientation-specific lattice strains and stresses of $L1_2$ and B2 phases are shown in Fig. 5.27(a,b). In the $L1_2$ phase, early yielding of (111) orientation is observed, similar to the observations at 673 K (**Paper IV**). This strongly indicates the occurrence of cube slip. The continuation of cube slip from 673 K is further confirmed by phase-averaged stress, where the (111) stress levels are below the stress associated in the (220) orientations. Further, the work hardening in the $L1_2$ (Fig. 5.26(c)) is due to hardening of (200) and (311) orientations, whereas flow stress remains constant in the (111) and (220) orientations. In the B2 phase, the orientation-specific lattice strains are significantly different compared to the previous studies at lower temperature. There is a strain transfer from (110) and (211) to (200) orientation as shown in Fig. 5.27(b,d) but the orientation-specific stress shows no appreciable load redistribution between orientations (Fig. 5.27(f)). These changes in the load redistribution at different temperatures needs to be investigated further to address the temperature dependence of deformation mechanisms in the B2 phase.

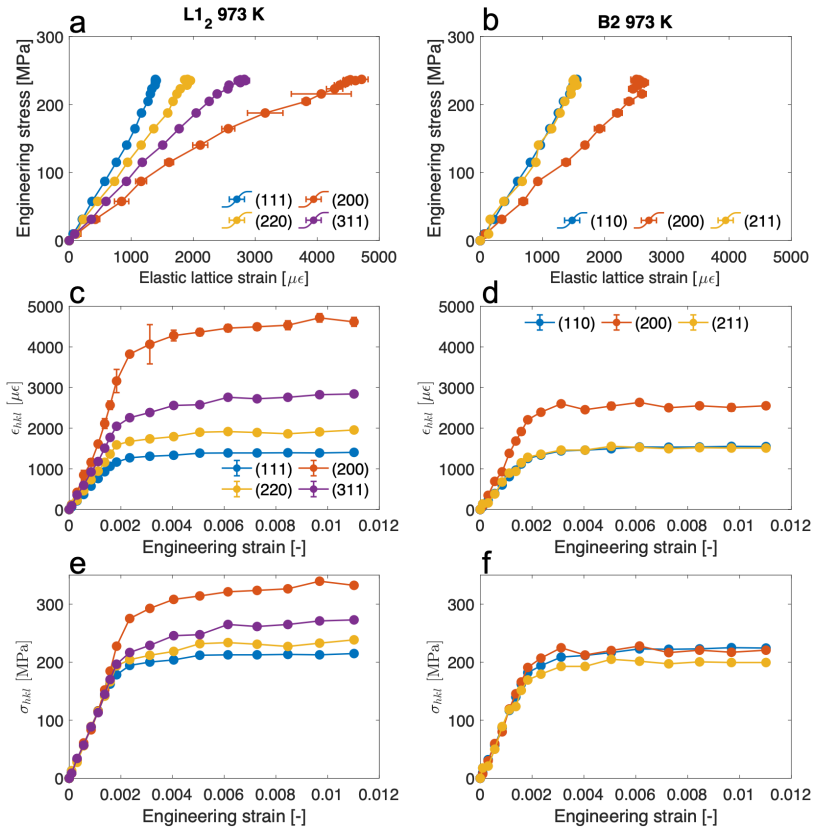

Figure 5.27: The evolution of orientation-specific lattice strains of (a,c) $L1_2$ and (b,d) B2, respectively. The orientation-specific stresses of (e) $L1_2$ and (f) B2.

Zhang et al. [35] reported the extensive twinning in the $L1_2$ phase during deformation of $AlCoCrFeNi_{2.1}$ at 700 °C. We inspected the propensity of twinning through the stacking fault probability (SFP) evolution as shown in Fig. 5.28. SFP can be evaluated from the difference in lattice strain evolution measured from the (111) and (222) peaks [151]. A small increase in SFP is noticed above the yield stress, which could indicate the presence of twinning in the $L1_2$ phase but it is not expected to be extensive at the small strains in this work. In general, the (111) orientation is prone to twinning since the Schmid factor for $\langle 112 \rangle \{111\}$ twinning is slightly higher for $\langle 011 \rangle \{111\}$ octahedral slip. However, the Schmid factor for $\langle 011 \rangle \{001\}$ cube slip is 1.5 times higher than that for twinning when loaded along (111), suggesting that such grains will undergo cube slip rather that twinning. Thus, a certain amount of twinning cannot be ruled out but the dominating effects at the small strains presented in the study arise from the $\langle 011 \rangle \{001\}$ cube slip.

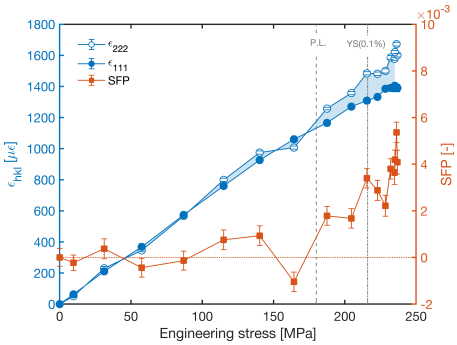

Figure 5.28: Lattice strain evolution for the (111) and (222) peaks (left axis) and the resulting stacking fault probability (right axis) as function of engineering stress. The lines marked P.L. and YS(0.1%) mark the proportionality limit and the 0.1 % proof stress, respectively (see Fig. 5.26(a))

This study has provided several new insights into the origins of the high temperature behaviour of the high entropy alloy, including the fact that the fundamental role of the phases becomes reversed. As $L1_2$ becomes the stronger phase at these temperatures, the alloying strategy proposed in **Paper IV** becomes even more interesting. Clearly, also the behavior of the B2 phase warrants further investigations, in order to improve its properties at higher temperatures.

5.3 Conclusions

The main conclusions from this work are formulated as answers to the research questions posed in Chapter 1.

1. What is the effect of particle size on the load distribution in a representative low γ' superalloys (such as Haynes 282)?

- Fine particles leads to the shearing which leads to absence of load redistribution; Coarse particle leads to the Orowan looping which leads to the distinct load redistribution. These behaviours are found to be consistent at all temperatures investigated in this work.
- The observed load distribution are same at all temperatures, which suggests that deformation mechanisms do not change with temperature.

2. What is the effect of deformation temperature on the load distribution in a representative low γ' superalloys (such as Haynes 282)?

- At higher stresses, also coarse γ' can undergo plastic deformation. This is more pronounced at low temperatures, since the stress levels increase.
- At high temperatures, the decrease in orientation and phase-specific stress levels suggests accumulation of damage in the necked region. While the damage process is unknown it is clearly anisotropic and phase-dependent.

3. What is the effect of deformation temperature on phase-specific deformation and load partitioning in as-cast EHEA $AlCoCrFeNi_{2.1}$?

- At low to intermediate temperatures (77–673 K), B2 is the reinforcing phase, but this is reversed at higher temperature (973 K).
- A slip mode transition in the $L1_2$ phase is suggested to occur around room temperature, which could be a potential alloy design strategy to sustain the high temperature strength, particularly as $L1_2$ becomes the reinforcing phase at high temperature.
- A distinct change in load redistribution in the B2 phase at high temperature (973 K) suggests a potential change in deformation mechanism.

5.4 Outlook

Based on the observations from the in-situ neutron diffraction studies on Haynes 282 and $AlCoCrFeNi_{2.1}$, a number of open questions and future directions emerge. The most important issues to be addressed, both in the short and long term perspective, are listed below.

In Haynes 282, the proposed yielding of γ' at higher stresses was inferred from lattice strain evolution needs to be confirmed using dedicated TEM studies. Due to slow rate of deformation, cross slip and climb can dominate the deformation mechanism at higher temperatures. Thus, the rate dependence effect on the load distribution needs to be determined. The damage mechanisms at higher temperature must be determined using EPSC models coupled with TEM studies. Provided that the proposed mechanisms can be confirmed, development of e.g. EPSC or FE based crystal plasticity based models capable of describing these phenomena should be developed.

In the $AlCoCrFeNi_{2.1}$ EHEA, the active slip system and it's temperature dependence in B2 phase needs to be determined using TEM analysis. Moreover, the strain rate effects on the deformation mechanisms and their effect on load partitioning needs to be determined. This will allow EPSC models to be implemented, which account for the temperature dependent slip mode transition of active slip systems in the EHEA. With the implementation of such models, the effects of orientation relationships should be explored, particularly in relation to the changing slip modes. In the long run, the proposed alloy strategy should be explored.

BIBLIOGRAPHY

[1] AMY Razak. *Industrial gas turbines: performance and operability*. Elsevier, 2007.

[2] David Furrer and Hans Fecht. Ni-based superalloys for turbine discs. *Jom*, 51(1):14–17, 1999.

[3] I Okada, T Torigoe, K Takahashi, and D Izutsu. Development of Ni base superalloy for industrial gas turbine. In *Proceedings of the Tenth International Symposium on Superalloys*, pages 707–712, 2004.

[4] W.D. Callister and D.G. Rethwisch. *Callister's Materials Science and Engineering*. Wiley, 2020.

[5] Yoshinao Mishima, Shouichi Ochiai, Noboru Hamao, Masayoshi Yodogawa, and Tomoo Suzuki. Solid solution hardening of nickel—role of transition metal and B-subgroup solutes—. *Transactions of the Japan institute of metals*, 27(9):656–664, 1986.

[6] A. J. Goodfellow. Strengthening mechanisms in polycrystalline nickel-based superalloys, oct 2018.

[7] Roger C. Reed. 2 The physical metallurgy of nickel and its alloys. *Superalloys- Fundementals and Applications*, pages 33–120, 2006.

[8] Benedict M.B. Grant, Elisabeth M. Francis, Joao Quinta da Fonseca, Mark R. Daymond, and Michael Preuss. Deformation behaviour of an advanced nickel-based superalloy studied by neutron diffraction and electron microscopy. *Acta Materialia*, 60(19):6829–6841, nov 2012.

[9] P. Zhang, Y. Yuan, H. Yin, Y. Gu, J. Wang, M. Yang, G. Yang, and X. Song. Tensile Properties and Deformation Mechanisms of Haynes 282 at Various Temperatures. *Metallurgical and Materials Transactions A: Physical Metallurgy and Materials Science*, 49(5):1571–1578, feb 2018.

[10] Zhihong Zhong, Yuefeng Gu, Yong Yuan, and Zhan Shi. Tensile Properties and Deformation Characteristics of a Ni-Fe-Base Superalloy for Steam Boiler Applications. *Metallurgical and Materials Transactions A: Physical Metallurgy and Materials Science*, 45(1):343–350, 2014.

[11] M Preuss, João Quinta da Fonseca, B Grant, E Knoche, R Moat, M Daymond, R C Reed, K A Green, P Caron, T P Gabb, M G Fahrmann, and E S Huron. The effect of γ' particle size on the deformation mechanism in an advanced polycrystalline nickel-base superalloy. In *11th International Symposium on Superalloys*, pages 405–414, United States, 2008. Minerals, Metals & Materials Society.

[12] M. R. Daymond, M. Preuss, and B. Clausen. Evidence of variation in slip mode in a polycrystalline nickel-base superalloy with change in temperature from neutron diffraction strain measurements. *Acta Materialia*, 55(9):3089–3102, may 2007.

[13] James Coakley and David Dye. Lattice strain evolution in a high volume fraction polycrystal nickel superalloy. *Scripta Materialia*, 67:435–438, sep 2012.

[14] E. M. Francis, B. M B Grant, J. Quinta Da Fonseca, P. J. Phillips, M. J. Mills, M. R. Daymond, and M. Preuss. High-temperature deformation mechanisms in a polycrystalline nickel-base superalloy studied by neutron diffraction and electron microscopy. *Acta Materialia*, 74:18–29, 2014.

[15] CJ Boehlert and SC Longanbach. A comparison of the microstructure and creep behavior of cold rolled HAYNES® 230 alloy™ and HAYNES® 282 alloy™. *Materials Science and Engineering: A*, 528(15):4888–4898, 2011.

[16] L.M. Pike. Development of a fabricable gamma-prime (γ') strengthened superalloy. *Superalloys 2008 (Eleventh International Symposium)*, pages 191–200, 2008.

[17] Bhagevatula Satyanarayana Murty, Jien-Wei Yeh, Srinivasa Ranganathan, and PP Bhattacharjee. *High-entropy alloys*. Elsevier, 2019.

[18] B. Cantor, I. T H Chang, P. Knight, and A. J B Vincent. Microstructural development in equiatomic multicomponent alloys. *Materials Science and Engineering A*, 375-377(1-2 SPEC. ISS.):213–218, 2004.

[19] Jien Wei Yeh, Swe Kai Chen, Su Jien Lin, Jon Yiew Gan, Tsung Shune Chin, Tao Tsung Shun, Chun Huei Tsau, and Shou Yi Chang. Nanostructured high-entropy alloys with multiple principal elements: Novel alloy design concepts and outcomes. *Advanced Engineering Materials*, 6(5):299–303+274, 2004.

[20] Fangjun Wang, Yong Zhang, Guoliang Chen, and Hywel A Davies. Tensile and compressive mechanical behavior of a $CoCrCuFeNiAl_0.5$ high entropy alloy. *International Journal of Modern Physics B*, 23(06n07):1254–1259, 2009.

[21] Frederik Otto, A Dlouhỳ, Ch Somsen, Hongbin Bei, G Eggeler, and Easo P George. The influences of temperature and microstructure on the tensile properties of a CoCrFeMnNi high-entropy alloy. *Acta Materialia*, 61(15):5743–5755, 2013.

[22] ON Senkov, GB Wilks, DB Miracle, CP Chuang, and PK Liaw. Refractory high-entropy alloys. *Intermetallics*, 18(9):1758–1765, 2010.

[23] S Ranganathan. Alloyed pleasures: multimetallic cocktails. *Current science*, 85(10):1404–1406, 2003.

[24] YJ Zhou, Y Zhang, YL Wang, and GL Chen. Solid solution alloys of $AlCoCrFeNiTi_x$ with excellent room-temperature mechanical properties. *Applied physics letters*, 90(18):181904, 2007.

[25] Yong Zhang, Ting Ting Zuo, Zhi Tang, Michael C Gao, Karin A Dahmen, Peter K Liaw, and Zhao Ping Lu. Microstructures and properties of high-entropy alloys. *Progress in materials science*, 61:1–93, 2014.

[26] Yiping Lu, Yong Dong, Hui Jiang, Zhijun Wang, Zhiqiang Cao, Sheng Guo, Tongmin Wang, Tingju Li, and Peter K. Liaw. Promising properties and future trend of eutectic high entropy alloys. *Scripta Materialia*, 187:202–209, oct 2020.

[27] Martin Eden Glicksman. *Principles of solidification: an introduction to modern casting and crystal growth concepts*. Springer Science & Business Media, 2010.

[28] Yiping Lu, Yong Dong, Sheng Guo, Li Jiang, Huijun Kang, Tongmin Wang, Bin Wen, Zhijun Wang, Jinchuan Jie, Zhiqiang Cao, Haihui Ruan, and Tingju Li. A promising new class of high-temperature alloys: Eutectic high-entropy alloys. *Scientific Reports*, 4(1):6200, may 2014.

[29] Qiannan Wang, Yiping Lu, Qian Yu, and Ze Zhang. The Exceptional Strong Face-centered Cubic Phase and Semi-coherent Phase Boundary in a Eutectic Dual-phase High Entropy Alloy AlCoCrFeNi. *Scientific Reports*, 8(1):14910, 2018.

[30] Adrianna Lozinko, Oleg V. Mishin, Tianbo Yu, Uta Klement, Sheng Guo, and Yubin Zhang. Quantification of microstructure in a eutectic high entropy alloy AlCoCrFeNi2.1. *IOP Conference Series: Materials Science and Engineering*, 580:012039, dec 2019.

[31] Adrianna Lozinko, Yubin Zhang, Oleg V. Mishin, Uta Klement, and Sheng Guo. Microstructural characterization of eutectic and near-eutectic AlCoCrFeNi high-entropy alloys. *Journal of Alloys and Compounds*, 822:153558, may 2020.

[32] Deep Choudhuri, Srivilliputhur G. Srinivasan, and Rajiv S. Mishra. Deformation of lamellar FCC-B2 nanostructures containing Kurdjumov-Sachs interfaces: Relation between interfacial structure and plasticity. *International Journal of Plasticity*, 125:191–209, feb 2020.

[33] Olav Hellwig, Katharina Theis-Bröhl, Guido Wilhelmi, Hartmut Zabel, and Andreas Stierle. Temperature and thickness dependent epitaxial relationship of Pd (111) on Cr (110). *Thin solid films*, 318(1-2):201–203, 1998.

[34] Saideep Muskeri, Vahid Hasannaeimi, Riyadh Salloom, Maryam Sadeghilaridjani, and Sundeep Mukherjee. Small-scale mechanical behavior of a eutectic high entropy alloy. *Scientific reports*, 10(1):1–12, 2020.

[35] Yaoli Zhang, Jinguo Li, Xinguang Wang, Yiping Lu, Yizhou Zhou, and Xiaofeng Sun. The interaction and migration of deformation twin in an eutectic high-entropy alloy AlCoCrFeNi 2.1. *Journal of Materials Science and Technology*, 35(5):902–906, 2019.

[36] Tilak Bhattacharjee, Ruixiao Zheng, Yan Chong, Saad Sheikh, Sheng Guo, Ian Thomas Clark, Toshiro Okawa, Irfan Samad Wani, Pinaki Prasad Bhattacharjee, Akinobu Shibata, and Nobuhiro Tsuji. Effect of low temperature on tensile properties of AlCoCrFeNi2.1 eutectic high entropy alloy. *Materials Chemistry and Physics*, 210:207–212, may 2018.

[37] A. Patel, I. Wani, S.R. Reddy, S. Narayanaswamy, A. Lozinko, R. Saha, S. Guo, and P.P. Bhattacharjee. Strain-path controlled microstructure, texture and hardness evolution in cryo-deformed AlCoCrFeNi 2.1 eutectic high entropy alloy. *Intermetallics*, 97:12–21, jun 2018.

[38] M. F. Ashby. A first report on deformation-mechanism maps. *Acta Metallurgica*, 20(7):887–897, Jul 1972.

[39] Terence G. Langdon and Farghalli A. Mohamed. A simple method of constructing an Ashby-type deformation mechanism map. *Journal of Materials Science*, 13(6):1282–1290, Jun 1978.

[40] David J Hull, Derek and Bacon. *Introduction to dislocations*. Butterworth-Heinemann, 2001.

[41] B Décamps, P Caron, M Condat, and T Khan. Dissociated matrix dislocations in a omicron/omicron'Ni-based single crystal superalloy. *Scripta metallurgica*, 18(10):1171–1174, 1984.

[42] Brigitte Décamps, Allan J Morton, and Marc Condat. On the mechanism of shear of γ' precipitates by single $(a/2)\langle 110\rangle$ dissociated matrix dislocations in Ni-based superalloys. *Philosophical Magazine A*, 64(3):641–668, 1991.

[43] Mustafa Benyoucef, Brigitte Décamps, Armand Coujou, and Nicole Clément. Stacking-fault energy at room temperature of the γ matrix of the MC2 Ni-based superalloy. *Philosophical Magazine A*, 71(4):907–923, 1995.

[44] F Pettinari, J Douin, G Saada, P Caron, A Coujou, and N Clement. Stacking fault energy in short-range ordered γ-phases of Ni-based superalloys. *Materials Science and Engineering: A*, 325(1-2):511–519, 2002.

[45] F Diologent and P Caron. On the creep behavior at 1033 K of new generation single-crystal superalloys. *Materials Science and Engineering: A*, 385(1-2):245–257, 2004.

[46] S Ma, L Carroll, and TM Pollock. Development of γ phase stacking faults during high temperature creep of Ru-containing single crystal superalloys. *Acta materialia*, 55(17):5802–5812, 2007.

[47] Alan Howard Cottrell. Dislocations and plastic flow in crystals. *American journal of physics*, 22(4):242–243, 1954.

[48] Derek Hull and David J Bacon. *Introduction to dislocations*, volume 37. Elsevier, 2011.

[49] M Kolbe. The high temperature decrease of the critical resolved shear stress in nickel-base superalloys. *Materials Science and Engineering: A*, 319:383–387, 2001.

[50] Y Yuan, YF Gu, CY Cui, T Osada, T Tetsui, T Yokokawa, and H Harada. Creep mechanisms of U720Li disc superalloy at intermediate temperature. *Materials Science and Engineering: A*, 528(15):5106–5111, 2011.

[51] Haibo Long, Yinong Liu, Deli Kong, Hua Wei, Yanhui Chen, and Shengcheng Mao. Shearing mechanisms of stacking fault and anti-phase-boundary forming dislocation pairs in the γ' phase in Ni-based single crystal superalloy. *Journal of Alloys and Compounds*, 724:287–295, 2017.

[52] Y.Q. Sun and P.M. Hazzledine. Chapter 49 Geometry of dislocation glide in $L1_2$ γ'-phase: TEM observations. In F.R.N. Nabarro and M.S. Duesbery, editors, *$L1_2$ Ordered Alloys*, volume 10 of *Dislocations in Solids*, pages 27 – 68. Elsevier, 1996.

[53] J Th M De Hosson. Superlattice dislocations in $L1_2$ ordered alloys and in alloys containing $L1_2$ ordered precipitates. *Materials Science and Engineering*, 81:515–523, 1986.

[54] H.G Wilsdorf B.H Kear. *Trans. Metall. Soc. AIME*, 224:382, 1962.

[55] V Paidar, DP Pope, and V Vitek. A theory of the anomalous yield behavior in $L1_2$ ordered alloys. *Acta Metallurgica*, 32(3):435–448, 1984.

[56] YM Wang-Koh. Understanding the yield behaviour of $L1_2$-ordered alloys. *Materials Science and Technology*, 33(8):934–943, 2017.

[57] K Yoshimi, S Hanada, and MH Yoo. Yield stress anomaly in B2 FeAl. *MRS Online Proceedings Library (OPL)*, 460, 1996.

[58] Y Nishino and Y Makino. Effect of vanadium substitution on strength properties of Fe3Al-based alloys. *Materials Science and Engineering: A*, 319:368–371, 2001.

[59] V. Vitek, D.P. Pope, and J.L. Bassani. Chapter 51 Anomalous yield behaviour of compounds with $L1_2$ structure. In F.R.N. Nabarro and M.S. Duesbery, editors, *$L1_2$ Ordered Alloys*, volume 10 of *Dislocations in Solids*, pages 135 – 185. Elsevier, 1996.

[60] B Huther, W and Reppich. Interaction of dislocations with coherent, stree-free ordered particles. *Zeitschrift Fur Metallkunde*, 69:628–634, 1978.

[61] H. Gleiter and E. Hornbogen. Theorie der Wechselwirkung von Versetzungen mit kohärenten geordneten Zonen (I). *physica status solidi (b)*, 12(1):235–250, jan 1965.

[62] H. Gleiter and E. Hornbogen. Beobachtung der Wechselwirkung von Versetzungen mit kohärenten geordneten Zonen (II). *physica status solidi (b)*, 12(1):251–264, Jan 1965.

[63] D Raynor and J M Silcock. Strengthening Mechanisms in γ' Precipitating Alloys. *Metal Science Journal*, 4(1):121–130, jan 1970.

[64] V Mohles and E Nembach. The peak-and overaged states of particle strengthened materials: computer simulations. *Acta materialia*, 49(13):2405–2417, 2001.

[65] Benedict M.B. Grant, Elisabeth M. Francis, João Quinta da Fonseca, Michael Preuss, and Mark R. Daymond. The effect of γ' size and alloy chemistry on dynamic strain ageing in advanced polycrystalline nickel base superalloys. *Materials Science and Engineering A*, 573:54–61, jun 2013.

[66] Tao Peng, Bin Yang, Gang Yang, Lu Wang, and Zhihua Gong. Microstructural evolution and mechanical properties of Nimonic 105 alloy aged at 750° C. *Journal of Alloys and Compounds*, 798:375–385, 2019.

[67] D. A. Grose and G. S. Ansell. The influence of coherency strain on the elevated temperature tensile behavior of Ni-15Cr-AI-Ti-Mo alloys. *Metallurgical Transactions A*, 12(9):1631–1645, 1981.

[68] GB Viswanathan, PM Sarosi, MF Henry, DD Whitis, WW Milligan, and MJ Mills. Investigation of creep deformation mechanisms at intermediate temperatures in René 88 DT. *Acta Materialia*, 53(10):3041–3057, 2005.

[69] QZ Chen and David M Knowles. Mechanism of$\langle 112 \rangle/3$ slip initiation and anisotropy of γ' phase in CMSX-4 during creep at 750° C and 750 MPa. *Materials Science and Engineering: A*, 356(1-2):352–367, 2003.

[70] Libor Kovarik, Raymond R Unocic, Ju Li, P Sarosi, C Shen, Yunzhi Wang, and Michael J Mills. Microtwinning and other shearing mechanisms at intermediate temperatures in Ni-based superalloys. *Progress in Materials Science*, 54(6):839–873, 2009.

[71] Johan J Moverare, Sten Johansson, and Roger C Reed. Deformation and damage mechanisms during thermal–mechanical fatigue of a single-crystal superalloy. *Acta Materialia*, 57(7):2266–2276, 2009.

[72] Jan Kanesund, Johan J Moverare, and Sten Johansson. Deformation and damage mechanisms in IN792 during thermomechanical fatigue. *Materials Science and Engineering: A*, 528(13-14):4658–4668, 2011.

[73] Fei Sun, Jianxin Zhang, and Hiroshi Harada. Deformation twinning and twinning-related fracture in nickel-base single-crystal superalloys during thermomechanical fatigue cycling. *Acta materialia*, 67:45–57, 2014.

[74] Y Yuan, YF Gu, T Osada, ZH Zhong, T Yokokawa, and H Harada. Deformation mechanisms in a new disc superalloy at low and intermediate temperatures. *Scripta Materialia*, 67(2):137–140, 2012.

[75] Shuyong Jiang, Dong Sun, Yanqiu Zhang, Xiaoming Zhu, Man Wang, and Chengzhi Zhao. Plastic deformation mechanisms of NiCuCrMoTiAlNb Ni-based alloys at cryogenic temperature. *Materials Science and Engineering: A*, 664:135–145, 2016.

[76] Joakim Nordström, Raveendra Siriki, Mattias Calmunger, Johan Moverare, and Guocai Chai. Twip and fracture behavior in the superalloy 625 at room and cryogenic temperatures. *Procedia Structural Integrity*, 23:457–462, 2019.

[77] Q Ding, H Bei, X Wei, YF Gao, and Z Zhang. Nano-twin-induced exceptionally superior cryogenic mechanical properties of a Ni-based GH3536 (Hastelloy X) superalloy. *Materials Today Nano*, 14:100110, 2021.

[78] Neil D'Souza, Joe Kelleher, Chunlei Qiu, Shu-Yan Zhang, Sam Gardner, Robert E Jones, Duncan Putman, and Chinnapat Panwisawas. The role of stress relaxation and creep during high temperature deformation in Ni-base single crystal superalloys–implications to strain build-up during directional solidification. *Acta Materialia*, 106:322–332, 2016.

[79] David M. Collins, Neil D'Souza, and Chinnapat Panwisawas. In-situ neutron diffraction during stress relaxation of a single crystal nickel-base superalloy. *Scripta Materialia*, 131:103–107, apr 2017.

[80] H J Stone, T M Holden, and R C Reed. On the generation of microstrains during the plastic deformation of Waspaloy. *Acta Materialia*, 47:4435–4448, 1999.

[81] S. Ma, P. Rangaswamy, and B. S. Majumdar. Microstress evolution during in situ loading of a superalloy containing high volume fraction of γ' phase. *Scripta Materialia*, 48:525–530, 2003.

[82] S. Ma, D. Brown, M. A.M. Bourke, M. R. Daymond, and B. S. Majumdar. Microstrain evolution during creep of a high volume fraction superalloy. *Materials Science and Engineering A*, 399:141–153, 2005.

[83] James Coakley, Roger C. Reed, Jonnathan L.W. Warwick, Khandaker M. Rahman, and David Dye. Lattice strain evolution during creep in single-crystal superalloys. *Acta Materialia*, 60(6-7):2729–2738, apr 2012.

[84] Benedict M.B. Grant, Elisabeth Knoche, Michael Preuss, Joao Quinta da Fonseca, and Mark R. Daymond. The Effect of Lattice Misfit on Deformation Mechanisms at High Temperature. *Advanced Materials Research*, 278:144–149, 2011.

[85] D Dye, HJ Stone, and RC Reed. A two phase elastic–plastic self-consistent model for the accumulation of microstrains in Waspaloy. *Acta materialia*, 49(7):1271–1283, 2001.

[86] Ceena Joseph. *Microstructural characterization of Haynes 282 after heat treatment and forging*. Chalmers tekniska högskola, 2015.

[87] Ceena Joseph, Christer Persson, and Magnus Hörnqvist Colliander. Influence of heat treatment on the microstructure and tensile properties of Ni-base superalloy Haynes 282. *Materials Science and Engineering A*, 679:520–530, 2017.

[88] Ceena Joseph. *Microstructure Evolution and Mechanical Properties of Department of Industrial and Materials Science*. PhD thesis, 2018.

[89] L. M. Pike. HAYNES 282 Alloy: A New Wrought Superalloy Designed for Improved Creep Strength and Fabricability. In *Volume 4: Cycle Innovations; Electric Power; Industrial and Cogeneration; Manufacturing Materials and Metallurgy*, page 1031. ASME, may 2006.

[90] KL Kruger. Haynes 282 alloy. In *Materials for ultra-supercritical and advanced ultra-supercritical power plants*, pages 511–545. Elsevier, 2017.

[91] RA Buckson and OA Ojo. Cyclic deformation characteristics and fatigue crack growth behaviour of a newly developed aerospace superalloy Haynes 282. *Materials Science and Engineering: A*, 555:63–70, 2012.

[92] Magnus Hörnqvist, Ceena Joseph, Christer Persson, Jonathan Weidow, and Haiping Lai. Dynamic strain aging in Haynes 282 superalloy. *MATEC Web of Conferences*, 14:16002, aug 2014.

[93] Junjing He, Rolf Sandström, and Sandro Notargiacomo. Low-cycle fatigue properties of a nickel-based superalloy Haynes 282 for heavy components. *Journal of Materials Engineering and Performance*, 26(5):2257–2263, 2017.

[94] R Brommesson, M Ekh, and C Persson. Experimental observations and modelling of cyclic and relaxation behaviour of the Ni-based superalloy Haynes 282. *International Journal of Fatigue*, 87:180–191, 2016.

[95] Kyeong-Yong Shin, Jin-Hyeok Kim, Mathieu Terner, Byeong-Ook Kong, and Hyun-Uk Hong. Effects of heat treatment on the microstructure evolution and the high-temperature tensile properties of Haynes 282 superalloy. *Materials Science and Engineering: A*, 751:311–322, 2019.

[96] Anne Elizabeth Staton-Bevan and RD Rawlings. The deformation behaviour of single crystal Ni_3(Al, Ti). *Physica status solidi (a)*, 29(2):613–622, 1975.

[97] Y Umakoshi, DP Pope, and V Vitek. The asymmetry of the flow stress in Ni_3(Al,Ta) single crystals. *Acta Metallurgica*, 32(3):449–456, 1984.

[98] Toshio Saburi, Takatoshi Hamana, Soji Nenno, and Han-ryong Pak. Temperature and orientation dependence of the yield strength of Ni_3(Al,W). *Japanese Journal of Applied Physics*, 16(2):267, 1977.

[99] C Lall, S Chin, and DP Pope. The orientation and temperature dependence of the yield stress of Ni_3(Al,Nb) single crystals.

[100] DB Miracle. Deformation in NiAl bicrystals. *Acta metallurgica et materialia*, 39(7):1457–1468, 1991.

[101] RR Bowman, RD Noebe, SV Raj, and IE Locci. Correlation of deformation mechanisms with the tensile and compressive behavior of NiAl and NiAl (Zr) intermetallic alloys. *Metallurgical Transactions A*, 23(5):1493–1508, 1992.

[102] J.A. Wollmershauser, S. Kabra, and S.R. Agnew. In situ neutron diffraction study of the plastic deformation mechanisms of B2 ordered intermetallic alloys: NiAl, CuZn, and CeAg. *Acta Materialia*, 57(1):213–223, jan 2009.

[103] A Lasalmonie. Deformation of Ni-Al at high temperature. *Journal of Materials Science*, 17(8):2419–2423, 1982.

[104] M Dollar, S Dymek, SJ Hwang, and P Nash. The occurrence of $\langle 110 \rangle$ slip in NiAl. *Scripta metallurgica et materialia*, 26(1):29–34, 1992.

[105] S Dymek, M Dollar, SJ Hwang, and P Nash. Influence of texture and hydrostatic pressure on the room temperature compression of NiAl polycrystals. *Mater Sci Eng A*, 152:160–165, 1992.

[106] T Yamagata and H Yoshida. Deformation behavior of FeAl single crystals. *Materials Science and Engineering*, 12(2):95–100, 1973.

[107] T Takasugi, S Hanada, and O Izumi. Slip modes in B2-type intermetallic alloys. *Materials Transactions, JIM*, 31(6):435–442, 1990.

[108] K-M Chang, R Darolia, and HA Lipsitt. Cleavage fracture in B2 aluminides. *Acta metallurgica et materialia*, 40(10):2727–2737, 1992.

[109] DL Yaney, AR Pelton, and WD Nix. Dislocations in extruded Co-49.3 at% Al. *Journal of materials science*, 21(6):2083–2087, 1986.

[110] C Vailhé and D Farkas. Shear faults and dislocation core structures in B2 CoAl. *Journal of materials research*, 12(10):2559–2570, 1997.

[111] Michael Feuerbacher. Dislocations and deformation microstructure in a B2-ordered $Al_{28}Co_{20}Cr_{11}Fe_{15}Ni_{26}$ high-entropy alloy. *Scientific reports*, 6(1):1–9, 2016.

[112] Yiping Lu, Xuzhou Gao, Li Jiang, Zongning Chen, Tongmin Wang, Jinchuan Jie, Huijun Kang, Yubo Zhang, Sheng Guo, Haihui Ruan, Yonghao Zhao, Zhiqiang Cao, and Tingju Li. Directly cast bulk eutectic and near-eutectic high entropy alloys with balanced strength and ductility in a wide temperature range. *Acta Materialia*, 124:143–150, feb 2017.

[113] J. Chadwick. The Neutron and its Properties. *The British Journal of Radiology*, 6(61):24–32, 1933.

[114] J Chadwick. Possible Existence of a Neutron. *Nature*, 129(3252):312–312, feb 1932.

[115] Castro GL G Garcıa A, Garcıa-Luna JL. Neutron beta decay and the current determination of Vud. *Physics Letters B*, 500(1-2):66–74, feb 2001.

[116] Juan Rodríguez-Carvajal. Recent advances in magnetic structure determination by neutron powder diffraction. *Physica B: Condensed Matter*, 192(1-2):55–69, oct 1993.

[117] RP Feynman. Quantum mechanics, col. 3, Lectures on Physics, 1970.

[118] Louis De Broglie. *Recherches sur la théorie des quanta*. PhD thesis, Migration-université en cours d'affectation, 1924.

[119] Andrew T Boothroyd. *Principles of Neutron Scattering from Condensed Matter*. Oxford University Press, Jul 2020.

[120] Ao Allen, C Andreani, MT Hutchings, and CG Windsor. Measurement of internal stress within bulk materials using neutron diffraction. *NDT international*, 14(5):249–254, 1981.

[121] PJ Withers and PJ Webster. Neutron and synchrotron X-ray strain scanning. *Strain*, 37(1):19–33, 2001.

[122] Philip J Withers and HKDH Bhadeshia. Residual stress. part 1–measurement techniques. *Materials science and Technology*, 17(4):355–365, 2001.

[123] Stefanos Athanasopoulos. *Multiscale granular mechanics: A neutron diffraction based experimental approach*. PhD thesis, 2019.

[124] J. R. Santisteban, M. R. Daymond, J. A. James, and L. Edwards. ENGIN-X: A third-generation neutron strain scanner. *Journal of Applied Crystallography*, 39:812–825, 2006.

[125] Edward Oliver, Beth Evans, Mohammad Chowdhury, Robert Major, Oleg Kirichek, and Zoe Bowden. Novel testing chamber for neutron scattering measurements of internal stresses in engineering materials at cryogenic temperatures. *Measurement Science and Technology*, 19(3):034019, jan 2008.

[126] O Kirichek, JD Timms, JF Kelleher, RBE Down, CD Offer, S Kabra, and SY Zhang. Sample environment for neutron scattering measurements of internal stresses in engineering materials in the temperature range of 6 K to 300 K. *Review of Scientific Instruments*, 88(2):025103, 2017.

[127] Yiqiang Wang, Bin Liu, Kun Yan, Minshi Wang, Saurabh Kabra, Yu-Lung Chiu, David Dye, Peter D Lee, Yong Liu, and Biao Cai. Probing deformation mechanisms of a FeCoCrNi high-entropy alloy at 293 and 77 K using in situ neutron diffraction. *Acta Materialia*, 154:79–89, 2018.

[128] Lei Tang, Kun Yan, Biao Cai, Yiqiang Wang, Bin Liu, Saurabh Kabra, Moataz M Attallah, and Yong Liu. Deformation mechanisms of $FeCoCrNiMo_{0.2}$ high entropy alloy at 77 and 15 K. *Scripta Materialia*, 178:166–170, 2020.

[129] Lei Tang, Li Wang, Minshi Wang, Huibin Liu, Saurabh Kabra, Yulung Chiu, and Biao Cai. Synergistic deformation pathways in a twip steel at cryogenic temperatures: In situ neutron diffraction. *Acta Materialia*, 200:943–958, 2020.

[130] Yajuan Shi, Shilei Li, Tung Lik Lee, Xidong Hui, Zhewei Zhang, Runguang Li, Minghe Zhang, Saurabh Kabra, and Yan-Dong Wang. In situ neutron diffraction study of a new type of stress-induced confined martensitic transformation in $Fe_{22}Co_{20}Ni_{19}Cr_{20}Mn_{12}Al_7$ high-entropy alloy. *Materials Science and Engineering: A*, 771:138555, 2020.

[131] R Haynes, AM Paradowska, MAH Chowdhury, CM Goodway, R Done, O Kirichek, and EC Oliver. An inert-gas furnace for neutron scattering measurements of internal stresses in engineering materials. *Measurement Science and Technology*, 23(4):047002, 2012.

[132] Stefanus Harjo, Kazuya Aizawa, Takayoshi Ito, Hiroshi Arima, Jun Abe, Atsushi Moriai, Kaoru Sakasai, Tatsuya Nakamura, Takeshi Nakatani, Takaaki Iwahashi, et al. Aspire To Become TAKUMI-TAKUMI present status and research topics. In *Materials Science Forum*, volume 652, pages 99–104. Trans Tech Publ, 2010.

[133] Stefanus Harjo, Takayoshi Ito, Kazuya Aizawa, Hiroshi Arima, Jun Abe, Atsushi Moriai, Takaaki Iwahashi, and Takashi Kamiyama. Current Status of Engineering Materials Diffractometer at J-PARC. *Materials Science Forum*, 681(September 2008):443–448, 2011.

[134] Takayoshi Ito, Takeshi Nakatani, Stefanus Harjo, Hiroshi Arima, Jun Abe, Kazuya Aizawa, and Atsushi Moriai. Application software development for the engineering materials diffractometer, TAKUMI. In *Materials Science Forum*, volume 652, pages 238–242. Trans Tech Publ, 2010.

[135] Takayoshi Ito, Stefanus Harjo, Yasuhiro Inamura, Takeshi Nakatani, Takuro Kawasaki, Jun Abe, and Kazuya Aizawa. Utilization of an Event-Recording System for Neutron Diffraction Experiments. *Materials Science Forum*, 783-786:2071–2074, may 2014.

[136] Seiko Ohira-Kawamura, Takanori Hattori, Stefanus Harjo, Kazutaka Ikeda, Noboru Miyata, Tsukasa Miyazaki, Hiroyuki Aoki, Masao Watanabe, Yoshifumi Sakaguchi, and Takayuki Oku. Highlight of recent sample environment at J-PARC MLF. *Neutron News*, 30(1):11–13, 2019.

[137] S. I. Campbell, F. A. Akeroyd, and C M Moreton. Open GENIE – Analysis and Control. In *NOBUGS*, oct 2002.

[138] Owen Arnold, Jean-Christophe Bilheux, JM Borreguero, Alex Buts, Stuart I Campbell, L Chapon, Mathieu Doucet, N Draper, R Ferraz Leal, MA Gigg, et al. Mantid—Data analysis and visualization package for neutron scattering and μ SR experiments. *Nuclear Instruments and Methods in Physics Research Section A: Accelerators, Spectrometers, Detectors and Associated Equipment*, 764:156–166, 2014.

[139] Brian H. Toby, Robert B. Von Dreele, and IUCr. GSAS-II : the genesis of a modern open-source all purpose crystallography software package. *Journal of Applied Crystallography*, 46(2):544–549, apr 2013.

[140] M. R. Daymond, M. A.M. Bourke, R. B. Von Dreele, B. Clausen, and T. Lorentzen. Use of Rietveld refinement for elastic macrostrain determination and for evaluation of plastic strain history from diffraction spectra. *Journal of Applied Physics*, 82(4):1554–1562, 1997.

[141] Mark R Daymond. The determination of a continuum mechanics equivalent elastic strain from the analysis of multiple diffraction peaks. *Journal of applied physics*, 96(8):4263–4272, 2004.

[142] David L Joy, David C and Newbury, Dale E and Davidson. Electron channeling patterns in the scanning electron microscope. *Journal of Applied Physics1*, 53:R81—-R122, 1982.

[143] Olaf Engler and Gunter Gottstein. New approach in texture research: local orientation determination with EBSP. *Steel Research*, 63(9):413–418, sep 1992.

[144] Stuart I. Wright, Matthew M. Nowell, and David P. Field. A review of strain analysis using electron backscatter diffraction, may 2011.

[145] David B Williams and C Barry Carter. Strain fields. In *Transmission Electron Microscopy*, pages 401–420. Springer, 1996.

[146] A Baczmanski, L Le Joncour, B Panicaud, M Francois, C Braham, A M Paradowska, S Wronski, S Amara, and R Chiron. Neutron time-of-flight diffraction used to study aged duplex stainless steel at small and large deformation until sample fracture. *Journal of Applied Crystallography*, 44(5):966–982, 2011.

[147] Y. Zhao, L. Le Joncour, A. Baczmański, E. Gadalińska, S. Wroński, B. Panicaud, M. François, C. Braham, and T. Buslaps. Stress distribution correlated with damage in duplex stainless steel studied by synchrotron diffraction during plastic necking. *Materials and Design*, 113:157–168, 2017.

[148] A. Baczmański, Y. Zhao, E. Gadalińska, L. Le Joncour, S. Wroński, C. Braham, B. Panicaud, M. François, T. Buslaps, and K. Soloducha. Elastoplastic deformation and damage process in duplex stainless steels studied using synchrotron and neutron diffractions in comparison with a self-consistent model. *International Journal of Plasticity*, 81:102–122, 2016.

[149] Saideep Muskeri, Vahid Hasannaeimi, Riyadh Salloom, Maryam Sadeghilaridjani, and Sundeep Mukherjee. Small-scale mechanical behavior of a eutectic high entropy alloy. *Scientific Reports*, 10(1):2669, dec 2020.

[150] N. Clément, G. Molénat, and D. Caillard. An in situ study of cube glide in the γ'-phase of a superalloy. *Philosophical Magazine A: Physics of Condensed Matter, Structure, Defects and Mechanical Properties*, 64(3):669–695, 1991.

[151] Bertram Eugene Warren. *X-ray Diffraction*. Courier Corporation, 1990.